UNIVERSITY OF PISA

Engineering PhD School "Leonardo da Vinci"

PhD Course in
"Applied Electromagnetism in Electrical and Biomedical Engineering, Electronics, Smart Sensors, Nano-Technologies"

PhD Thesis

Design and characterization of antennas for wireless communications systems

ING/INF-02

Tutors:

Prof. Ing. Paolo NEPA _____

Prof. Ing. Giuliano MANARA _____

Author

Ing. Roberto CASO

_____

2012

CONTEST

JOURNAL PUBLICATIONS

1. R. Caso, A. D'Alessandro, A. Michel, P. Nepa, and G. Manara, "Integration of Slot Antennas in Commercial Photovoltaic Panels for Stand-Alone Communication Systems," submitted to *IEEE Transactions on Antennas and Propagation, 2012.*
2. R. Caso. A. D'Alessandro, A.A. Serra, and P. Nepa, "Dual-Band L-Shape PIFA for Display-Equipped Devices," submitted to *Electronic Letters*, 2012.
3. A. Guraliuc, R. Caso, P. Nepa, and J. L. Volakis, "Numerical Analysis of a Wideband Thick Archimedian Spiral Antenna," to appear on *IEEE Antenna and Wireless Propagation Letters*, 2012
4. R. Caso, A. D'Alessandro, A.A Serra, P. Nepa, and G. Manara, "Compact integrated dual-band G-PIFAs for DVB-T and WLAN applications," to appear on *IEEE Transactions on Antennas and Propagation*, 2012
5. R. Caso, A. D'Alessandro, A.A Serra, P. Nepa, and G. Manara, "An Integrated Dual-Band PIFA for DVB-T and WIMAX Applications," *IEEE Antenna and Wireless Propagation Letters*, vol. 10, pp. 1027-1030, 2011.
6. R. Caso, A.A. Serra, A. Buffi, M.R. Pino, P. Nepa, and G. Manara, "Dual-Polarized Slot-Coupled Patch Antenna Excited by a Square Ring Slot," *IET Microwaves, Antennas & Propagation,* vol. 5, pp. 605-610, 2011.
7. R. Caso, A.A. Serra, M.R. Pino, P. Nepa, and G. Manara, "A Wideband Slot-Coupled Stacked-Patch Array for Wireless Communications*," IEEE Antenna and Wireless Propagation Letters*, vol.9, pp. 986-989186, 2010.
8. A. Buffi, R. Caso, M.R. Pino, P. Nepa, and G. Manara, "Single-feed circularly polarised aperture-coupled square ring slot microstrip antenna," *Electronics Letters*, vol. 46, pp.268-269, 2010.
9. A. Buffi, R. Caso, G. Manara, P. Nepa, and A.A. Serra, "Ring-slot coupled microstrip patch antennas," *Atti della fondazione Giorgio Ronchi,* 2010.
10. R. Caso, A. Buffi, M.R. Pino, P. Nepa, and G. Manara, "A novel dual-feed slot-coupling feeding technique for circularly polarized patch arrays," *IEEE Antenna and Wireless Propagation Letters*, vol.9, pp. 183-186, 2010.

CONFERENCE PUBLICATIONS

11. R. Caso, A. Michel, P. Nepa, G. Manara, and R. Massini, *"Design and Performance of an Integrated Antenna for a 433MHz Car Park Monitoring System*," *IEEE AP-S International Symposium*, Chicago, Illinois, USA, 2012.
12. A. Michel, R. Caso, P. Nepa, L. Tavanti, L. Gazzarrini, and R. Garroppo, "Design and Performance Analysis of a Slot Antenna Integrated in a Photovoltaic Panel," *IEEE AP-S International Symposium*, Chicago, Illinois, USA, 2012.
13. A.A. Serra, R. Caso, A. Buffi, A. Guraliuc, A. Michel, A. D'Alessandro, and P. Nepa "Research Activity on Antenna Design for Wireless Communication Networks at the University of Pisa," *IEEE AP-S International Symposium*, Chicago, Illinois, USA, 2012.
14. R. Caso, A. D'Alessandro, A.A Serra, P. Nepa, and G. Manara, "Dual-band integrated G-PIFA antenna for DVB-T and WLAN applications," *IEEE AP-S International Symposium*, Spokane, Washington, USA, 2011.
15. R. Caso, A. D'Alessandro, A.A Serra, P. Nepa, and G. Manara, "Wideband integrated H-PIFA antenna for DVB-T and WIMAX applications," *IEEE AP-S International Symposium*, Spokane, Washington, USA, 2011.
16. R. Caso, A. Buffi, and A.A. Serra, "Ring slot coupled microstrip patch antennas," *RiNEm Riunione Nazionale di Elettromagnetismo*, Benevento, Italy, 2010.
17. A. Buffi, R. Caso, M.R. Pino, and P. Nepa, "AR Bandwidth Enhancement for Single-Feed Circularly Polarized Square Ring Slot Patch Antenna," *EMTS International Symposium on Electromagnetic Theory,* Berlin, Germany, 2010.
18. A. Buffi, R. Caso, M.R. Pino, P. Nepa, and G. Manara, "Circularly Polarized Square Ring Slot Patch Antennas," *IEEE AP-S International Symposium*, Toronto, Ontario, 2010.
19. R. Caso, A.A. Serra, M.R. Pino, P. Nepa, and G. Manara, "A wideband linear array of slot coupled stacked-patches," *IEEE AP-S International Symposium*, Toronto, Ontario, 2010.
20. R. Caso, A. Buffi, M.R. Pino, P. Nepa, and G. Manara, "An annular-slot coupling feeding technique for dual-feed circularly polarized patch arrays," *IEEE AP-S International Symposium,* Toronto, Ontario, 2010.
21. A. Buffi, R. Caso, M.R. Pino, P. Nepa, and G. Manara, "A novel slot-coupling feeding technique for circularly polarized patch antennas," *IWAT International Workshop on Antenna Technology,* Lisbon, Portugal, p. 1-4, 2010.

22. A. Buffi, R. Caso, G. Manara, P. Nepa, and A.A. Serra, "Dual-polarization slot-coupled patch antennas: state-of-art and a novel configuration," *Giornata di studio sulla caratterizzazione di antenne*, Salerno, Italy, 2009.
23. R. Caso, A.A. Serra, P. Nepa, G. Manara, and M.R. Pino, "A square ring slot feeding technique for dual-polarized patch antennas," *IEEE AP-S International Symposium*, Charleston, SC USA, 2009.
24. R. Caso, G. Manara, P. Nepa, and A.A. Serra, "Progettazione di antenne per apparati WIMAX," *RiNEm Riunione Nazionale di Elettromagnetismo*, Lecce, Italy, 2009.
25. A.A. Serra, R. Caso , P. Nepa, and G. Manara, "A wideband dual-polarized stacked patch antenna array for base stations," *ISAP - International Symposium on Antennas and Propagation*, Taipei, Taiwan, 2008.
26. R. Caso, G. Manara, P. Nepa, and A.A. Serra, "Antenne a microstriscia a larga banda e multi-banda per le stazioni radio base dei sistemi UMTS, WLAN e WIMAX," *Giornata di Studio: Coesistenza e compatibilità elettromagnetica delle tecnologie wireless emergenti*, L'Aquila, Italy, 2008.

INTRODUCTION

The pervasive development of wireless communication networks has determined a greater than ever need for high-performance antennas for large-scale production. Mass-production antennas must be simple, low-cost, easy-to-assembly, compact and low-weight. Nevertheless, they are also required to meet demanding electrical specifications: high-efficiency in compact antennas, shaped radiation patterns for base-station antennas, reconfigurability features for opportunistic communication antennas, easy integration for mobile terminal antennas, electrical robustness in wearable textile antennas for body-centric communications, as well as high isolation in dual-polarization antennas, antennas for MIMO applications and diversity reception. During his PhD studies at the Microwave and Radiation Laboratory of the Department of Information Engineering, University of Pisa, the author gained a valuable experience in designing, prototyping and characterizing planar antennas in the frequency range from a few hundred MHz up to 10 GHz.

Advantages of microstrip technology in terms of easy-fabrication, low-weight and reliability in mass production, determined an extended utilization of printed antennas for the realization of planar antennas for base stations (or access points) and subscriber units (CPE, customer premises equipment) of wireless communication networks, as for example wireless local networks (WLANs) at the 2.4 GHz ISM band (IEEE 802.11b/g), WIMAX™ systems in the 3.3-3.8GHz frequency range, and high-data rate communications at 5-6GHz (Hiperlan, IEEE 802.11a).

In this context, in Chapter I the author presents a novel feeding technique for dual-polarized patch antennas, where the patch and the feeding line are coupled through a resonant square ring slot [1]-[4]. In [5]-[10], it has been shown that the above technique is effective in realizing single-feed and double-feed circularly polarized antennas.

Prototypes operating at the WIMAX frequency band have been realized and prototyped [1]-[10]. Moreover a stacked-version [11]-[12] of the dual linearly polarized patch has been used to get up to 45% percentage impedance bandwidth, with a 2x1 array working in the GSM 1800-1900 band (1710-1910 MHz), UMTS band (1920-2170 MHz), ISM band (2400-2484 MHz), and UMTS 3G expansion band (2500-2690 MHz). Most of the work on ring slot coupled patch antennas has been carried out in collaboration with the University of Oviedo, Spain, where the author spent a period to gain experience in antenna prototyping and radiation pattern measurements in a fully anechoic chamber.

Several antenna prototypes that exploit different feeding techniques for microstrip antennas have been realized [13]-[16] in collaboration with the Yuan Ze University of Taipei and the company Telsa s.r.l. [17], Bergamo, Italy.

DVB-T (Digital Video Broadcasting-Terrestrial) standards are rapidly becoming very popular and they are nowadays the only terrestrial television service available in many regions. Next generation terminals will be required to have an integrated antenna in order to avoid cabled connections and to make them relatively portable (at least within an indoor scenario). In addition to this, a web access could be provided to guarantee access to on-demand services.

In Chapter II, a couple of dual-band antenna that can guarantee access to both TV and internet services are presented [18]-[22]. They are dual-band PIFA (Planar Inverted-F Antenna) antennas properly designed to fit in monitor-equipped devices with relatively stringent mechanical and aesthetic constraints; they exhibit the second resonance at WIMAX™ [18]-[19] or the 2.4 GHz [20]-[22] frequency band. All the above cited PIFAs are low-cost solutions as they can be made out of a cut and bent single metallic sheet. The antenna prototyping and characterization have been carried out in collaboration with the company SECO s.r.l., Arezzo, Italy [23].

There is a need for wide bandwidth antennas to serve several functions including navigation, broadcasting and personal communication, to mention a few. Using different antennas to cover all communication bands is a simple approach, but leads to increased costs, weight, more surface area for installation and electromagnetic

compatibility issues. The adoption of a single, small size wideband antenna is certainly more attractive. Spirals are widely used circularly-polarized wideband antennas.

In Chapter III, a numerical analysis is performed for a wideband two-arm Archimedean spiral. In contrast to conventional spirals, each metallic strip is vertically oriented [24] with respect to the antenna's aperture. Indeed, using vertical strips to form the spiral arms leads to a larger number-of-turns within the same aperture size. Concurrently, this approach allows for a more effective and easier control of the spiral's input resistance as compared to conventional spirals (that use planar strips to form the arms), by varying the strip width and turn thickness. Also, when the antenna is embedded in a dielectric block, miniaturization is more effective than in conventional planar Archimedean spirals. Above activity has been developed in collaboration with the Electro-Science Laboratory, Ohio State University, US.

Autonomous communication systems often use photovoltaic (PV) panels that are physically separated from the antenna, and this demands for a compromise in the utilization of the available space. Moreover, in several applications, as for example monitoring, vehicular communication and satellite systems, distinct PV panel and antenna may be anti-aesthetic, expensive and causes engineering issues. For above reasons, antenna integration in large PV panels is desirable and it has become a research topic.

In Chapter IV, two configurations of slot antennas suitable for integration into a class of commercial large photovoltaic (PV) panels are presented [25]-[26]. The basic idea is to exploit the room available between adjacent PV cells, also taking advantage of the presence of the cover glass layer that gives a valuable miniaturization effect. As test cases, two antenna designs are presented for stand-alone communication systems operating in the GSM/UMTS (1710-2170 MHz) and WIMAX (3300-3800 MHz) frequency bands. The numerical design has been performed by resorting to quite simple numerical models; after that, the effects on the antenna performance of the presence of nearby photovoltaic cells, DC bus wires and panel frame have been verified through a measurement campaign with slot antenna prototypes attached to real PV panels. Then, a

straightforward fine tuning has been adopted to match the antennas when installed on the panel.

The demand for intelligent parking systems is expected to grow in the near future, to provide automatic management and monitoring, as well as convenience to the customers. Such a system can be made of an RF reader, and a set of wireless sensors (or autonomous transmitters) each one placed on the ground of a parking space. The 433MHz ISM band is prefereed to the 2.4GHz one as lower frequency is more robust to car shadowing and interference level is lower too.

In Chapter V, a top-loaded vertical monopole antenna to be integrated in a wireless sensor of a car park monitoring system operating at 433MHz is designed [28]. The final design came out from a careful analysis of the effects on the antenna input impedance of nearby elements (photovoltaic cells, battery, sensor cover, ultrasonic transducer). A performance comparison between the proposed vertically polarized antenna and a commercial ceramic antenna is presented, showing an average increase of the received power level at the reader of about 2.2dB, when measurements are performed on a distance range of 10-60m between the sensor and the reader antenna of the car park monitoring system.

Research activities described in Chapter IV and Chapter V have been carried out in collaboration with the consortium CUBIT [27], Polo Tecnologico di Navacchio, Cascina, Pisa.

Chapter I

1 DUAL-POLARIZED SLOT-COUPLED PATCH ANTENNA EXCITED BY A SQUARE RING SLOT

1.1 Introduction

Recent years have seen a significant exploitation of printed antenna technology in mass production of planar arrays for base stations and subscriber units of cellular communication systems. Indeed, microstrip antennas are characterized by their low profile, light weight, ease of construction, and high flexibility in designing shaped-beam and multiband antennas. A common feeding technique for wideband antennas is that based on slot-coupling, where a microstrip line is coupled to the radiating patch through a slot in a metallic ground plane, as first proposed by Pozar [29]. Slot-coupled patches can exhibit a quite large impedance bandwidth at the cost of an affordable construction complexity, and allow for more space for the feed network with respect to microstrip fed arrays (the latter being an important need especially for dual-polarized dense phased arrays [30]). Moreover, the metallic ground plane where slots are realized prevents the spurious radiation from the feed network and then reduces the amplitude of the cross-polar components.

1.2 A Square Ring Slot Feeding Technique

1.2.1 Introduction

To extend the single-feed single-polarization design to the dual-polarization antenna design, a large number of aperture-coupled patch antennas have been presented in the open literature [31]-[46] (most of them are shown in Figure 1.1). In a dual-polarized slot-coupled patch, the two orthogonal fundamental modes can be excited through either a centered cross-shaped slot (namely two crossed slots) [31]-[38] (configurations denoted as "X_1"-"X_5" in Figure 1.1) or two separated orthogonal slots [39]-[46].

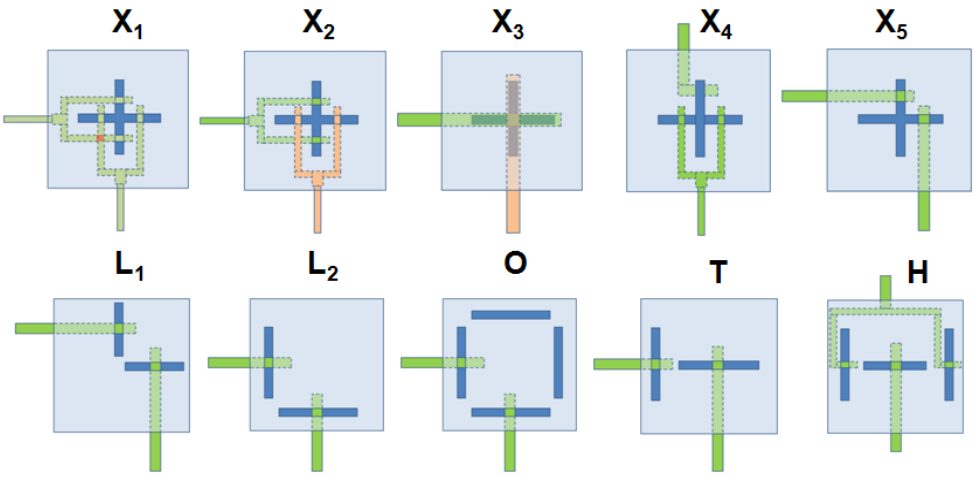

Figure 1.1 - Some configurations of dual-polarized slot-coupled patch antennas, with different positions of the two coupling slots with respect to the patch center. Feed lines with the same color are printed on the same side of a dielectric slab; in X1 an air bridge (denoted by a red square) is needed to avoid line overlapping.

Dual-polarized slot-coupled patches with a cross-shaped slot fed by two orthogonal balanced feed lines [31]-[36] result in good performance in terms of isolation and cross-

polarization level. On the other hand, to avoid overlapping between the two feed lines, either an air bridge [31], [32], or a double-layer substrate [33]-[36] is needed, both of which increase the realization cost of large arrays. In search of less expensive single-layer feed networks, antenna designers have developed dual-polarized slot-coupled patch configurations using a cross-shaped slot centered beneath the patch and two non-overlapping feed lines etched on the same side of a single layer laminate [37]-[38].

Dual-polarized slot-coupled patch configurations with non-overlapping feed lines printed on the same side of a single layer substrate can also be realized by resorting to two separate perpendicular slots (it allows the feed line to remain at the center of the corresponding slot, for both polarization ports). A number of patches characterized by either one ("T" and "H" layouts in Figure 1.1) or all slots ("L_1", "L_2" and "O" layouts in Figure 1.1) shifted with respect to the patch center have been proposed [39]-[46].

In this chapter, a novel dual-polarized slot-coupled patch antenna exhibiting a symmetry property with respect to the two microstrip feed lines is presented. A square patch is coupled to a pair of microstrip feed lines by a square ring slot realized in a metallic ground plane, and both feed lines are on the same side of a single-layer substrate. To show the working principle and the radiation properties of the proposed slot-coupled patch, a sample antenna operating in the 3.3-3.8 GHz WIMAX™ frequency band has been designed. Simulated data agrees well with measurements on an antenna prototype. In the paragraph 1.2.2, the novel slot-coupling feeding technique and its working principle are illustrated. Simulation results obtained with a full-wave commercial tool (Ansoft HFSS™) and a comparison with measurements on an antenna prototype are presented and discussed in the paragraph 1.2.3. Finally, concluding remarks and work in progress are both given in the paragraph 1.2.4.

1.2.2 Antenna Design

The novel dual-polarized slot-coupled patch antenna fed through a square ring slot is shown in Figure 1.2. It is apparent that the layout is symmetric with respect to the two input ports. The latter represents a useful feature when designing a wideband dual-circular polarized patch (requiring an additional feeding circuit to generate two signals with the same amplitude and a 90° phase shift), or when designing the feeding network of a dual-polarized array.

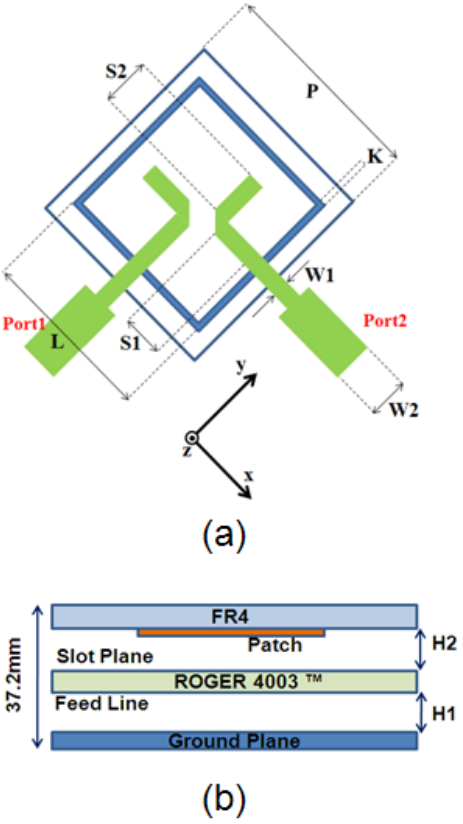

Figure 1.2 - (a) Top view and (b) stackup of the square patch fed through a square ring slot. Dimension of the geometrical parameters for a WIMAX™ antenna: P=20.5mm, L=16.3mm, K=0.5mm, W1=2.5mm, W2=3.7mm, S1=2mm, S2=7.5mm. H1=22mm, H2=11mm.

It is worth noting that, in dual-polarized patch antennas, geometrical and electrical symmetry are advantageous in improving port isolation and cross-polarization performance.

To show the working principle and the radiation properties of the proposed slot-coupled patch, a sample antenna operating at the 3.3-3.8 GHz WIMAX™ frequency band has been designed, fabricated and characterized. Nevertheless, it is apparent that the proposed geometry can be used for any application where a planar dual-polarized antenna with a port isolation greater than 20dB and a fractional bandwidth greater than 10-15% is required (larger impedance bandwidths can be obtained by adding a square stacked patch).

In the sample antenna, both microstrip lines are printed on the same 1.524mm thick Rogers RO4003 substrate (εr=3.55, tgδ=0.0027), which is 70x70 mm^2 square. The square ring slot has a perimeter of 65.2mm and is etched on the other side of the above substrate, namely on the metallic ground plane separating the feed lines from the square patch. As in other slot-coupled patch configurations, the length of the open-circuited stub behind the slot is optimized for input impedance tuning. A 100x100 mm^2 square aluminum reflector is placed at a distance of 22mm from the feed lines, to reduce back radiation and increase the antenna gain. The 20.5x20.5 mm^2 copper patch is printed on the bottom layer of an FR4 laminate, which is 1.6mm thick and 60x60 mm^2 wide (it also acts as a cover for the antenna). The air gap between the patch and the slot plane is 11mm thick. Figure 1.3 illustrates the electric field distribution inside the square ring slot when port 1 of the patch in Figure 1.2 is fed. It is apparent that the field distribution resembles that of the fundamental resonating mode of a ring slot. This is in agreement with the fact that the slot perimeter is close to the guided wavelength λg of a slotted line with the same geometrical and electrical parameters as those of the slot: λg=66mm, at 3.5GHz.

The electric field distribution shown in Figure 1.3 reveals a number of interesting features.

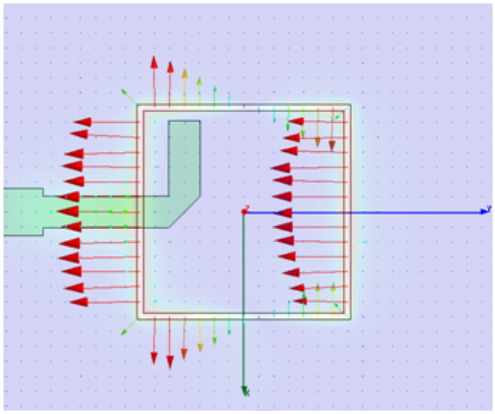

(a)

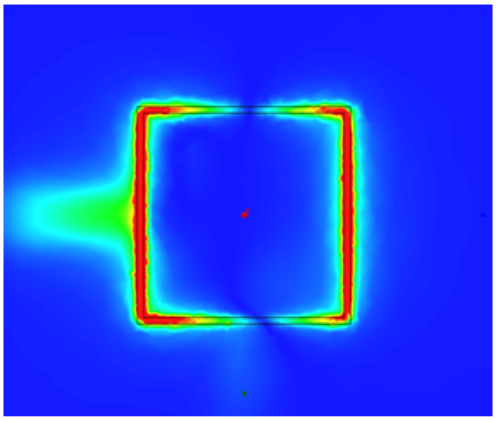

(b)

Figure 1.3 - (a) Direction and (b) amplitude of the electric field inside the square ring slot, when port 1 of the antenna in Figure 1.2 is fed (HFSS data).

The side of the ring slot that is directly fed and the one parallel to it are both excited, and the electric fields induced into the two slot-sides are in phase and with a similar amplitude; as a consequence, due to above phase relationship and the symmetric position of the above the sides with respect to the patch centre, the resonant mode of the patch (that one associated with port 1) is properly excited and low cross-polarization is expected.

Moreover, the electric field distribution induced into the two sides of the slot orthogonal to the previous ones are out of phase and do not excite the orthogonal resonant mode of the patch (that one associated to port 2). Finally, the induced electric field does vanish close to the centre of the above sides of the slots; it means that relatively high port isolation is expected when that point is used to couple the slot ring to the feed line of port 2.

It is worth noting that since the slot perimeter is less than the free-space wavelength (actually it is around a slot-line guided wavelength) and the patch perimeter is almost double the free-space wavelength, the whole square ring slot always remains under the patch, for any design frequency. Moreover, due to the symmetry between the two ports, the two corporate feed networks of a dual-polarized array can be identical, and the same radiation patterns and gain for the two ports are expected in the whole antenna frequency bandwidth.

The novel layout presented here can be seen as an advancement of the modified "L" configuration presented by Shafai et al. in [42] (the configuration named as "O" in Figure 1.1). Indeed, it is apparent that the 4-slot arrangement in the "O" configuration, which is symmetric with respect to the patch centre, resembles the ring slot geometry. The significant difference is that in the novel configuration all four sides of the ring slot contribute effectively and correctly to the excitation of the two orthogonal fundament patch resonant modes, while in the "O" configuration two slots are just parasitic slots used to minimize the cross-polarization level (also, amplitude and phase of the parasitic slot contribution cannot be easily controlled in the design phase).

1.2.3 Numerical and Experimental Results

In this paragraph, HFSS simulation results will be compared with measurements carried out on a prototype of the WIMAX™ patch antenna. The antenna prototype is shown in Figure 1.4, and it has been measured in the anechoic chamber at the Department of Electrical Engineering of the University of Oviedo.

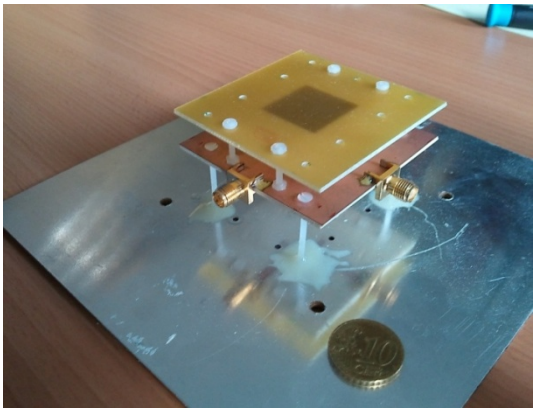

Figure 1.4 - Photo of an antenna prototype.

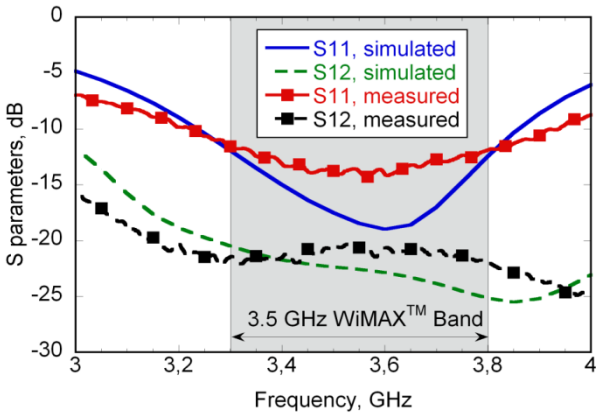

Figure 1.5 - Measured and simulated S-parameters of the square ring slot fed patch

Both measurement and simulation results for the reflection coefficient and port isolation are shown in Figure 1.5, and they exhibit a reasonable agreement.

For both polarizations, the reflection coefficient is less than -10dB, from 3.3GHz to 3.8GHz (percentage impedance bandwidth is 14%). The port isolation is greater than 20dB in the whole WIMAX™ frequency band.

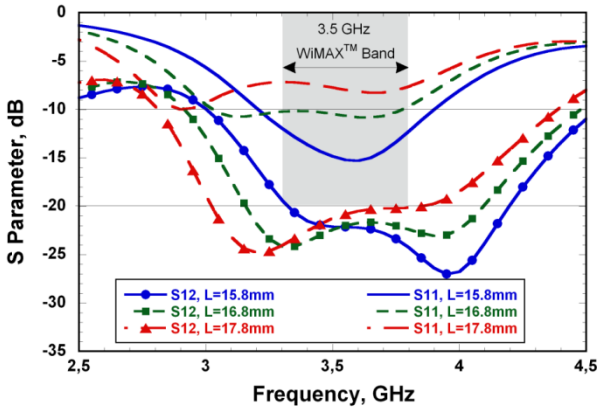

Figure 1.6 - Simulated S-parameters of the square ring slot fed patch as a function of the slot width, L.

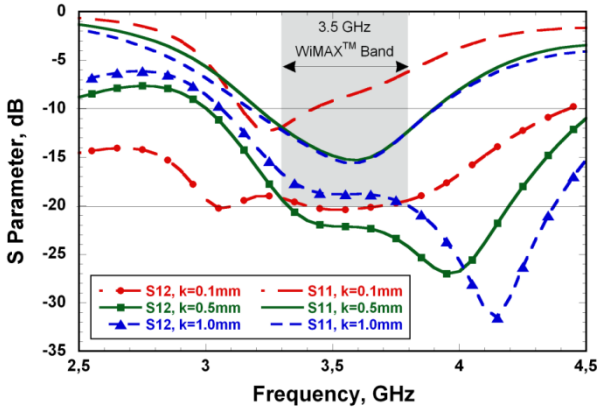

Figure 1.7 - Simulated S-parameters of the square ring slot fed patch as a function of the slot width, k.

Figure 1.6-7 show the most significant results of a numerical parametric analysis. Reflection coefficient and port isolation are plotted in Figure 1.6-7 as a function of slot

perimeter and width, respectively (while all other parameters are as those given in the paragraph 1.2.2). Performance dependence on other antenna geometrical parameters (as for example, patch size, stub length, layer thickness, etc.) is comparable to that already discussed in most of the papers relevant to the configurations shown in Figure 1.1.

In Figure 1.6 we can observe that the optimal value of L (edge of the slot, shown in Figure 1.2) is 15.8 mm. Indeed, in this case reflection coefficient is always well below -10 dB in the 3.3-3.8 GHz band; moreover slot and patch resonant-frequencies are positioned in order to create a single large bandwidth. When L is increased from 15.8 mm to 16.8 mm and then 17.8 mm, the slot resonant-frequency moves toward lower frequencies. For the last two values, S_{11} curves present two separate resonance peaks. Moreover, as can be seen from Figure 1.6, the patch resonance frequency remains unchanged at around 3.65 GHz. For all considered values of L, port isolation remains greater than 20 dB in the 3.5 GHz WIMAX™ band. In Figure 1.7, the numerical results of a parametric analysis with respect to the slot width (k parameter in Figure 1.2) are shown. The reflection coefficient is almost constant for values of k greater than 0.5mm. For k<0.5 mm worse performance is obtained. The isolation is greater than 20 dB until k is less than 0.5 mm.

Although the achieved port isolation is not as high as that obtained for "T" configurations [43]-[45], it is worth mentioning that even for a high performance slot-coupled single patch the port isolation reduces to less than 25dB [43] when the latter is arranged in antenna arrays, due to the mutual coupling effects.

To show the robustness of our solution in terms of port isolation performance, a small 2x2 array (Figure 1.8) has been designed and it has been verified that the port isolation for the array is still greater than 20dB as for the single element.

To better investigate the properties of the electric field distribution along the ring slot of the designed antenna, the simulated S_{12} parameter has been calculated when the square patch is removed. From the numerical results in Figure 1.9 it is apparent the port isolation dips at around 3.6GHz, which was expected on the basis of the discussion in the paragraph 1.2.2.

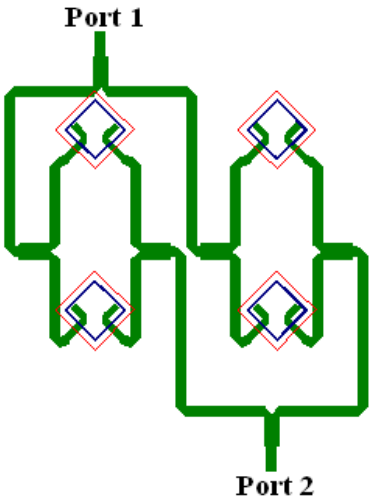

Figure 1.8 - (a) Comparison between the isolation of the dual-polarized single element in Figure 1.2 and that one of the dual-polarized 2x2 array shown in

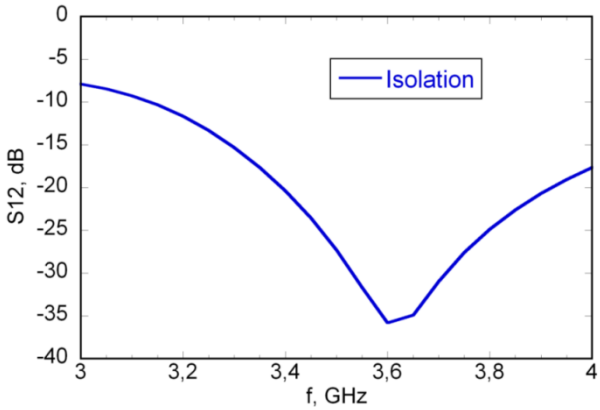

Figure 1.9 - Simulated S12 parameter of the square ring slot fed patch in Figure 1.2, when the patch has been removed.

It can be stated that the degraded isolation performance is due to a patch-induced coupling between the two orthogonal modes. On the other hand, it is worth mentioning

that by properly optimizing antenna parameters, a higher isolation could be obtained for those applications where a reduced impedance bandwidth can be accepted.

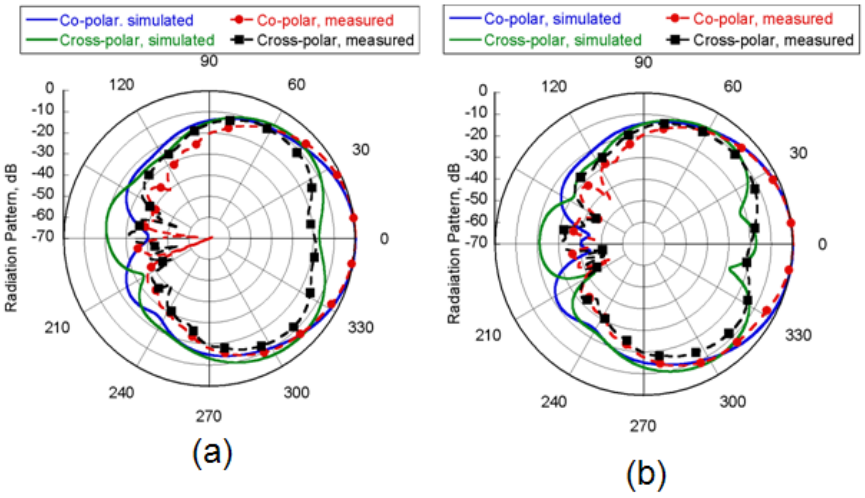

Figure 1.10 - Measured and simulated co-polar and cross-polar components for the square slot fed patch in Figure 1.2, at f=3.55 GHz when port 2 is fed: (a) □=45° plane and (b) □=-45° plane.

In Figure 1.10, the co-polar and cross-polar components of the radiation pattern, in the φ=45° and φ=-45° radiation planes, are shown, when port 2 is fed. The measured half power beamwidths at 3.55 GHz is around 56° in both principal planes, and cross-polar components are below -18dB at the broadside direction. The measured gain is between 8dB and 8.7dB in the band of interest (Figure 1.11). Similar results are obtained when port 1 is fed. Finally, we verified that the main beam is not depointing and the radiation pattern is almost symmetric, in an extended frequency range; this is as expected since the phase centre is the same for the square slot and the patch [46].

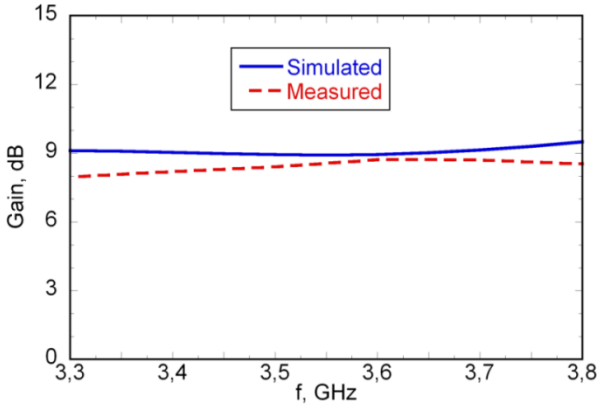

Figure 1.11 - Measured and simulated gain of the square ring slot fed patch in Figure 1.2, when port 2 is fed.

1.2.4 Conclusions

A novel slot-coupled patch fed through a square ring slot has been presented and design criteria have been discussed. Due to its simple structure, the patch described here can be used as the radiating element of medium and large planar arrays with dual linear polarizations (vertical/horizontal polarizations or ±45° slanted polarizations). Antenna performance has been shown by the design, fabrication and characterization of a patch operating at the 3.3-3.8 GHz WIMAX^{TM} frequency band. A port isolation of 20dB has been obtained, in a 500MHz frequency band (14% fractional bandwidth), with cross-polar level less than -18dB in the broadside direction. On the other hand, different geometrical parameter sets could be determined with reference to different specifications; in particular, we found that the final design of the proposed solution is a result of a trade-off between frequency bandwidth enlargement and isolation improvement. With respect to other slot-coupling feeding techniques for dual-polarized patch antennas, the configuration here proposed exhibits a simple structure and a valuable symmetry property with respect to the two feeding ports, while preserving a

satisfying isolation between the two input ports. Moreover, only one feeding network laminate is required, and the level of the coupling between the patch and the feeding line is increased with respect to configurations using (for each polarization) only one rectangular slot shifted with respect to the patch centre. Impedance bandwidth enlargement can be achieved by adding either stacked patches or other parasitic elements close to the main radiating patch, while preserving the original symmetry properties. Finally, due to the symmetry of the antenna layout with respect to the two feed ports, good axial-ratio performance can be obtained when it is used to radiate a circularly polarized field, as shown in [5] and [6], where a single feed and a double feed technique have been used, respectively.

1.3 A wideband slot-coupled stacked-patch array for wireless communications

1.3.1 Introduction

Recently some frequency bands have been assigned to upcoming wireless applications to guarantee the Broadband Wireless Access (BWA) together with traditional cellular and Local Area Network (LAN) services. Among them, the frequency band from 2500MHz to 2690MHz has been assigned to 3G mobile UMTS (Universal Mobile Telecommunications System) as an expansion band of the 1920-2170 MHz UMTS band. Moreover, the frequency band from 2300MHz to 2700MHz is reserved to WIMAX™ applications in some areas of the north and South America and in the all Asia. The newest installations of base station antennas have to afford the need to provide the area coverage for all above services and in this context it is preferable to avoid using one antenna for each system. For multi-service systems, wideband or multi-band antennas are needed when the lack of space is a determinant constraint or when buildings cannot be defaced by multiple antenna installations. Actual radiating systems provide multi-band operability for GSM and UMTS cellular services, with a maximum percentage bandwidth up to 25%. In addition to the multi-band element need, the antenna system is often requested to provide dual polarization capability. This is necessary to implement diversity at the base station, to compensate for the signal degradation due to multipath phenomena [47]. Diversity consists in using multiple antenna systems that receive two sufficiently uncorrelated copies of the signal and properly combine them at the receiver to increase the signal reliability. A multiple antenna system for diversity techniques that provides two uncorrelated received signals needs two input ports, which can be realized with two antennas placed at a certain

distance (spatial diversity) or with complementary radiation patterns. A space saving solution is gained with polarization diversity [48]. Much attention has been given to polarization diversity through analytical and experimental investigation, resulting in the observation that ±45° slanted polarizations are preferred to vertically/horizontally (V/H) polarizations because they form identical patterns in the azimuth plane and they are equally sensible to horizontally and vertically polarized signals.

This project proposes a two-element linear array of dual polarized wideband stacked patches fed through a novel slot coupling technique [2], where the patch is coupled to the feeding line through a square ring slot. The implementation of a sequential rotation technique and the symmetry properties of the slot-patch pair guarantee good performance in terms of the isolation between the two polarization ports and the level of the cross-polar components in both principal radiation planes. A single layer laminate is needed for the feeding network, since the square ring slot can be excited through two orthogonal non-overlapping microstrip lines. The final array operates in the GSM 1800-1900 band (1710 – 1910 MHz), UMTS band (1920 - 2170 MHz), ISM band (2400 - 2484 MHz) and UMTS 3G expansion band (2500 - 2690 MHz) or, alternatively, WIMAX™ band (2300 – 2700 MHz). The antenna has been designed and optimized by using Ansoft HFSS™. A prototype has been realized and measurements were carried out showing good performance in the whole required bandwidth (45% bandwidth, Reflection Coefficient < -10dB)). Simulated and measured results are shown for reflection coefficient, port isolation, antenna gain, and radiation patterns in the antenna principle radiation planes.

1.3.2 Antenna Design

Figure 1.12 shows the stack-up and the layout of the wideband slot-coupled stacked-patch array, together with the two feeding lines. A metallic reflector is needed to limit the back radiation and increase the antenna gain. Since the layout is symmetric with respect to the two input ports, identical radiation and input impedance properties are expected for the two ports.

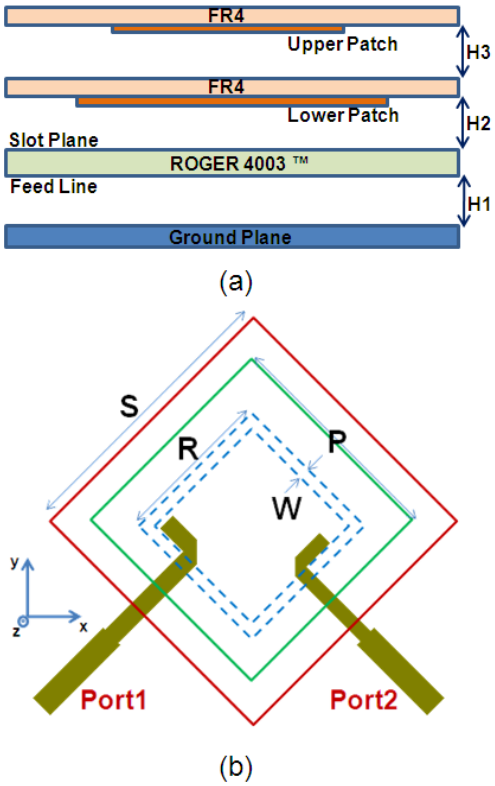

Figure 1.12 - Stack-up and top-view geometry of the wideband slot-coupled stacked-patch (H1 = 22mm, H2=10mm, H3 = 11mm, S = 45mm (lower plane), P = 35mm (upper plane), R =31mm (slot side), W = 0.5mm (slot width))

Both microstrip lines are printed on the lower side of a 1.524mm thick RO4003 Rogers substrate (ε_r=3.55, tgδ=0.0027). The square ring slot has a perimeter of 124mm, a 0.5mm width, and it is etched on the upper side of the above substrate, i.e. on the metallic ground plane separating the feeding lines from the lower square patch. As in other slot-coupled patch configurations [33], the ground plane prevents spurious radiation from the feeding network, and the length of the open-circuited stub behind the slot is optimized for input impedance tuning. The 45x45mm^2 lower patch is printed on the bottom layer of an FR4 laminate, which is 1.6mm thick; the upper 35x35mm^2 stacked patch is printed on the bottom layer of another FR4 laminate, which also acts as an antenna cover. The air gap between the slot plane and the lower patch, and that one between the driven patch and the stacked patch is 10mm and 11mm high, respectively.

By referring to port 2, the side of the ring slot that is directly fed and that one parallel to it (i.e. the -45° slanted sides of the ring slot shown in Figure 1.12b) are both excited, and the electric field induced into the two slot-sides are in phase and with a similar amplitude; as a consequence, due to above phase relationship and the symmetric position of the -45° slanted sides with respect to the patch centre, the fundamental resonant mode of the patch (that one associated to port 2) is properly excited and low cross-polarization level is expected. Moreover, the electric field distribution (Figure 1.13) induced into the two sides of the slot orthogonal to the previous ones (i.e. the +45 slanted sides of the ring slot shown in Figure 1.12) are out of phase and do not excite the orthogonal resonant mode of the patch (that one associated with port 1).

Finally, the induced electric field does vanish close to the centre of the -45° slanted sides of the slots; it means that a good port isolation is expected when that point is used to couple the square slot to the orthogonal feed line corresponding to port 1. The previous characteristics are apparently related to the fact that the square ring slot is resonating at the design frequency.

Two radiating elements are lined in a column with a separation equal to 100mm (0.9λ@2.7GHz). The overall size of the array panel is 125x200mm^2 and it is 45mm thick, giving the antenna a relatively low profile design. A 50 Ω microstrip line feeds both two elements of each column through one power divider for each polarization.

Starting from the feeding point, a 50Ω microstrip feeding line is transformed to a 25Ω one by a quarter-wavelength impedance matching line located just before the power divider. Quarter wavelength transformers are 24mm long and 6mm wide. To improve polarization purity and port isolation, the novel slot-coupling feeding technique has been combined with a sequential feeding technique [2] as suggested in [50]-[51]. Due to the symmetry of the antenna/slot configuration, the 90° rotation required by the sequential feeding technique does not apply to the radiating patches, but slight modifications are required at the feeding network level only.

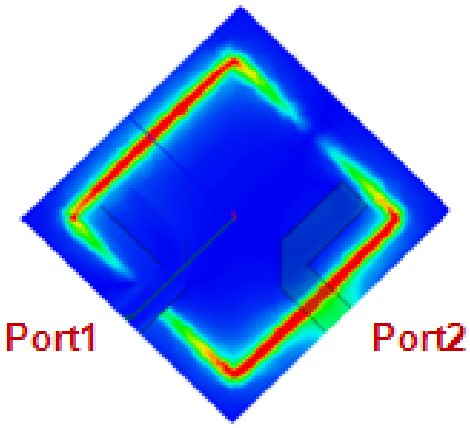

Figure 1.13 - Electric field distribution induced into the two sides of the slot when port 2 is fed.

1.3.3 Numerical and Experimental Results

Figure 1.14 shows the realized prototype and the corresponding layout. The 2x1 sub-array prototype (Figure 1.14c), was realized on a 125mm wide and 200mm long laminate with the same stack-up as in Figure 1.12a.

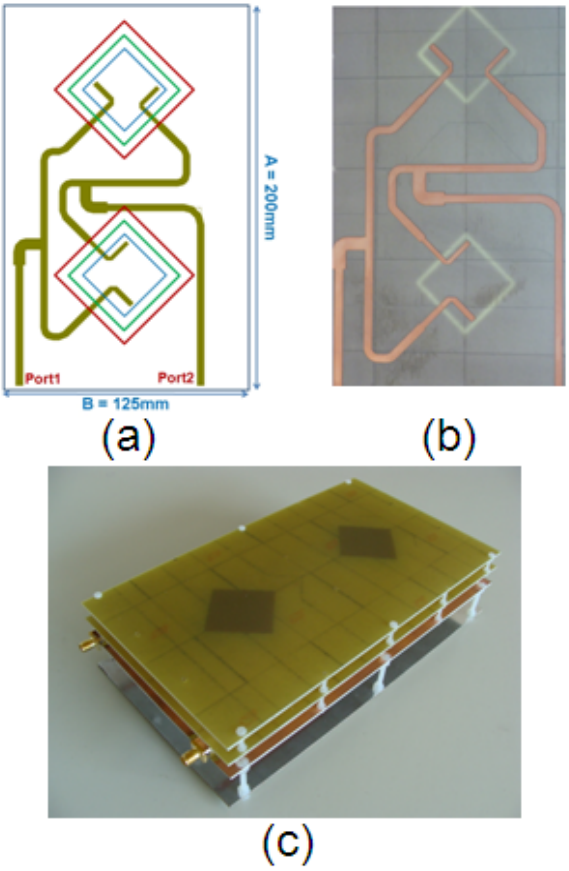

Figure 1.14 - Realized prototype of the wideband slot-coupled stacked-patch array. (a) Simulated 2x1 subarray. (b) Detail of feeding lines and coupling slots. (c) Realized 2x1 prototype.

The sequential rotation technique applies here only to a 2 port sub-array and its effect is consequently reduced with respect to a longer 2Nx1 array where better performance are expected. Reflection coefficient is less than -10dB in the whole frequency band from 1.71GHz to 2.69GHz, as shown in Figure 1.15, where a good agreement is visible between simulation results and measurements data except for a small difference due to imprecision in the prototype realization.

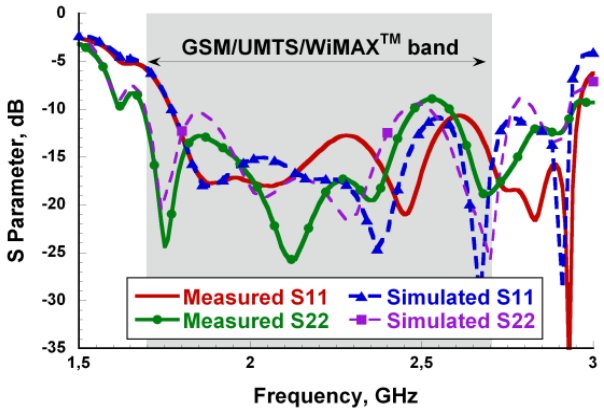

Figure 1.15 - Simulated and measured reflection coefficient for the wideband slot-coupled stacked-patch array.

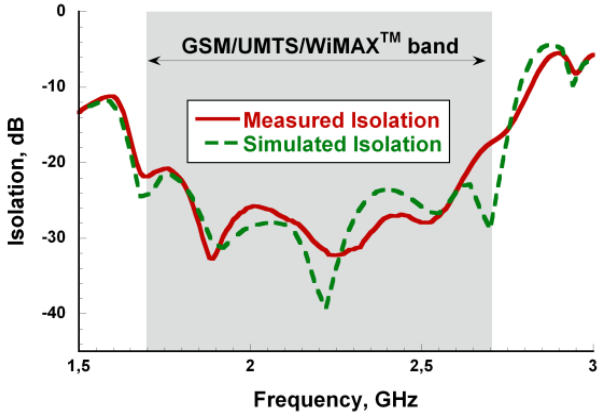

Figure 1.16 - Simulated and measured isolation for the wideband slot-coupled stacked-patch array.

The overall impedance percentage bandwidth (Reflection coefficient<-10dB) is greater than 45%. Both numerical and measured data are slightly different for the two ports because of some differences in the corresponding feeding lines mainly due to the sequential rotation technique applied to the +45° polarization microstrip line. The array port isolation, shown in Figure 1.16, is greater than 22dB in the whole frequency band of interest.

Figure 1.17 and Figure 1.18 show the co-polar and cross-polar components of the radiation patterns, at 2.2GHz, in the azimuth (φ = 0) and elevation (φ = 0) planes, respectively, when port 1 is fed.

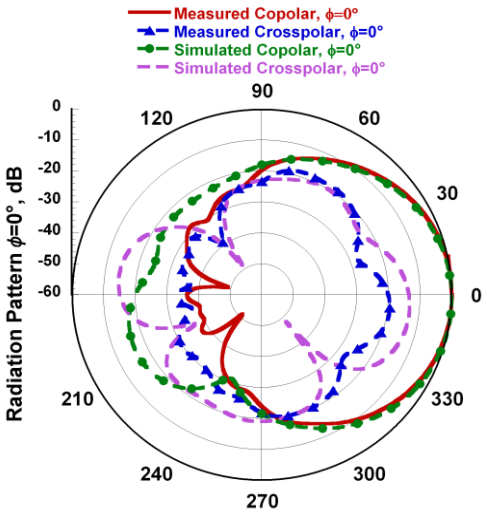

Figure 1.17 - Copolar and crosspolar radiation pattern in the azimuth plane for the wideband slot-coupled stacked-patch array, at 2.2 GHz when port 1 is fed.

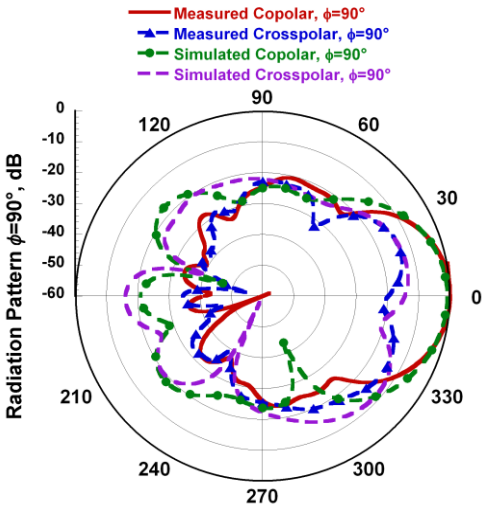

Figure 1.18 - Copolar and crosspolar radiation pattern in the elevation plane for the wideband slot-coupled stacked-patch array, at 2.2 GHz when port 1 is fed.

The relative amplitude of the cross-polar components is less than -20dB. Half Power Beam Width (HPBW) is 61° in the azimuth plane and 36° in the elevation plane. The antenna gain for Port 1 (Figure 1.19) is between 8dB and 11dB in the entire band of interest. Similar results have been obtained for the orthogonal polarization (when port 2 is fed).

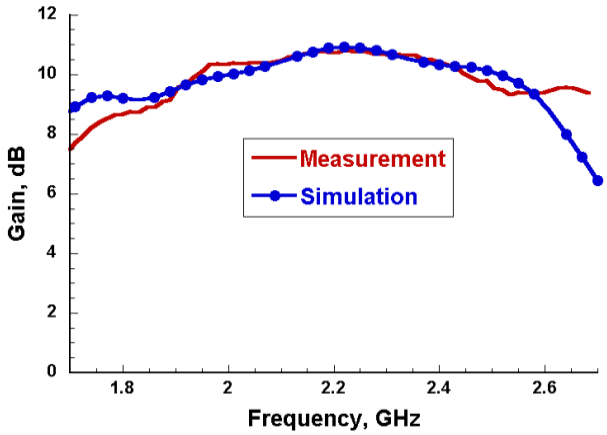

Figure 1.19 - Simulated and measured gain for the wideband slot-coupled stacked-patch array (when Port 1 is fed).

In Table 1.1 - Gain and HPBW for the wideband slot-coupled stacked-patch array.

HPBW and antenna gain are summarized in Table 1.1.

Frequency, MHz	Gain, dB	HPBW, deg (Horizontal Plane)
1800	8.7	60°
2050	10.4	61°
2400	10.4	57°
2500	9.5	56°
2600	9.3	55°

Table 1.1 - Gain and HPBW for the wideband slot-coupled stacked-patch array.

We can observe that the HPBW in the horizontal plane is quite stable in the whole antenna operating band.

1.3.4 Conclusions

A 2x1 array module of wideband dual-polarization stacked-patch antennas working between 1.71GHz and 2.69GHz (percentage bandwidth greater than 45%) has been described in this paragraph. The array is intended as a module for any 2Nx1 linear array to be composed on the basis of gain requirements for base station antennas. The radiating elements are fed through a novel slot coupling technique and a sequential feeding technique has been implemented for each patch pair. As a result, good isolation and cross-polarization purity performance are obtained, as required by the specifications for dual-polarization base station antennas. Array performance was analyzed by numerical simulations and a prototype was realized. A measurement campaign was conducted to evaluate reflection coefficient, isolation, radiation patterns and antenna gain. Simulated and experimental results are in quite good agreement and they exhibit low crosspolar components and a relatively high isolation.

1.4 A Circularly Polarized 2x2 Array

1.4.1 Introduction

In microwave radio links, circular polarization is able to reduce multipath effects. It also allows more flexible reciprocal orientations between the transmitting and the receiving antennas. For the above reasons, circularly polarized (CP) antennas are used in a number of communication systems, as for example GPS (Global Positioning System) terminals and satellite-to-mobile wideband communication links, as well as UHF RFID (Radio Frequency IDentification) readers. Moreover, a number of ATC (Air Traffic Control) radars and SAR (Synthetic Aperture Radar) systems adopt CP antennas, exploiting some interesting properties of the polarimetric scattering. CP patch antennas are generally divided into two categories, named as single-feed and dual-feed configurations. Both these configurations are able to excite the patch orthogonal principal modes with a quadrature phase shift. Dual-feed layouts resort to an external power splitter (for example a reactive power divider or a 90° quadrature hybrid). On the other hand, single-feed configurations are based on a single feed and perturbation segments that are applied to the patch boundary. Typical single-feed configurations are the corner truncated patch and the nearly square patch with the feeding point located along the patch axes or diagonals. Single-feed solutions are simpler but exhibit a limited Axial Ratio (AR) bandwidth [52]. On the contrary, the dual-feed technique results in a larger AR bandwidth [39], [53] at the expense of a more complex feeding network, which is a substantial drawback in electrically large array antennas.

In the paragraph 1.4.2, a patch antenna using a novel slot-coupling technique (firstly introduced in [2] for dual-linear polarization patch antennas) is used to realize a CP 2x2 array with wide impedance matching and AR bandwidths. Specifically, a dual-feed

technique is used for each array element, and it is combined with a sequential rotation array feeding technique [54]-[56]. The sequential rotation technique consists in sequentially rotating each patch element together with imposing an appropriate offset in the feed excitation phase. Sequential rotation feeding can be used to improve cross polarization (circular polarization purity), radiation pattern symmetry and impedance bandwidth, also providing improved port isolation in dual-circular polarization arrays [49]. Numerical simulations obtained with Ansoft Designer^{TM} are used to show the remarkable AR performance of the 2x2 array. The above described improvements are obtained at the cost of a moderately increased feeding network complexity. Numerical results are validated through comparisons with measurements performed on an array prototype.

1.4.2 Antenna Design and Experimental Results

2x2 square array with an inter-element distance equal to 72mm (about $0.85\lambda_0$, where λ_0 is the free space wavelength at the centre of the WIMAX^{TM} frequency band) has been analyzed in this paragraph. Preliminary numerical results have been obtained by feeding each array element with an ideal 90° phase shifter (in the numerical tool, Port1 and Port2 of the (n,m) array element have been fed with an input current equal to $I_{n,m}$ and $I_{n,m}\exp(+j\pi/2)$, respectively). The radiating element has been used in a conventional 2x2 array ($I_{n,m}=1$, with n=1,2 and m=1,2) and later on in a 2x2 sequentially rotated array ($I_{1,2}=\exp(+j\pi/2)I_{1,1}=-I_{2,1}$, $I_{2,2}=-I_{1,1}$, and each patch is 90° rotated with respect to the adjacent one): in both cases the array was constituted by four patches and four ideal 90° phase shifters. The use of ideal phase shifters instead of a microstrip feeding network allows us to avoid AR performance degradation due to phase shift errors in the element feeding currents; nevertheless, mutual coupling between array patches is still accounted for. The conventional 2x2 array (where the four array elements are fed in-phase) exhibits very good AR performance with respect to both frequency and angular

deviation from broadside direction, θ. From the numerical results shown in Figure 1.20, it results that the simulated AR at the broadside direction is less than 2.25dB in the whole frequency band, and its variations within the array beam are less than 0.5dB, in both principal radiation planes at ϕ=0° and ϕ=90°. Such a good performance is in some way related to the symmetry properties of the novel slot-coupling feeding technique [2].

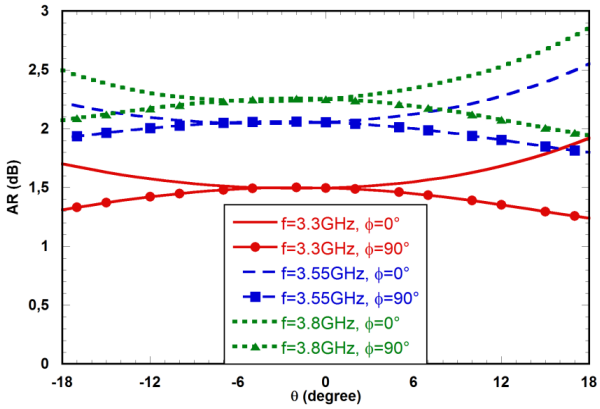

Figure 1.20 - AR for a 2x2 conventional array (without sequential rotation) and with ideal phase shifters (without microstrip feeding network). AR is plotted vs. the angular displacement from broadside, θ, for different frequency values (3.3GHz, 3.55GHz and 3.8GHz), and in both principal radiation planes (ϕ=0° and ϕ=90°).

Simulation results also showed a stable half-power beamwidth (HPBW), versus frequency, in both principal planes. Indeed, we observed a HPBW of 32° at the central frequency, 3.55GHz, with variations of less than 2° in the WIMAX™ frequency band. The array gain is about 13dB in the broadside direction (θ=0°). When the four array elements are sequentially 90° rotated and fed with a proper phase shift, as required by the sequential rotation technique, the same performance in terms of HPBW and gain is obtained as for the conventional 2x2 array. On the other hand, it is apparent from the results in Figure 1.21 that the AR at broadside becomes less than 0.03dB over the whole WIMAX™ frequency band. Moreover, AR variations with respect to the angle θ are

less than 0.5dB, in the whole frequency band and in both the ϕ=0° and the ϕ=90° radiation planes.

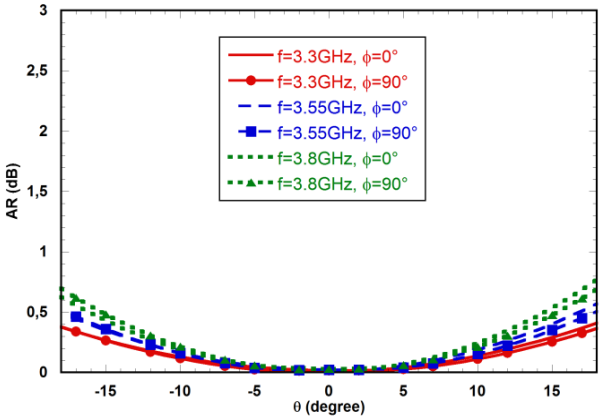

Figure 1.21 - AR for a 2x2 array with sequential rotation and with ideal phase shifters (without microstrip feeding network). AR is plotted vs. the angular displacement from broadside, θ, for different frequency values (3.3GHz, 3.55GHz and 3.8GHz), and in both principal radiation planes (ϕ=0° and ϕ=90°).

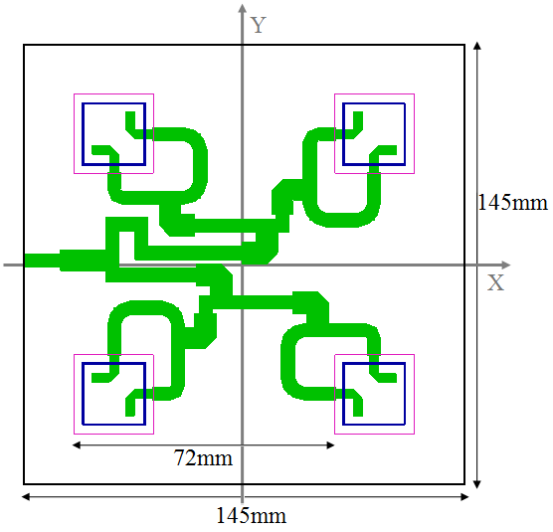

Figure 1.22 - Layout of the 2x2 sequentially rotated CP array.

Above results confirm that the sequential rotation technique can significantly improve AR performance, giving an improvement of about 2dB with respect to the

conventional 2x2 array. Finally, a sequentially rotated 2x2 array with a complete microstrip feeding network has been designed, as shown in Figure 1.22. Each dual-linear polarized patch has been fed through a reactive 3dB power divider that includes two microstrip lines whose lengths differ of $\lambda_g/4$, where λ_g is the microstrip wavelength (λ_g=52mm, microstrip wavelength at 3.55GHz).

The power divider also includes a quarter-wavelength impedance transformer (6mm wide and 12.6mm long microstrip line). The feeding network consists of microstrip lines whose lengths have been adjusted to achieve the required 90° current phase difference between adjacent elements. A prototype of the array has been fabricated and a photo is shown in Figure 1.23.

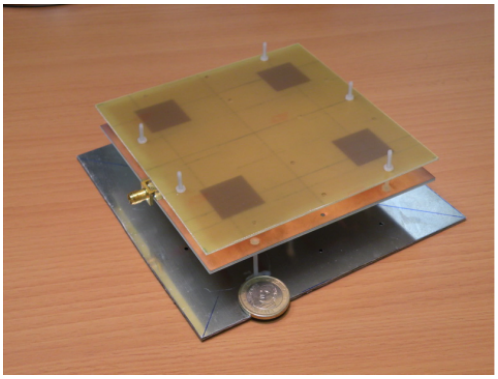

Figure 1.23 - A prototype of the 2x2 CP array.

The reflection coefficient for the 2x2 CP array is shown in Figure 1.24.

It is apparent that the measurements and the numerical data are in a very good agreement; except for a frequency shift which has been often noted when using an electromagnetic tool that considers infinite dielectric layers. In the whole WIMAX™ frequency band, the measured reflection coefficient is less than -10dB. As apparent from Figure 1.25, the maximum measured gain is about 12.8dB.

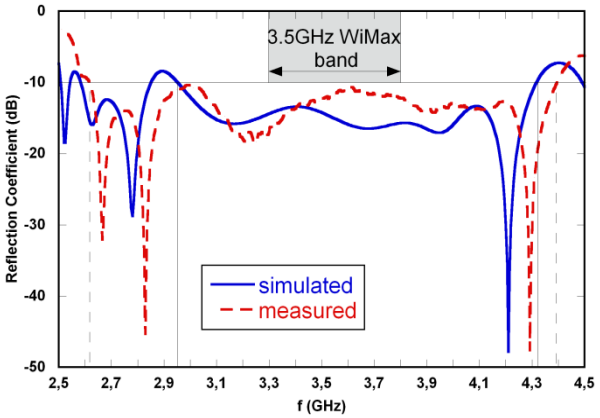

Figure 1.24 - Simulated (solid line) and measured (dashed line) reflection coefficient for the 2x2 CP array in Figure 1.23.

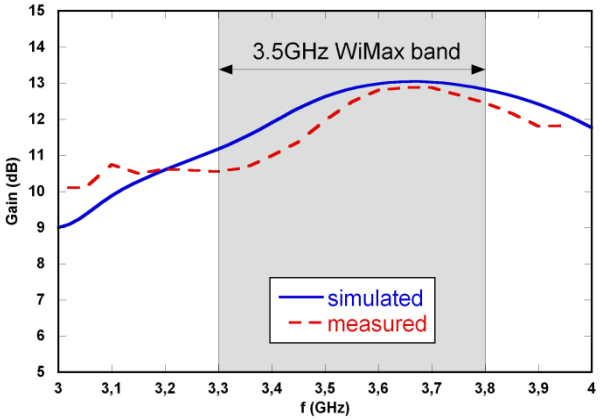

Figure 1.25 - Simulated (solid line) and measured (dashed line) broadside gain vs. frequency for the 2x2 CP array in Figure 1.23.

Figure 1.26 illustrates the simulated and measured array radiation patterns, in the ϕ=0° plane, at 3.55GHz. The antenna radiates a Right Hand Circular Polarization (RHCP) and the measured cross-polar component (LHCP, Left Hand Circular Polarization) is less than -20dB within the HPBW which is equal to 28° (a little bit smaller than the simulated one which is equal to 32°).

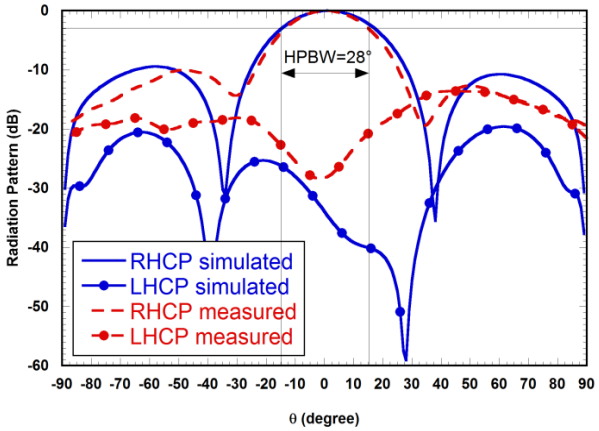

Figure 1.26 - Simulated (solid line) and measured (dashed line) normalized radiation pattern for the 2x2 CP array in Figure 1.23, in the φ=0° principal plane, at 3.55GHz: RHCP (without markers) and LHCP (with markers).

The measured and simulated AR, versus the frequency and the angle from broadside θ, are shown in Figure 1.27 and Figure 1.28, respectively. In the broadside direction, the measured AR is less than 1.35dB in the whole WIMAX™ frequency bandwidth, and the 3dB AR bandwidth is of about 30%. The measured AR is less than 2.25dB at the centre frequency (3.55GHz), for any direction within the array main beam, and in both the ϕ=0° and the ϕ=90° radiation planes.

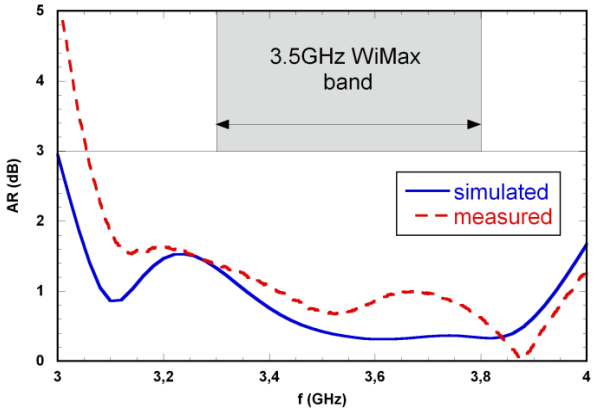

Figure 1.27 - Simulated (solid line) and measured (dashed line) Axial Ratio vs. frequency for the 2x2 CP array in Figure 1.23 (at the broadside direction, θ=0°).

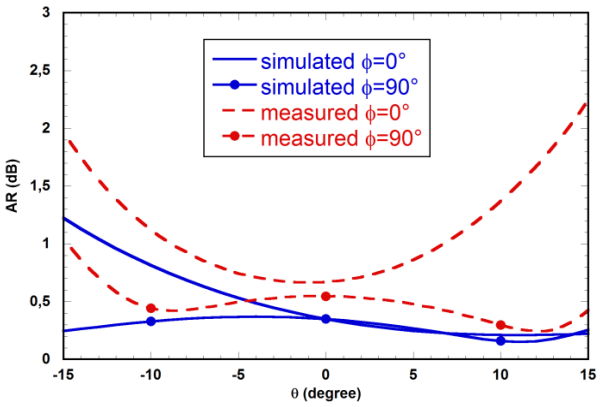

Figure 1.28 - Simulated (solid line) and measured (dashed line) Axial Ratio vs. the θ angle, for the 2x2 array in Figure 1.23, at the centre frequency (3.55GHz) and in both principal planes: φ=0° (without markers) and φ=90° (with markers).

1.4.3 Conclusions

A dual-feed square patch coupled to the microstrip feeding line through a square ring slot has been used to realize a circularly polarized 2x2 array. To obtain a wide impedance bandwidth as well as a wide axial ratio bandwidth a sequential rotation feeding technique has also been adopted. Simulation and measurement results for an array designed to operate in the WIMAX™ frequency band have shown that both an AR<3dB and a return loss greater than 10dB can be obtained. In particular, the measured 3dB AR percentage bandwidth results to be as high as 30%.

Chapter II

2 DUAL-BAND PIFA FOR WIRELESS COMMUNICATIONS SYSTEMS

2.1 Introduction

In recent years, specific attention has been focused on terrestrial high definition television services and applications. The DTV (Digital TeleVision) and the European DVB-T (Digital Video Broadcasting-Terrestrial) standards are rapidly becoming very popular and they are nowadays the only terrestrial television service available in many regions [58]. Next generation terminals will be required to have an integrated antenna in order to avoid cabled connections and to render them relatively portable (at least within an indoor scenario). In addition to this, a web access through a Wireless Local Area Network (WLAN) could be provided to guarantee access to on-demand services. Therefore, dual-band compact integrated antennas for DVB-T and WLAN applications represent a valuable solution.

A number of DTV wideband antennas have been recently presented [59]-[65], which are mainly low cost and low profile and of easy fabrication printed monopoles and patch-alike antennas. Printed monopoles require a careful positioning inside devices with high circuitry density, as they are quite sensitive to the presence of close by metal

parts. On the other hand, patch-alike antennas and PIFAs are suitable for integration because their ground plane also acts as a shield.

In this communication, a dual-band PIFA operating in both the DVB-T (470–862 MHz, 59% percentage bandwidth [58]) and the WLAN (2400-2484 MHz, 2.7% percentage bandwidth) frequency bands is presented, which is suitable to be integrated into devices, such as a monitor or a TV chassis, where relatively large volumes are often available along their sides or top. The proposed solution exploits the working principle recently proposed for an UWB PIFA [66], which is characterized by a driven (fed) radiating element separated by a small gap from a coplanar parasitic branch. In [66], the driven PIFA element acts as the primary element, governing the lowest resonant frequency, while the higher resonant frequency is controlled by the parasitic element. The proper dimensioning of the driven and parasitic branches and of the separating gap allowed us to get a compact dual-band antenna design. The extent of the antenna proposed in [66] was also reduced. In modern displays, the available volume in a monitor chassis has a transverse area usually less than 15mmx10mm, while almost its entire border length is accessible. Consequently, in this work, it was assumed that a volume less than 250 x 15 x 10 mm3 should be occupied by the radiating element.

2.2 Compact Dual-Band PIFA for DVB-T and WLAN Applications

2.2.1 Introduction

DVB-T PIFAs have been recently proposed [67]-[68]. In [67], the radiating patch and the ground plane are not facing each other, as it happens in conventional PIFAs, but they are orthogonal. This could result in high coupling with the circuitry, if the latter results to lie in close proximity. The antenna structure proposed in [68] looks more as a multi-antenna system (two radiating elements are separately fed and coupled to a third parasitic one). The PIFA here proposed is electrically smaller than the element in [68], where the parasitic patch and a wide ground plane increase the entire antenna volume. In addition, it offers dual-band functionality as it operates also in the 2.4 GHz IEEE 802.11b,g WLAN band, so that a single antenna can guarantee access to both TV and internet services, while simplifying terminal chassis design. To the best of authors' knowledge, dual-band radiating elements for DVB-T and WLAN applications have not been proposed yet.

The proposed PIFA layout is presented in the paragraph 2.2.2, where numerical data and experimental measurement results on two prototypes are also shown. In particular, the robustness of the solution in terms of antenna impedance matching against detuning effects that can be caused by the presence of surrounding metal parts is discussed.

Simulation results have been derived by CST Microwave Studio.

2.2.2 Antenna Design and Experimental Results

Figure 2.1 shows the layout of the proposed PIFA and Table 2.1 summarizes its main dimensions. The layout resulted from an optimization process focused to reduce the overall antenna dimensions as much as possible.

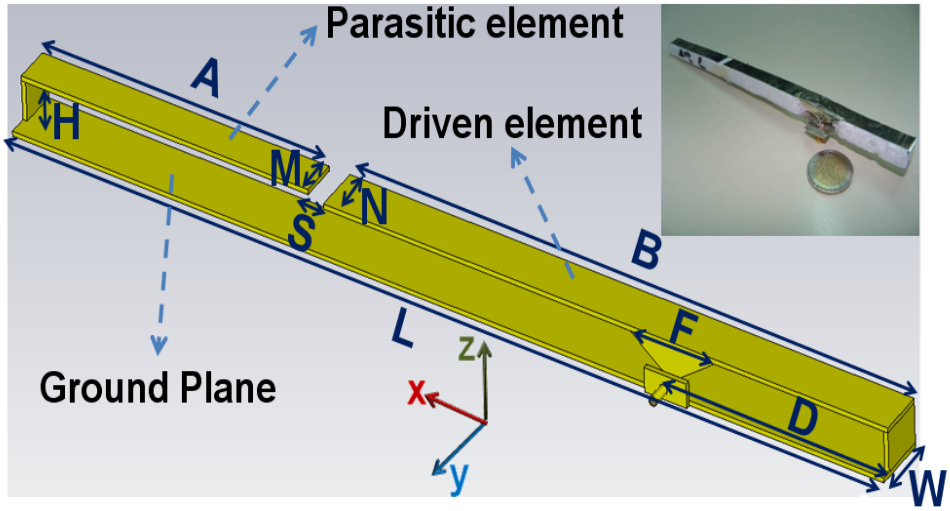

Figure 2.1 - Geometry and prototype of the proposed dual-band PIFA (the SMA connector model is also shown).

L	207	M	10
W	12	B	133
H	8	N	10
S	5	D	51
A	69	F	10

Table 2.1 - PIFA dimensions (MM)

The antenna is cut from a single metal sheet (even the trapezoidal feed plate is part of it) in the required planar geometry/shape and then it is properly bent to obtain the

final 3D structure. This simplifies the industrial fabrication and avoids any soldering, except for that at the antenna connector.

Similarly to the antenna in [66], the proposed PIFA is characterized by a driven radiating element separated by a small gap from a coplanar parasitic branch. The driven PIFA element acts as the primary element, governing the lowest resonant frequency, while the upper resonant frequency close to the DVB-T band is controlled by the parasitic element. Moreover, the separating gap helps in controlling a third resonance around 2.45 GHz in the IEEE 802.11b,g band for WLANs. Thus, as an improvement of the solution in [66], the proposed PIFA exhibits a dual band functionality. Moreover, if compared with [66], a significant reduction of 63% and 87% was achieved for the electrical thickness (*H*) and width (*W*), respectively (the electrical size is referred to the wavelength at the DVB-T band centre frequency, where λ=448mm) at the cost of only 9% length (*L*) increase.

The linear PIFA occupies an overall volume of 207 x 12 x 8 mm^3. This radiating element is relatively large with respect to antennas printed or mounted on high permittivity substrates but, at the same time, it can guarantee higher gains and efficiencies.

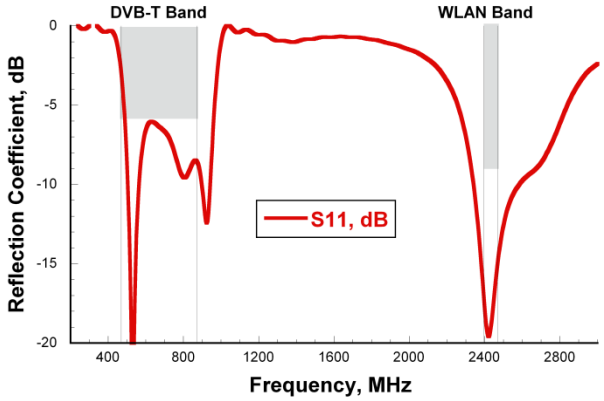

Figure 2.2 - Simulated reflection coefficient for the proposed dual-band PIFA.

As shown in Figure 2.2, the reflection coefficient is below -6 dB in the whole DVB-T band, and less than -10 dB in the IEEE 802.11b,g band.

The above values are typical thresholds for integrated antennas for such communication standards. It is worth noting that wideband performance in the DVB-T band (59% percentage bandwidth) is achieved through a careful tuning of two distinct main resonances. On the basis of a parametric analysis, the main parts for the antenna optimization were identified. The driven and parasitic elements jointly contribute to determine the two resonances at the DVB-T band. They can be controlled by varying the W, H and L parameters.

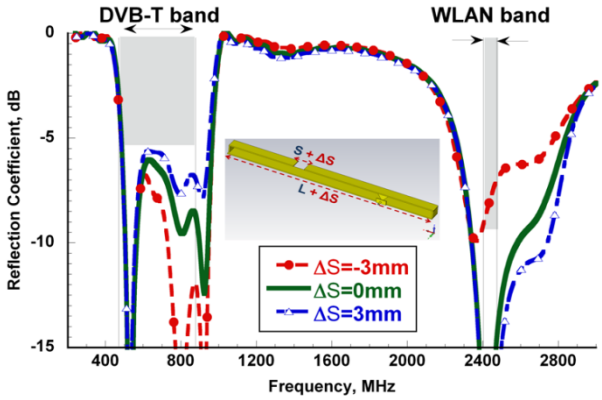

Figure 2.3 - Simulated reflection coefficient of the proposed dual-band PIFA as a function of frequency for different values of ΔS.

Figure 2.3 shows the reflection coefficient behaviour with respect to frequency for different values of Δ*S* between -3 mm and 3 mm (see Figure 2.3 for Δ*S* meaning). The gap S between the two elements, mainly affects the antenna reflection coefficient at the IEEE 802.11b,g band.

The reflection coefficient is plotted in Figure 2.4 and Figure 2.5 for different values of the M and N parameter, respectively. It is worth noting that these parameters affect the reflection coefficient values both in the IEEE 802.11 and in the DVB-T bands. Indeed, M and N variations cause the resonant frequency to shift in the IEEE 802.11b,g band and the reflection coefficient values to increase at the DVB-T frequencies. In particular, it is observed that M and N values greater than 10mm determine similar

performances in terms of reflection coefficient values and this minimum value is obviously preferred in order to minimize the total volume of the antenna. By varying the feed distance from the short-circuit, D, no effects are visible in the DVB-T band. However D is effective for fine tuning at 2.4 GHz. The parameter A affects both the resonance in the WLAN band and the second of the two resonances in the DVB-T band.

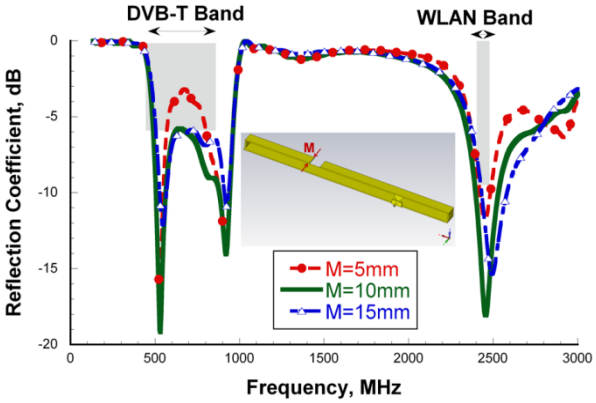

Figure 2.4 - Simulated reflection coefficient of the proposed dual-band PIFA as a function of frequency for different values of the parameter M.

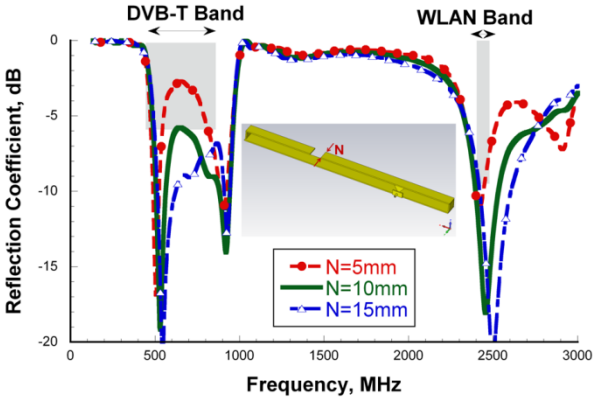

Figure 2.5 - Simulated reflection coefficient of the proposed dual-band PIFA as a function of frequency for different values of the parameter N.

The gain and the radiation patterns in the principal planes (co-polar and cross-polar components) are shown in Figure 2.6-8 for the centre frequencies of the bands of interest.

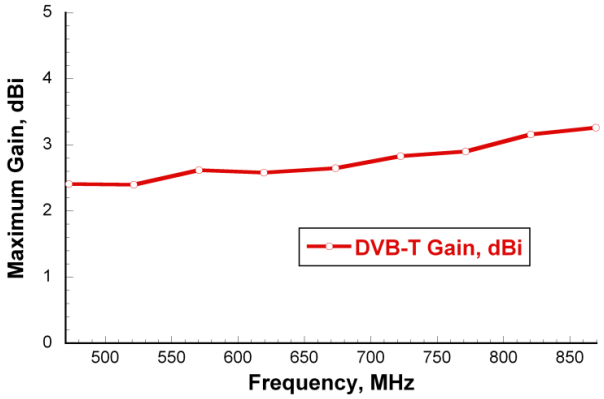

Figure 2.6 - Simulated gain for the proposed dual-band PIFA in the DVB-T band.

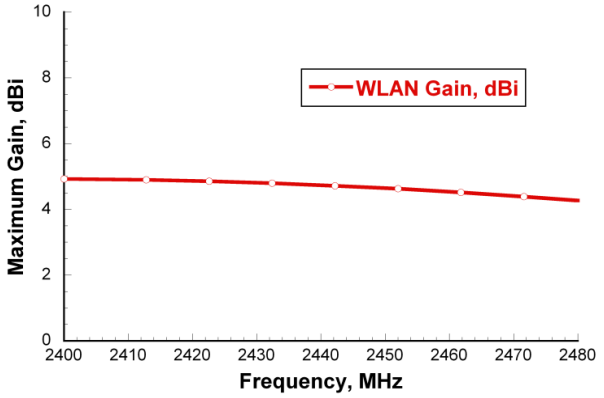

Figure 2.7 - Simulated gain for the proposed dual-band PIFA in the WLAN band.

The antenna gain is between 2.4 dBi and 3.3 dBi in the DVB-T band, and between 4.4 dBi and 4.8 dBi in the WLAN band. Radiation patterns have different shapes in the two frequency bands.

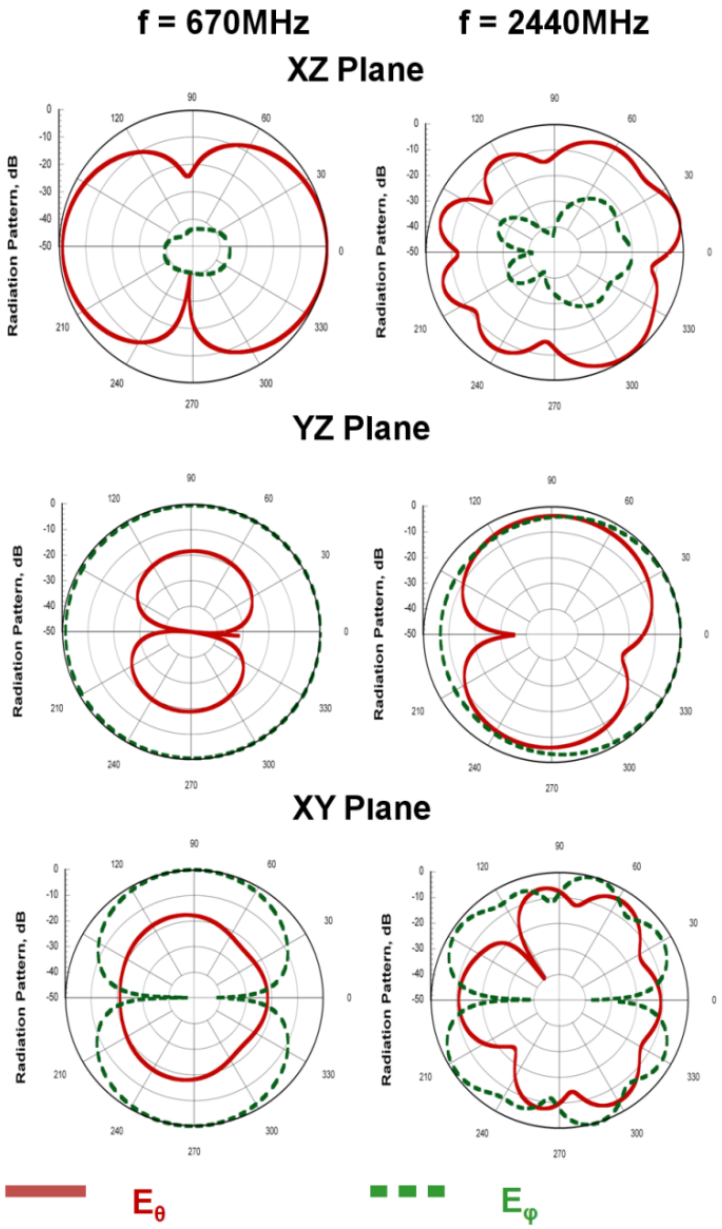

Figure 2.8 - Simulated radiation patterns (components E_θ and $E\varphi$) in the principal planes at 670 MHz (central frequency for the DVB-T band) and 2440 MHz (central frequency for the IEEE 802.11b,g band) for the proposed dual-band PIFA.

At lower frequencies, in the DVB-T band, the antenna behaves like a dipole with main lobes along broadside directions and nulls in the endfire ones. An omni-directional pattern is observed in the plane transverse to the antenna (yz-plane). At higher frequencies the antenna is electrically longer, high side lobes occur and no main beam can be identified. Cross-polar component levels are always below -18dB in the DVB-T band, while in the IEEE 802.11 band they cannot be distinguished in some planes (see for instance the xy-plane). However, since the terminal where the antenna has to be integrated is often an indoor device operating in a rich multipath environment, radiation patterns are not required to have specific properties in terms of beam width/shape and cross-polar levels.

On the other hand, when the antenna is integrated into the device, radiation patterns would be furtherly deformed, exhibiting higher cross-polar components, by the presence of internal parts of the monitor chassis.

A first prototype (*Prot.1*) was realized with a 0.4mm thick adhesive copper tape, cut and folded around a 207 mm long, 12 mm wide and 8 mm high polystyrene block (Figure 2.1). Measured reflection coefficients are shown in Figure 2.9, and compared with simulated results. The first prototype (*Prot.1*) exhibits a WLAN operating band slightly up-shifted with respect to simulation data.

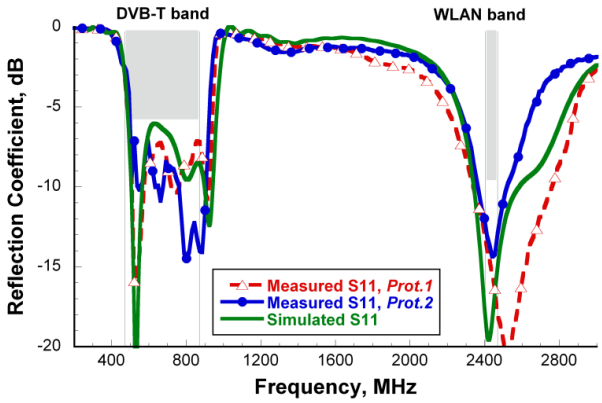

Figure 2.9 - Simulated and measured reflection coefficient for the proposed dual-band PIFA.

Then, a tuning of some geometrical parameters has been used to achieve another prototype with the desired performance between 2400 MHz and 2484 MHz *(Prot.2)*. Both prototypes satisfy reflection coefficient requirements (< -10dB) in the WLAN frequency band and they both could be used. However, even if its band is narrower than that of *Prot.1*, *Prot.2* exhibits a lower reflection coefficient in the WLAN band. Moreover, it is worth noting that introducing *Prot.2* also allowed us to show that, by varying some parameters (see Table 2.2), the highest antenna resonant frequency (close to the WLAN band) can be suitably controlled.

Prot.2 dimensions are listed in Table 2.2, together with the corresponding percentage variation with respect to the antenna dimensions derived from the numerical analysis (Table 2.1). The final space occupation for the tuned prototype is 217 x 12 x 8 mm^3 (*L x W x H*).

L	217 (+5.8%)	M	10
W	12	B	140 (+5.2%)
H	8	N	10
S	5	D	53 (+3.9%)
A	72 (+4.3%)	F	10

Table 2.2 - Antenna Prototype Dimensions (MM) for Prototype 2 and Corresponding Variations with Respect to Dimensions in Table 2.1

A further experimental analysis consisted in measuring the reflection coefficient variations when a metallic obstacle is located close to the antenna. In particular, a large metallic plate (300mmx400mm) was positioned in the vicinity of the antenna, at distances of 1cm, 2cm and 3cm, as shown in Figure 2.10-12.

It is apparent that the reflection coefficient variations are minimal, except for the cases in Figure 2.11, where the reflection coefficient goes up to -5dB in the DVB-T band.

Among the three studies presented in Figure 2.10-12, the one in Figure 2.11 needs to be more deeply analyzed and carefully considered when designing the integrated

system, since it is the one in which the PIFA is more sensitive and reflection coefficient requirements are not fully satisfied.

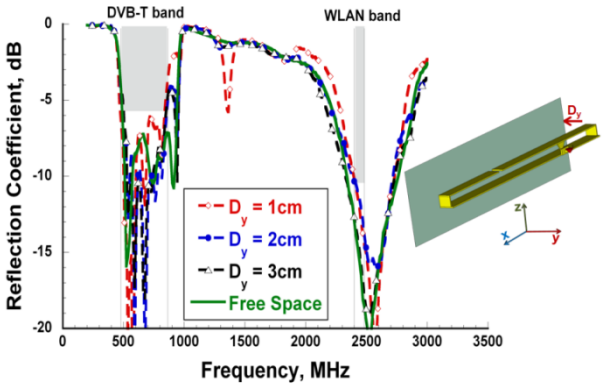

Figure 2.10 - Measured reflection coefficient for the proposed dual-band PIFA in the presence of a large metallic plate, as a function of the distance Dy.

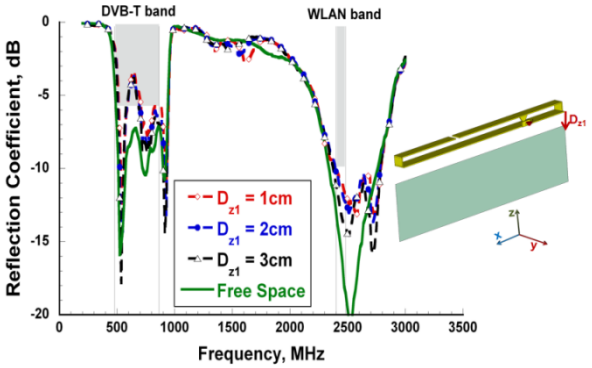

Figure 2.11 - Measured reflection coefficient for the proposed dual-band PIFA in the presence of a large metallic plate, as a function of the distance Dz1.

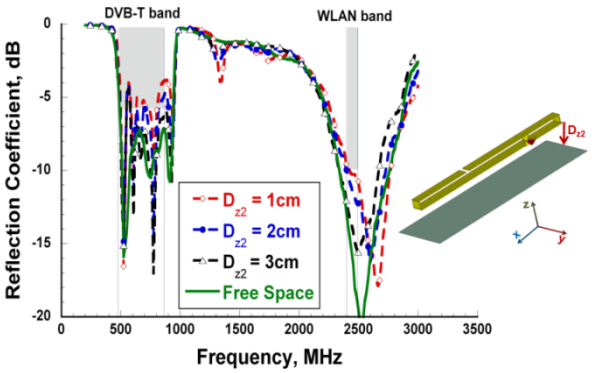

Figure 2.12 - Measured reflection coefficient for the proposed dual-band PIFA in the presence of a large metallic plate, as a function of the distance Dz2.

2.2.3 Conclusions

A compact dual-band Planar Inverted-F Antenna working in both the DVB-T band (470-862 MHz) and the IEEE 802.11b,g band (2400–2484 MHz) has been presented. It was designed to meet space requirements typically required for integration along the border of display-equipped devices. The antenna exhibits good impedance matching performance, with a reflection coefficient less than -6 dB in the DVB-T frequency band and less than -10dB in the IEEE 802.11b,g band. A prototype was realized through a single cut of a properly folded copper tape. The linear PIFA fills an overall volume of 217 x 12 x 8 mm^3. The robustness of the solution in terms of reflection coefficient variations with respect to the presence of near metal parts has been analyzed and checked through measurements.

2.3 Dual-Band L-Shape PIFA for Display-Equipped Devices

2.3.1 Introduction

A linear-shape PIFA working in the DVB-T and WIMAX frequency bands has been presented in [18]. Moreover, an alternative layout for a dual-band linear-shape PIFA has been more recently proposed in [20], for an antenna operating in the DVB-T and WLAN frequency bands. Since the PIFAs in [18], [20] cannot be made shorter less than 20cm while still getting an acceptable input impedance matching at the DVB-T frequency band, some other layout modifications are needed for integration into those devices with a length of the monitor sides not greater than 13-15 cm, or when part of the space along the monitor border is occupied by a webcam or a microphone. In such cases, a possible modification of the antenna layout with respect to that in [18], [20] is based on conforming the antenna to the shape of one of the device corners (a few preliminary simulation results were presented in [21]). In this letter, both numerical simulations and experimental results for an L-shape PIFA layout derived from that in [20] are presented, to show that the modified layout can be a valuable solution for monitor-equipped devices with an extent smaller than 15cmx15cm. Simulation results have been derived by using CST Microwave Studio commercial tool.

2.3.2 Antenna Design and Experimental Results

Starting from the dual-band linear-shape PIFA described in [20], a modified layout suitable to be integrated along the corner of a compact monitor-equipped device is presented. In [18]-[21], it has been verified that the total length L of a linear PIFA is a key parameter for DVB-T applications, and it should be greater than 20cm to get satisfactory VSWR performance in the whole DVB-T frequency range. It is worth noting that the new L-shape antenna configuration cannot be obtained by simply bending the antenna in [20], since all the basic antenna geometrical parameters need to be modified to optimize antenna performance (Figure 2.13).

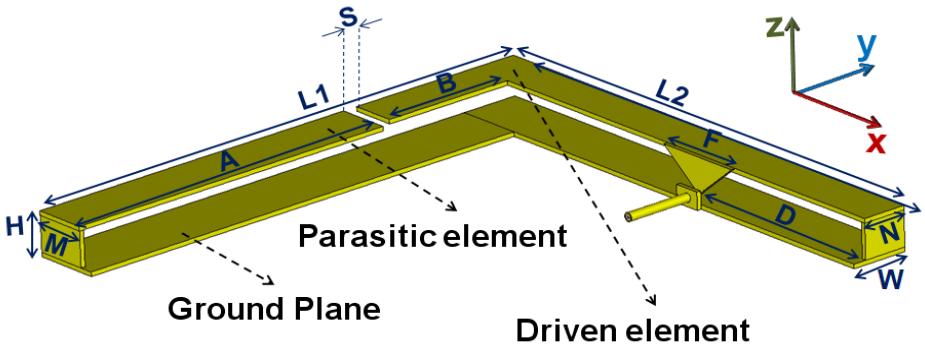

Figure 2.13 - Geometry of the proposed dual-band L-shape PIFA: L1=120mm, L2=116mm, W=13mm, H=8mm, S=3.3mm, A=76.5mm, M=12mm, B=30.2mm, N=10mm, D=47mm, F=20mm.

In particular, the distance between the two radiating elements, S, and the distance of the feeding point from the edge, D, represent the most effective design parameters for antenna tuning. Also, the sum of the arm lengths, L1 and L2, must be retained greater than 20cm. The width and the height of the radiating element have been set at 13mm and 8mm, respectively, as in [20]. As for the PIFAs in [18]-[69], the L-shape PIFA can be made out of a cut and bent single metal sheet. A prototype was realized with a

0.4mm thick adhesive copper tape, cut and folded around a polystyrene block to obtain the final 3D structure. Results in terms of simulated and measured reflection coefficient are shown in Figure 2.14, and they exhibit a satisfactory agreement.

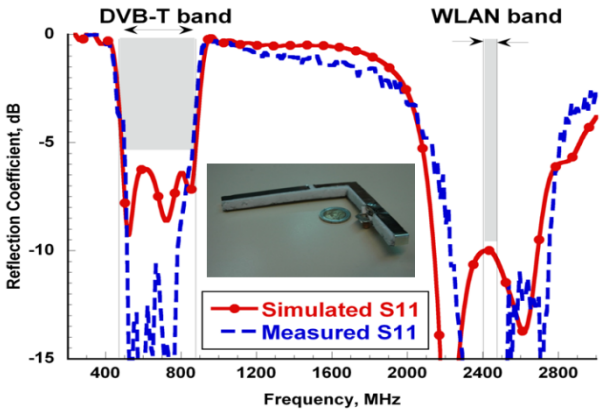

Figure 2.14 - Simulated and measured reflection coefficient for the proposed dual-band L-shape PIFA.

The reflection coefficient is below -6dB and -10dB in the DVB-T and WLAN bands, respectively. The antenna gain is between 1.8 dBi and 2.2 dBi in the DVB-T band, and between 6.2 dBi and 6.4 dBi in the WLAN band; a radiation efficiency greater than 95% has been obtained at both frequency bands due to the absence of lossy substrates.

The radiation pattern modifications have been analyzed when compared to those of the linear-shape PIFA in [20]. The radiation patterns in the principal planes, XZ, YZ and XY, are shown in Figure 2.15 (E_θ and E_φ components, with all of them normalized to the electric field amplitude at $\theta=0$), when evaluated at the center frequency of the bands of interest.

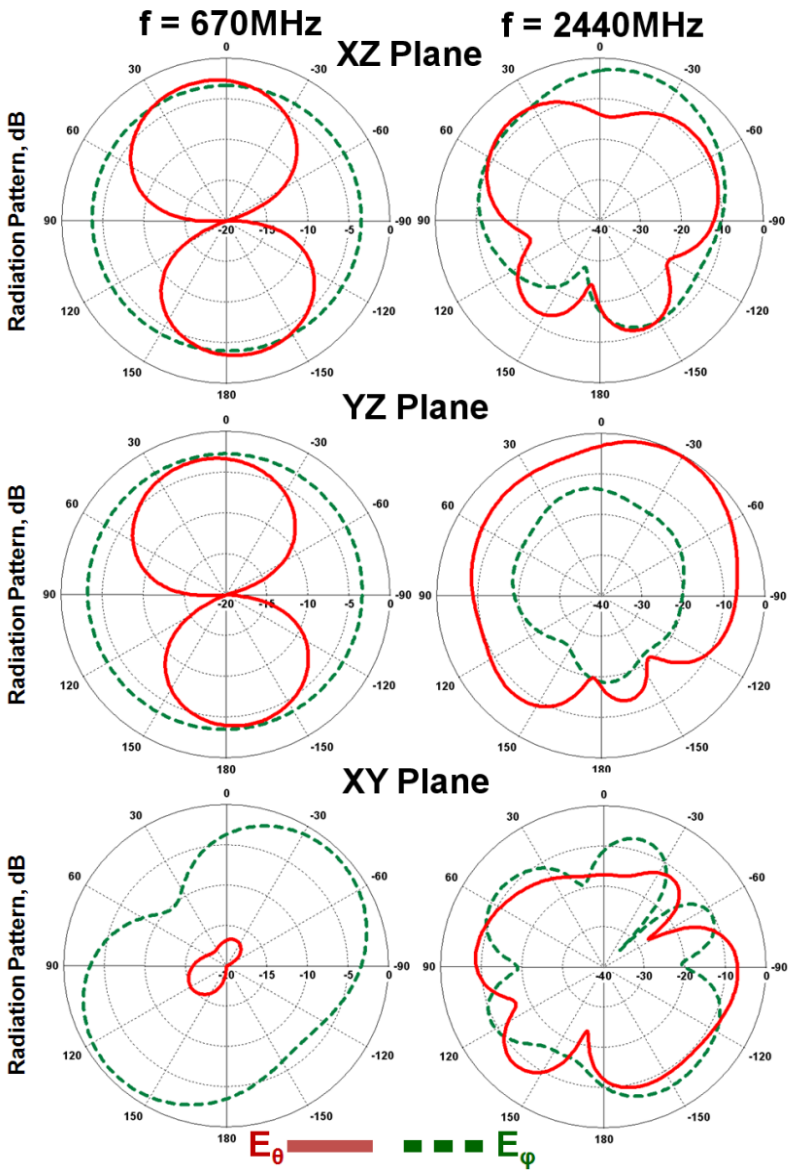

Figure 2.15 - Simulated radiation patterns (Eθ and Eφ components normalized to the electric field amplitude at θ=0) for the proposed dual-band L-shape PIFA: a) 670 MHz (central frequency for the DVB-T band); b) 2440 MHz (central frequency for the IEEE 802.11b,g ban

In the DVB-T band, the L-shape geometry causes a 45° rotation of the radiation pattern in the XY plane, as also apparent from the antenna gain 3D plot shown in Figure 2.16.

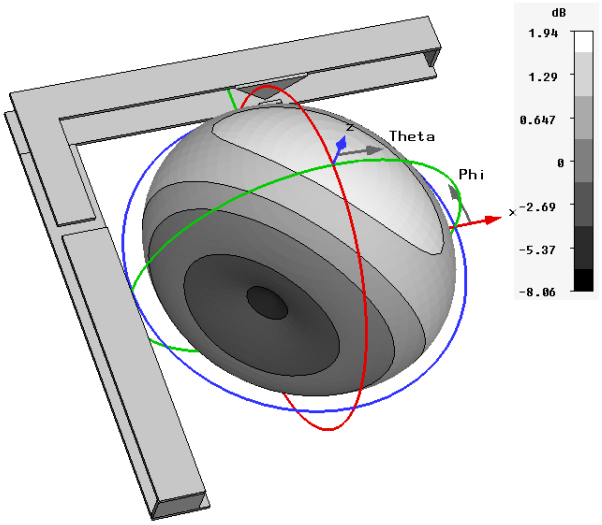

Figure 2.16 - Simulated 3D antenna gain (dBi) for the dual-band L-shape PIFA: 670 MHz.

In the other two principal planes (XZ and YZ) a 10° displacement from broadside of the E_θ component maximum occurs; the E_φ component exhibits an almost omnidirectional radiation pattern. The radiation patterns in Figure 2.17 show that L-shape PIFA radiates a linearly polarized field in the φ=+45° plane. Above results show that the L-shape PIFA radiates as a combination of two orthogonal linear radiators that are fed in-phase. At higher frequency, in the WLAN band, a larger number of lobes are present, as expected since the antenna is electrically long at 2.4 GHz (see Figure 2.15).

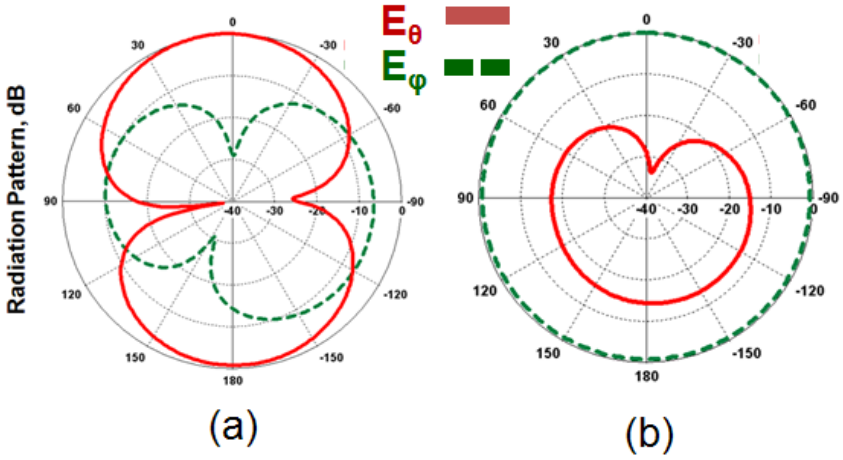

Figure 2.17 - Simulated radiation patterns (Eθ and Eφ components normalized to the electric field amplitude at θ=0) for the proposed dual-band L-shape PIFA at 670 MHz: a) φ=45° plane; φ=-45° plane.

2.3.3 Conclusions

A dual-band L-shape Planar Inverted-F Antenna operating in both the DVB-T band (470-862 MHz) and the WLAN IEEE 802.11b,g band (2400 – 2484 MHz) has been presented. It has been designed to meet space requirements typically required for integration along the corner of display-equipped devices. A prototype was realized and characterized. The L- shape PIFA can be obtained by properly cutting and folding a single metal sheet, so resulting in a relatively low-cost and mechanically robust antenna configuration.

Although the final design here shown has been obtained by assuming specific requirements on the maximum length of the two arms of the L-shape PIFA (less than 15cm for both arms), it has been numerically and experimentally verified that VSWR performance at the extremely large DVB-T frequency band can be still met by properly tuning antenna geometrical parameters, when the arm length requirements change less

than 10% with respect to the lengths in Figure 2.13. This confirms the robustness of the proposed L-shape PIFA design, which can be well optimized also when specific and demanding aesthetic/mechanical requirements must be met.

Chapter III

3 WIDEBAND SPIRAL ANTENNAS

3.1 Introduction

There is a need for wide bandwidth antennas to serve several functions including navigation, broadcasting and personal communication, to mention a few. Using different antennas to cover all communication bands is a simple approach, but leads to increased costs, weight, more surface area for installation and electromagnetic compatibility issues. The adoption of a single, small size wideband antenna is certainly more attractive.

Spirals are widely used circularly-polarized wideband antennas [70]-[73]. Because of the spiral's wideband features, much attention has been focused in recent literature, especially for miniaturization [74]. The basic idea for miniaturization is to slow down the wave travelling within the antenna structure. To do so, several approaches have been pursued, including dielectric [75] or magneto-dielectric loading [76], artificial materials [77], spiral arm shaping [70], [78], and distributed reactive loading [79]. However, when using the popular dielectric loading approach, the input impedance is also lowered. Also, material loading increases the antenna volume and weight. Alternatively, when the wave velocity is reduced via meandering of its metalized arms, the axial ratio deteriorates [70]. It has been found that coiling of the spiral arms provides for impedance control [71]. However, this type of volumetric design/miniaturization is cumbersome.

3.2 Numerical Analysis of a Wideband Thick Archimedean Spiral Antenna

3.2.1 Introduction

As an alternative to volumetric coiling, this chapter presents a spiral whose arms are constructed of simpler vertically oriented metallic strips. Importantly, our numerical data shows significant impedance control with this simple geometry. Concurrently this approach affords all the miniaturizations considered in the past.

The chapter is organized as follows. The paragraph 3.2.2 describes the geometry of the proposed thick Archimedean Spiral Antenna (hereafter denoted as Thick-ASA), and how the strip parameters affect input impedance. In the same paragraph, the Thick-ASA performance (impedance, realized gain and axial ratio) are compared to a conventional Archimedean spiral. In the paragraph 3.2.3, numerical results are presented demonstrating that the dielectric loading is quite effective for miniaturization when applied to the Thick-ASA. Numerical simulations were performed using the commercial software CST MWS®.

3.2.2 Antenna Design

The proposed two-arm Archimedean spiral antenna is shown in Figure 3.1a. Each arm is made of a thin metallic strip of width *w*. In contrast to conventional spirals, each metallic strip is vertically oriented with respect to the antenna's aperture.

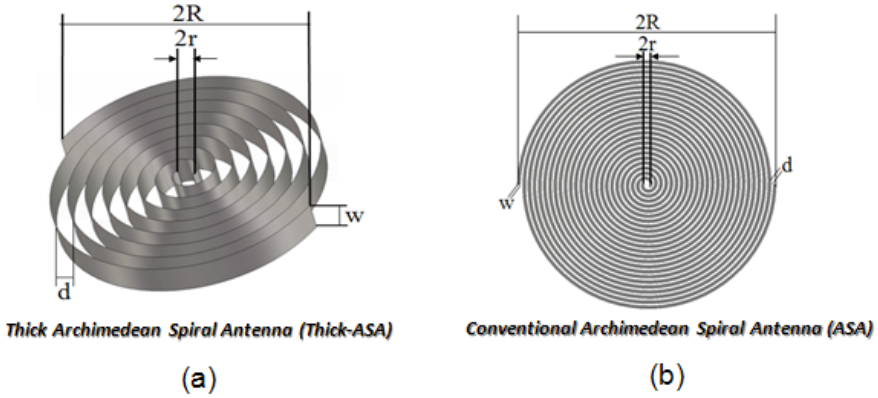

Figure 3.1 - (a) Two-arm Thick Archimedean Spiral Antenna (Thick-ASA): a key aspect of this spiral is the use of vertical strips rather than planar to form the spiral. (b) Conventional Archimedean Spiral Antenna made of two planar strip arms (ASA).

Spiral antennas are usually mounted above a reflector or an absorber-loaded cavity, to achieve unidirectional radiation at broadside. However, as the goal of the work is to demonstrate the advantages of using arms made of vertical strips, we only focus on the free-standing version of the Thick-ASA. Specifically, we compare the performance of spirals whose arms are constructed of planar or vertical strips. For reference, a planar spiral operating over 2-18GHz was chosen [80]. For both the Thick-ASA and the reference ASA, the inner and outer radius were set to r=0.6mm and R=30mm, respectively, and the strip thickness was set to 0.2mm. Both spirals are fed at the centre

through a balanced feed. The distance between the spiral turns and the number of turns will be denoted by *d* and *N*, respectively, and will be adjusted to achieve impedance and frequency control. We note that an advantage of the Thick-ASA is that the parallel strips of the Thick-ASA provide for more capacitance per unit length between adjacent strips. This is demonstrated in Figure 3.2 and implies better control on the input impedance.

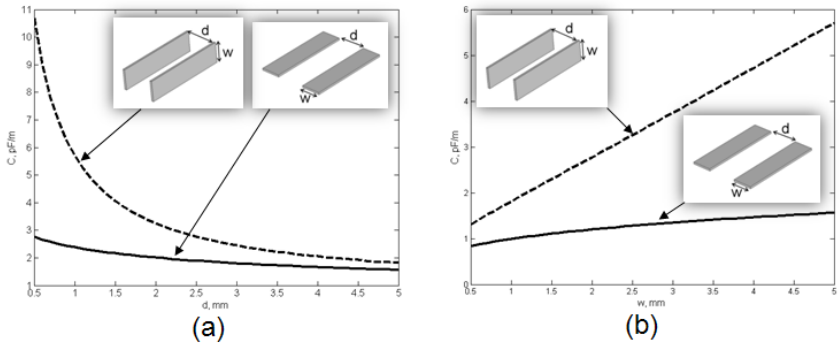

Figure 3.2 - Capacitance per unit length for two side-to-side parallel metallic strips and two face-to-face parallel metallic strips when: (a) w=5mm and d is varied; (b) d=1mm and w is varied.

Specifically, Figure 3.3 shows that the Thick-ASA with *N*=12 turns and *d*=1.22mm has a fairly constant input impedance. We also observe that the Thick-ASA input resistance decreases when the strip width increases.

This is to be expected as the input resistance is proportional to $1/\sqrt{C}$, where C is the capacitance per unit length between the two parallel conductors [81]. When compared to the input resistance of the ASA (*N*=12 turns, *d*=0.6mm and *w*=0.6mm) it is apparent that the Thick-ASA input resistance is stable over a much larger frequency range. More importantly, the impedance of the Thick-ASA is easier to match at lower frequencies. We also note that the input reactance is nearly zero for both antennas, as is typical for spirals.

An apparent advantage of the Thick-ASA is that the number of turns can be increased without enlarging the antenna aperture. Figure 3.4 shows the input impedance of a Thick-ASA for N=12 (d=1.22mm), N=18 (d=0.8mm), and N=24 (d=0.6mm), with the strip width kept to w=2mm. Concurrently, d is varied to preserve the antenna's size, and is responsible for the input resistance variations. Generally, the proposed Thick-ASA allows for a more effective and easier control of its input impedance as compared to conventional spirals.

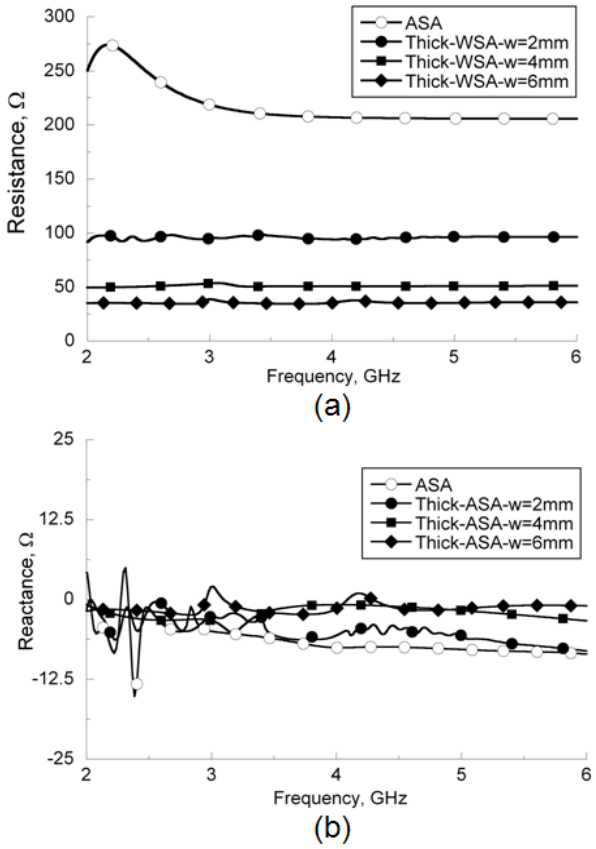

Figure 3.3 - Input resistance (a) and reactance (b) of the free-standing Thick-ASA as a function of antenna thickness w, when d=1.22mm. The reference curve refers to an ASA made of metallic strips with w=d=0.6mm. N=12 for both antennas

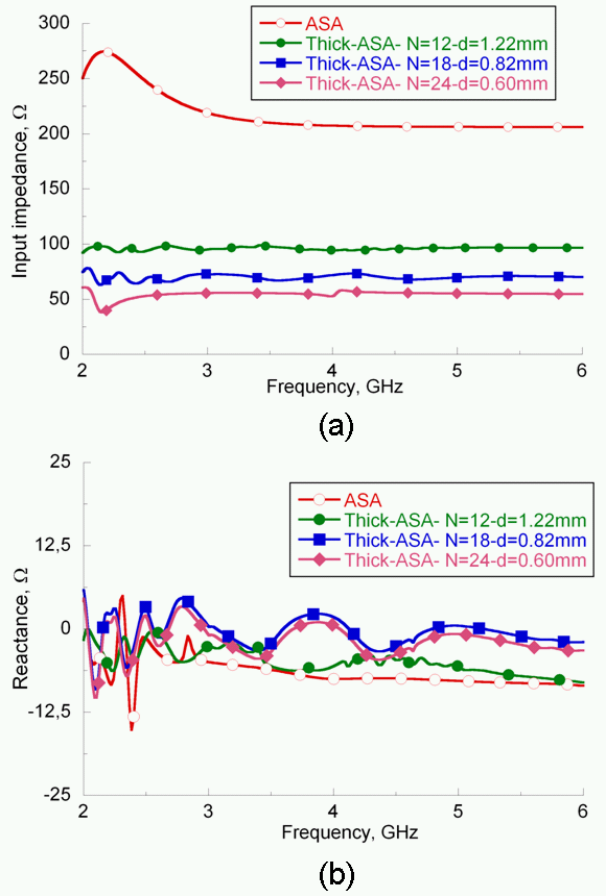

Figure 3.4- Input resistance (a) and reactance (b) of the free-standing Thick-ASA as a function of the turn number, N. The antenna thickness was kept at w=2mm. For comparison, the ASA (w=d=0.6mm, N=12) input impedance is also displayed.

From Figure 3.5, it is apparent that the Thick-ASA has improved gain and axial ratio at lower frequencies without enlarging the antenna's physical aperture (outer radius is kept to R=30mm). Specifically, the Thick-ASA exhibits a 3.6dB gain at approximately 1.7GHz, whereas the standard ASA (N=12 turns, d=w=0.6mm) has the above gain at 2GHz. This implies a slight miniaturization (about 15%). Increasing further the number

of spiral turns, the gain improves at lower frequencies. However, as depicted in Figure 3.4, the antenna impedance also decreases with the number of turns.

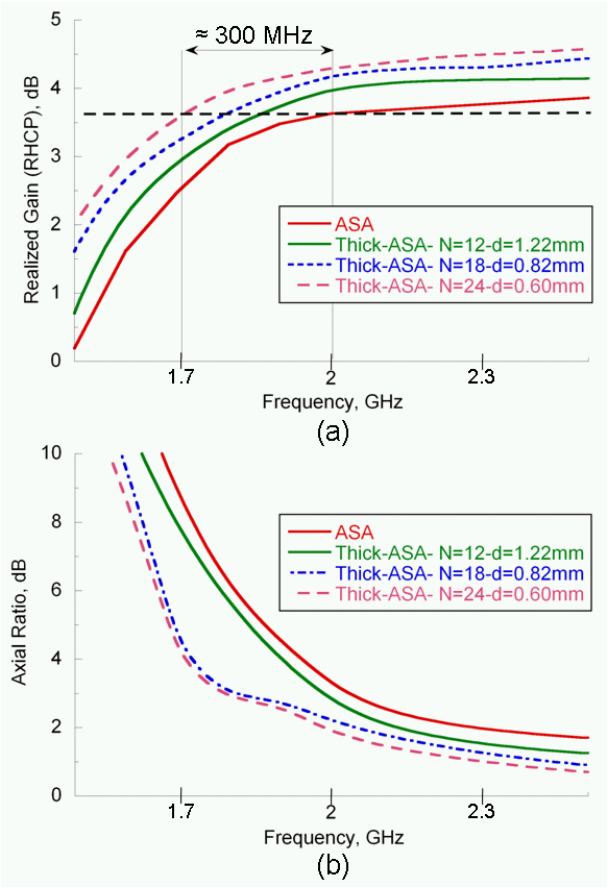

Figure 3.5 - Realized broadside gain and (b) axial ratio of the free-standing Thick-ASA as a function of the spiral turns, N. The antenna thickness was set to w=2mm. Also, the realized gain and axial ratio of the reference ASA is shown (w=d=0.6mm, N=12).

Figure 3.6 shows the realized gain of the Thick-ASA when its thickness *w* is varied. We observe that at lower frequencies the antenna gain improves when the spiral

thickness increases. However, based on Figure 3.3, the input impedance also decreases. Thus, a value of w=4mm was selected as a compromise.

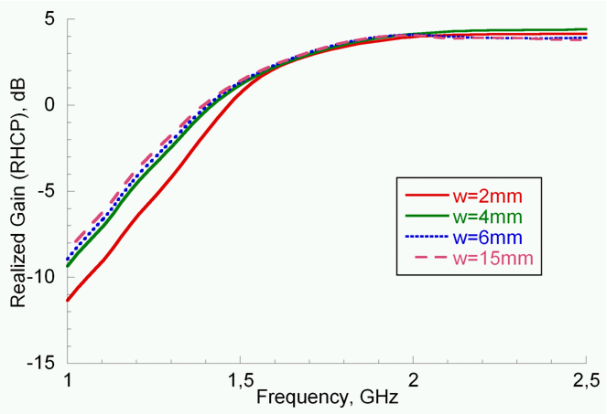

Figure 3.6 - Realized broadside gain of the free-standing Thick-ASA as a function of antenna thickness w (d=1.22mm, N=12).

3.2.3 Dielectric Loading Miniaturization

To examine the impact of dielectric loading on miniaturization, both the Thick-ASA and ASA antennas were embedded in a dielectric material block. That is, the Thick-ASA and standard ASA were simulated while embedded in a thick cylindrical slab of Polytetrafluoroethylene (PTFE). The PTFE slab was of diameter D=65mm and thickness H, and is depicted in Figure 3.7. It is fairly straightforward to realize the thick spiral design in practice. As an example, when a polymer substrate (like a PDMS, polydimethylsiloxane polymer) [82] is used, the metalized portions of the antenna are first fabricated in full including the feed. Subsequently, the polymer is poured onto the metal structure in wet form, and allowed to dry in 24 hours. Multiple polymer layers can be poured to form various combinations of the substrates and superstrates. In the case

when the available substrate is already hardened, thin grooves can be drilled or etched deep into the substrate layer. The spiral's vertical strips can then be inserted into the groove to form the metalized design.

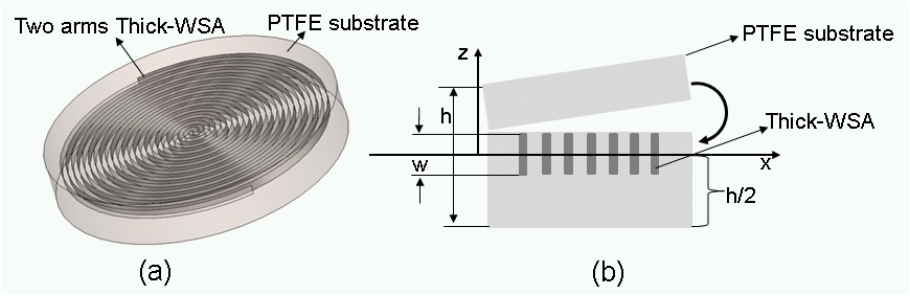

Figure 3.7 - Thick-ASA embedded in a PTFE-slab of thickness H: a) perspective view; b) cross-section of the Thick-ASA-PTFE.

In Figure 3.8 the effect of the PTFE height on the Thick-ASA gain is shown. Due to dielectric loading, the lower frequency limit decreases, and this was expected.

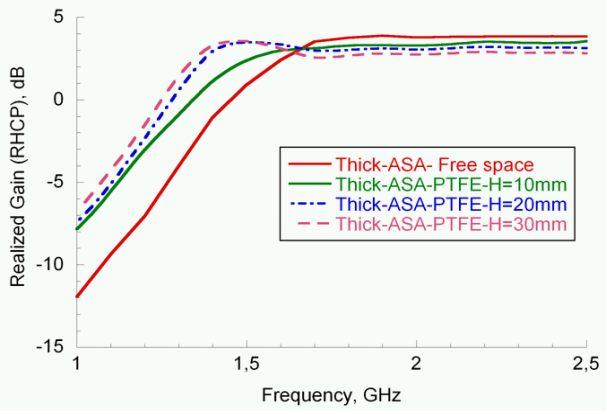

Figure 3.8 - Realized broadside gain for the Thick-ASA, with and without dielectric loading (for various dielectric thickness values of the former case). The strip thickness was set to w=4mm, d=1.22mm and N=12.

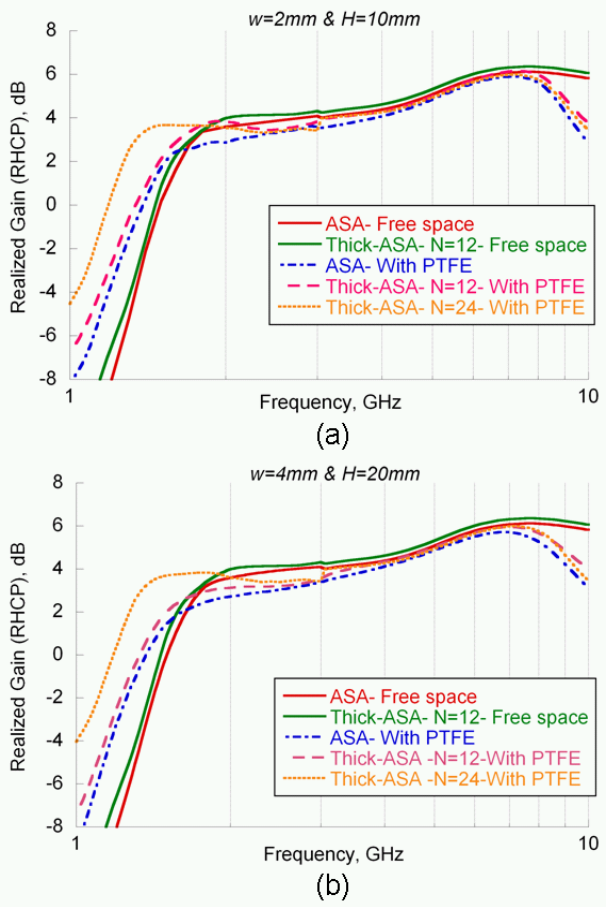

Figure 3.9 - Realized broadside gain for the Thick-ASA when (a) w=2mm, H=10mm; (b) w=4mm, H=20mm (d=1.22mm if N=12, d=0.6mm if N=24). A comparison with the conventional ASA is also provided (w=d=0.6mm, N=12, H=10mm for case (a) and H=20mm for case (b)).

For an antenna thickness (or strip width) w=4mm and dielectric height $H \geq 20$mm, we observe very small variations in terms of antenna gain. Therefore, it is assumed that a reasonable value for the $H/w=5$. For an assumed ratio $H/w= 5$, Figure 3.9 shows the realized broadside gain when the strip width is set to 2mm and 4mm. Specifically, we observe that the Thick-ASA exhibits a gain of about 3.4dB at 1.4GHz. By comparison this gain value is achieved at 1.9GHz for the standard ASA. Nevertheless, axial ratio of

both spirals is comparable, as depicted in Figure 3.10. However, without employing variable spiral growth rates, the spiral gain drops at higher frequencies. This is to be expected and was already noted in [70] and [74].

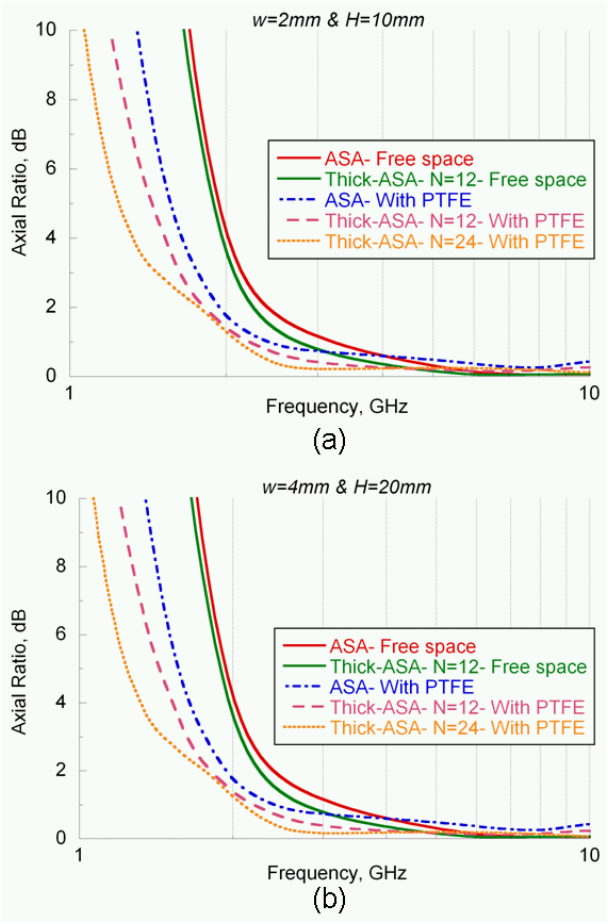

Figure 3.10 - Axial ratio of the Thick and conventional ASA when (a) w=2mm, H=10mm; (b) w=4mm, H=20mm (d=1.22mm if N=12, d=0.6mm if N=24). For the conventional ASA, w=d=0.6mm and N=12.

3.2.4 Conclusions

Some advantages of the two-arm Archimedean spiral, whose arms are vertically oriented with respect to the antenna's aperture, were examined through a numerical analysis. , It was noted that using vertical strips to form the spiral arms leads to a larger number-of-turns within the same aperture size. Concurrently, this approach allows for a more effective and easier control of the spiral's input resistance as compared to conventional spirals (that use planar strips to form the arms). Further, we found that dielectric loading leads to additional miniaturization as compared to conventional spirals. Although the presented results are specific to Archimedean spiral antennas, the same approach can be applied to other antennas made of wires or printed strips, i.e. log-spirals and helical antennas. We should also remark that non-uniform dielectric loadings applied close to the antenna's surface (as suggested in [74]) can be incorporated by simply varying the strip width. To the best of our knowledge, this work is the first to propose *wideband* spiral antennas formed of thick-arms. The only relevant paper to this work is [83]. However, [83] refers to a *resonant* thick-arm spiral for an ingestible capsule (only 21% bandwidth around 500MHz). This arithmetic spiral was made of a single arm having a length equal to about a quarter of a wavelength. Further, in [83], the authors state that thick-arms were used to increase impedance bandwidth, a statement in agreement with the known practice of using thicker wires to increase the dipole's bandwidth.

Chapter IV

4 Integration of Slot Antennas in Commercial Photovoltaic Panels for Stand-Alone Communication Systems

4.1 Introduction

Autonomous communication systems often use photovoltaic (PV) panels that are physically separated from the antenna, and this demands for a compromise in the utilization of the available space. Moreover, in several applications, as for example monitoring, vehicular communication and satellite systems, distinct PV panel and antenna may be anti-aesthetic, expensive and causes engineering issues. For above reasons, antenna integration in large PV panels is desirable and it has become a research topic. Designing the antennas such that they can be easily integrated in a commercial PV panel without modifying the panel geometry (after-market integration) can result in a low-cost implementation of additional functions in a solar PV field. For example, a low-data rate wireless communication system could be implemented for the remote control and monitoring of PV panels in large solar fields. In this context, low cost antennas with proper polarization and pattern characteristics are needed to improve panel-to-panel radio links or maximize a tunnel-propagation effect (Figure 4.1). Most recent solutions for antennas integrated in PV panels are those based on the innovative transparent antennas [84]-[86], or patch [87]-[94] and slot [94]-[96] antennas.

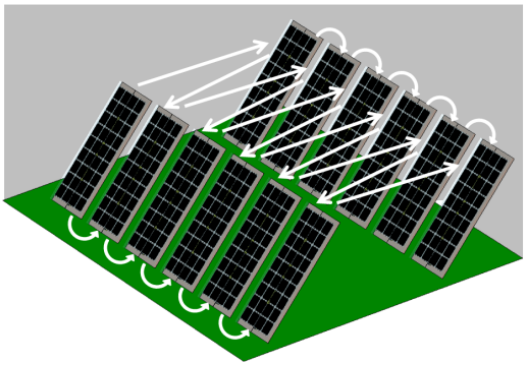

Figure 4.1 - A simplified scheme of a solar PV field where a wireless communication link can be used for remote control and monitoring functions.

Transparent materials have been proposed to implement innovative transparent antennas, as they can be easily mounted on solar cells. Transparent antennas have been optimized for different applications, at 3.4-3.8GHz [84] and 2.5GHz [85] frequency bands. Nevertheless these materials are still relatively expensive. Besides, meshed patch antennas printed on the top of PV cells are considered a cost-friendly solution. An example of such antennas, optimized for a 2.52GHz small satellite application, is described in [86]. However, a 90% sunlight transparency needed for the proper functioning of the solar cell [86] cannot be easily achieved.

Solar cells have been employed themselves as a radiating patch [87] or as a coupled patch [88]-[90], for GPS vehicular applications, GSM bands or 3.76 GHz satellite communications. In such cases the cell dimensions are strictly related to the operating frequency, and this limits the possible applications for PV panels made of cells with standardized cells. Solar cells may also be used as a ground plane for an upper patch element [91]-[93], but with a reduction of the PV solar efficiency.

Slot antennas placed between solar cells have been optimized for high frequency applications [94]-[95], or by requiring modifications of the DC bus wires [96]. Alternatively, slots have been realized by properly etching of them [97] into the solar cell, but reducing the cell solar efficiency.

In this chapter, two configurations of low-cost slot antennas suitable for their integration in a class of commercial large PV panels are described. As test cases, two antennas operating at the GSM/UMTS and WIMAX frequency bands have been designed to show the achievable performance in terms of compactness and percentage impedance bandwidth (paragraph 4.2). A considerable reduction of the antenna physical size was obtained exploiting the presence of the cover glass layer that is always present in commercial PV panels. In the paragraph 4.3, measurements on antenna prototypes attached to real PV panels have been used for a fine tuning of the antennas, so avoiding detailed numerical models that would result in complex models but not able to account for the several propagation phenomena involved in the periodic/multilayer structure of a PV panel. Indeed, the effects on antenna performance of the cells close to the slot, as well as of the DC bus wires and panel aluminium frame cannot effectively accounted for by numerical models (dielectric permittivity values of the PV cell material at the UHF and microwave frequencies are also difficult to find).

4.2 Slot Antenna Design

The antenna integration concept here proposed is based on the exploitation of the room available between adjacent solar cells of some large PV panels, so without decreasing the panel solar efficiency. In particular, two cell arrangements often used in large PV panels are considered, and they are shown in Figure 4.2.

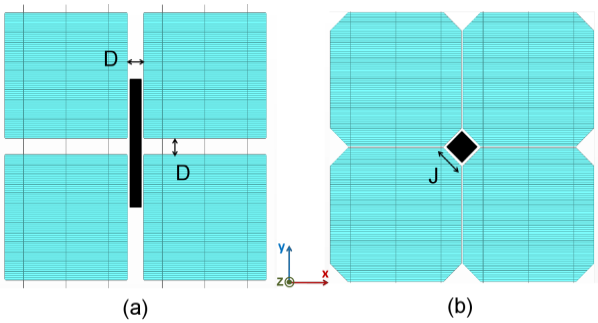

Figure 4.2 - Two typical arrangements for PV cells in large panels: (a) square cells separated by a distance D; (b) octagonal cells close to each other, with an uncovered square-shape space whose side length is denoted by J. Possible locations for slot antennas are also shown (with dark color), which are such that the slot aperture is not crossed by the DC voltage bus wires.

For such configurations, a linear or square slot antenna etched on a low-cost substrate can be attached just on the back side of the panel and located in such a way that the slot aperture is not obstructed by the cells (which basically behave like shielding conductive surfaces). Also, the DC voltage bus wires have not to cross the slot aperture, as it would result in an antenna shorting effect. For example, this means that in the cell arrangement shown in Figure 4.2a, gaps parallel to the x-axis are not functional because of the presence of the DC voltage bus wires; on the other hand, more room is available along the y-axis (it being only limited by the panel frame size), so allowing either the allocation of some long linear slots (resonating at low frequencies) or the allocation of linear arrays made of shorter linear slots (higher resonance frequencies) to implement

high-directivity arrays or a number of low-directivity arrays operating at different frequency bands (electronic beam scanning can also be implemented through a proper feeding network).

To better understand how to make use of the above linear or square gaps, the stack-up of two typical PV panels are shown in Figure 4.3. Silicon or GaAs (Gallium Arsenide) solar cells are usually incorporated between two ethylene vinyl acetate (EVA) layers. Also, two cover glass layers are placed at the top and bottom sides of the PV panel. In some commercial panels, the bottom cover glass layer can be replaced by a plastic backsheet, as a Tedlar® film (Figure 4.3b).

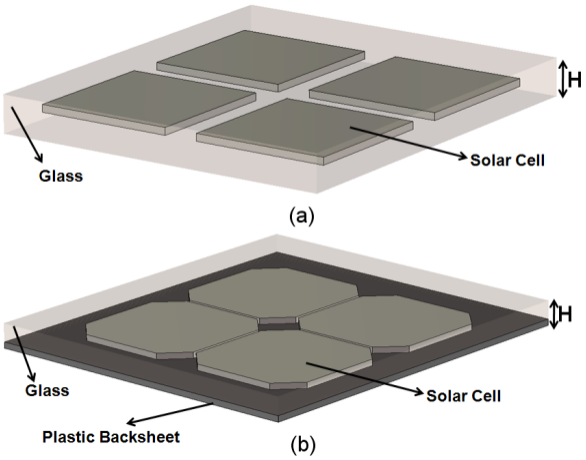

Figure 4.3 - Stack-up of two typical commercial photovoltaic panels: (a) a glass- cells-glass PV panel, with square solar cells and (b) a glass-cells-Tedlar® PV panel with octagonal solar cells. In both PV panel configurations, the solar cells matrices are encapsulated between two EVA layers.

Therefore, a slot antenna positioned according to the two above mentioned criteria, could be enclosed by cover glass and EVA layers. Both layers are low-loss dielectrics and their effect can be accounted for during the design process. EVA layer is relatively thin (usually less than 0.1mm) and its effect can be neglected up to some Gigahertz. The glass layer is thicker, going from a few mm up to 10 mm when both a top and a bottom cover glass layer are present (see Figure 4.3a). Notably, the glass layer of the PV panel

that will appear to be positioned on the top of the slot helps in reducing slot resonance frequency [98], so giving rise to an extremely advantageous antenna miniaturization effect (without requiring any antenna meandering or distributed reactive loading, or any other complex configuration).

As test cases for the proposed design approach, a linear slot antenna and a square slot antenna have been designed and prototyped, to fit in commercial PV panel topologies like those in Figure 4.3a and Figure 4.3b, respectively. Figure 4.4 shows the top view of the two proposed antennas: a three-stepped slot antenna (*TSSA*) [99] and a square slot antenna (*SSA*) [100]. Both slots are realized on a 1.6mm thick FR4 substrate (ε_r=4.4, tgδ=0.02); a CPW and a microstrip are used to feed the TSSA and SSA, respectively (both with a 50-Ω characteristic impedance).

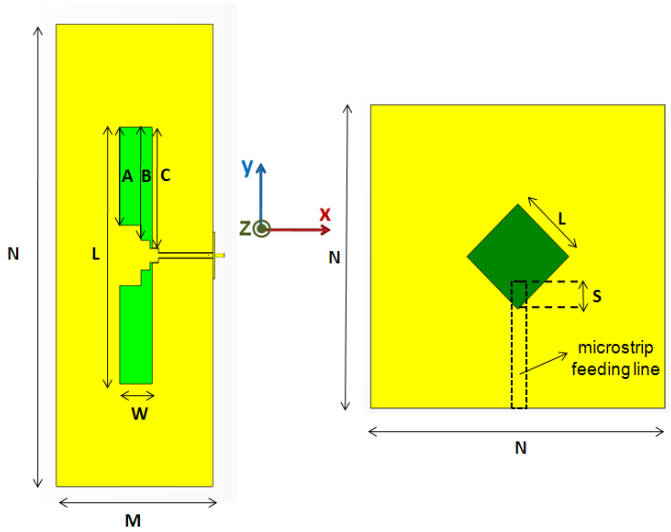

Figure 4.4 - Layout of the proposed slot antennas suitable to be integrated in a typical PV panel: (a) three-stepped slot antenna, *TSSA*; (b) square slot antenna, *SSA*.

The three-stepped slot configuration has been chosen to check the best performance that can be achieved in term of percentage impedance bandwidth, in the framework of slot antennas whose maximum width is limited by the presence of nearby PV cells

separated by a given distance D. Specifically, it is shown that the antenna can operate in frequency bands that allocate both GSM (1710 – 1910 MHz) and UMTS (1920 – 2170MHz) applications (around 24% percentage bandwidth). The three-stepped slot is etched on the same side of the CPW feeding line. The main parameters related to the resonant frequency and to the bandwidth of *TSSA* are the slot length (*L*) and width (*W*), respectively. An antenna impedance fine tuning on a wide frequency bandwidth can be achieved by varying the lengths *A*, *B* and *C*.

In the *SSA*, the microstrip feeding line is in the opposite side with respect to the square slot. As in other square slot configurations, the length of the open-circuit stub (*S*) behind the slot is optimized for input impedance tuning. The S*SA* has been designed to operate at higher frequencies, in the WIMAX 3300–3800MHz frequency band, as it represents the lower frequency band that can be covered when the side of the square space available at the corner of octagonal cells is less than 30mm (and a cover glass layer of less than 5mm is considered).

The numerical simulations were performed using the commercial software CST MWS®. Simulation results on the miniaturization effect due to the PV panel cover glass layer are discussed in the paragraph 4.2.1. The effects of the solar PV cells close to the antenna have been numerically checked by adding square or octagonal metallic patches positioned nearby the slots, between the slot plane and the glass layer (paragraph 4.2.2). Finally, the influence of a reflector behind the whole structure (needed if an unidirectional beam is required) is analyzed in the paragraph 4.2.3.

4.2.1 Miniaturization effect due to the cover glass layer

A simplified model of the PV cell multilayer structure has been adopted during the numerical design process (Figure 4.5). Indeed, only a glass layer ($\varepsilon r = 4.82$, $tg\delta = 0.0054$) has been considered.

The TSSA and SSA have been optimized by considering for the cover glass layer a thickness *G* equal to 8mm and 5mm, respectively. These values come from the

corresponding value of the cover glass layer of the two commercial photovoltaic panels that have been used for the measurements. The geometrical parameters of the two optimized slot antennas are listed in Table I.

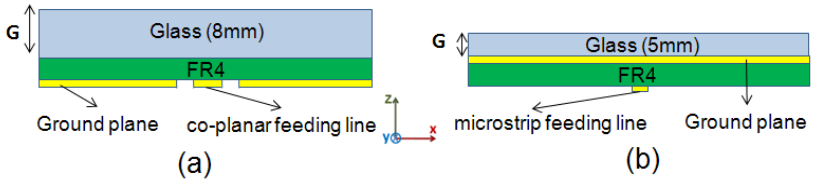

Figure 4.5 - Stack-up of the proposed slot antennas suitable to be integrated in two typical PV panels: (a) *TSSA* and (b) *SSA*. The cover glass layer on the top is the only layer of the PV cell that has been considered in the numerical model used for the slot antenna design.

TABLE I

ANTENNA DIMENSIONS OPTIMIZED WITH COVER GLASS LAYER (MM)

TSSA				SSA	
N	200	A	35.2	L	19.5
M	70	B	40.7	N	140
L	92.4	C	43.5	S	11.4
W	13				

The *TSSA* and *SSA* fit an overall volume of 200×70×1.6 mm^3 and 140×140×1.6 mm^3, respectively. The *TSSA* slot is 92.4mm long (*L*) and 13mm wide (*W*). The square slot exhibits an area of about 19.5 × 19.5 mm^2, with a *S* =12.3mm stub. Figure 4.6 shows the reflection coefficient of the two antennas.

To give evidence to the miniaturization effect, in the same figure the reflection coefficient for an identical slot antenna without the glass layer is shown. It has been numerically estimated that the presence of the cover layer leads to a quite important miniaturization level: 36% for the *TSSA* and 25% for the *SSA*.

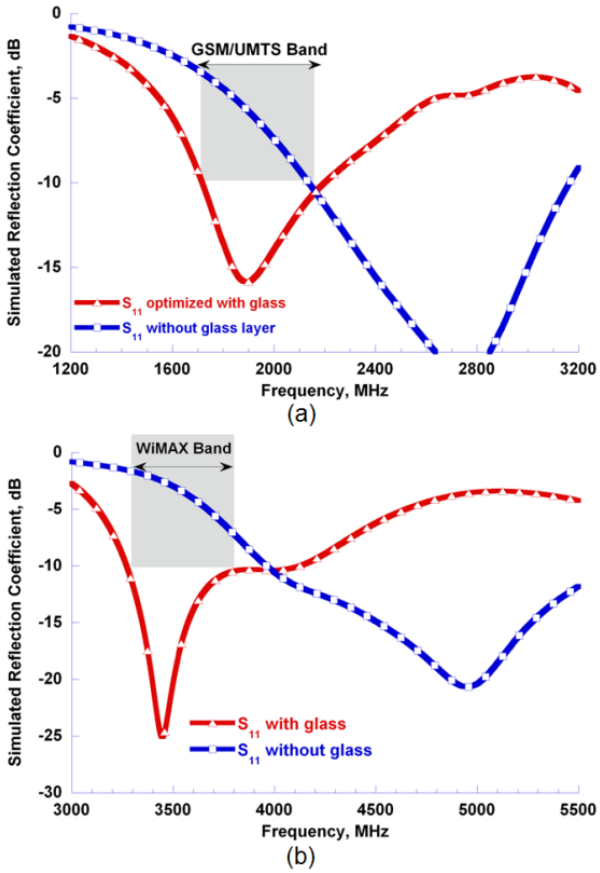

Figure 4.6 - Simulated reflection coefficient for the slot antennas: (a) *TSSA* and (b) *SSA*. A reference curve showing the reflection coefficient when the cover glass layer is removed.

It has been also verified that *TSSA* and *RSA* antenna gain are stable in the frequency band of interest, as shown in Figure 4.7.

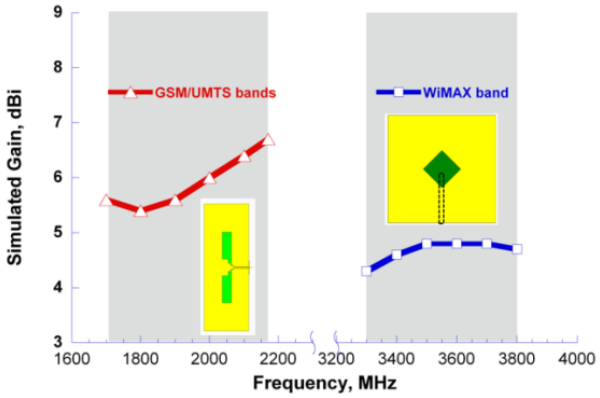

Figure 4.7 - Simulated gain for the proposed TSSA and SSA in the GSM/UMTS and WIMAX bands, respectively.

4.2.2 Numerical analysis of the effect of the PV cells located nearby the slot

The effects of the solar PV cells close to the antenna have been numerically checked by adding square or octagonal metallic patches positioned nearby the slots, in the middle of the glass layers (Figure 4.8). The 1-mm-thick plastic backsheet effect in the PV panel of Figure 4.8b can be neglected in the numerical simulation.

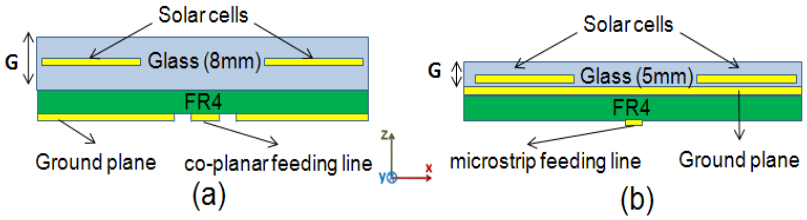

Figure 4.8 - Stack-up of the proposed slot antennas suitable to be integrated in two typical PV panels, for (a) the *TSSA* and (b) the *SSA*. The cover glass layer on the top is the only layer of the PV cell that has been considered in the numerical model used for the slot design, while simple metallic patches have been used to model the PV cells.

Figure 4.9a shows the reflection coefficient behaviour of the TSSA, by varying the distance *D* between the PV cells from 10mm up to 50mm. It is noted that when the distance between two solar cells is smaller than the *TSSA* slot width (*W*=13mm), there is a significant impedance mismatching, as expected since the slot is partially covered by the PV cell.

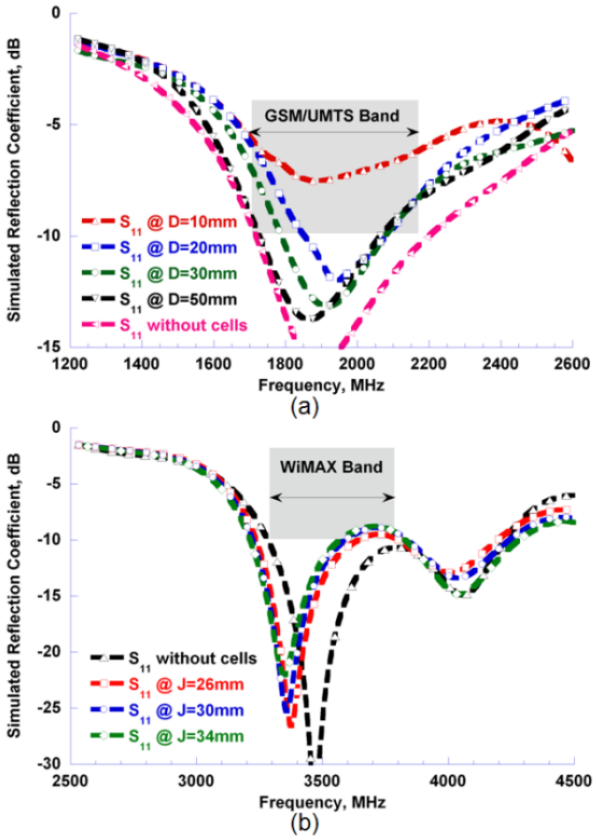

Figure 4.9 - Simulated reflection coefficient for the slot antennas, as a function of the size of the room available between adjacent cells (parameters *D* and *J* in Figure 4.2). PV cells have been modeled trough simple metallic patches: (a) *TSSA* and (b) *SSA*. As a reference, a curve has been added for the simpler cell model where only the glass layer is present.

Numerical results for the SSA are shown in Figure 4.9b. It results that for a slot side of 19.5mm, the distance between nearby octagonal PV cells (Figure 4.2b) should be enough large to allow that the side of the square space in Figure 4.2b, *J*, is at least greater than 26mm. The presence of the solar cells determines a slight mismatching and a 100MHz shift toward lower frequencies (this shift can be compensated through a small reduction of the square slot side, *L*).

4.2.3 A metallic reflector to get an unidirectional radiation pattern: its effect on the antenna input impedance

An aluminium reflector placed at a distance *R* from the bottom side of the FR4 substrate (Figure 4.10) can be used to achieve unidirectional radiation at broadside and increase the antenna gain.

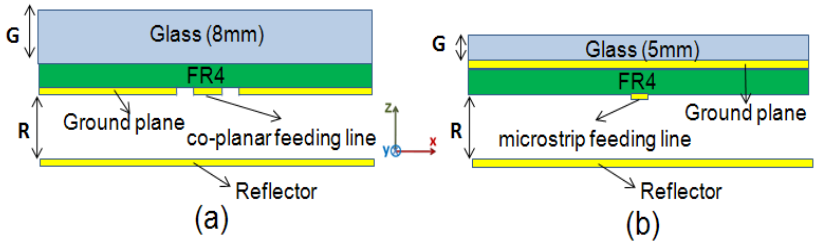

Figure 4.10 - Stack-up of the (a) *TSSA* and (b) *SSA* with a 250mm-side square reflector plane. Its presence ensures a low back radiation and an improvement of the antenna gain.

The effect on the reflection coefficient of a 250mm-side aluminium square reflector is shown in Figure 4.11 for different distances *R*. The presence of the reflector results in slight impedance mismatching that can be compensated by varying the main parameters of the two antenna configurations. For *R*=30mm, antenna gain increases up to about 8dBi and 7dBi for the TSSA and SSA, respectively. The radiation patterns in the principal planes (E_θ and E_φ components), evaluated at the centre frequencies of the

bands of interest, are shown in Figure 4.12. A back lobe amplitude less than -13dB is achieved for both antennas. The two slots antennas (both they are linearly polarized antennas) exhibit a cross-polar component levels below -18dB.

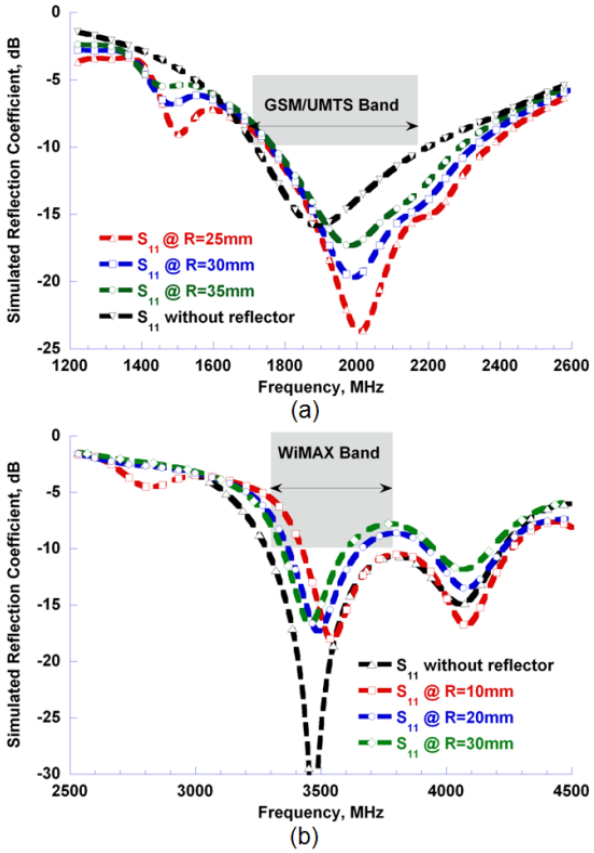

Figure 4.11 - Simulated reflection coefficient of the slot antennas versus the distance R between the FR4 bottom and a metallic reflector: (a) TSSA and (b) SSA. The reference curve shows the antenna reflection coefficient when the reflector is absent.

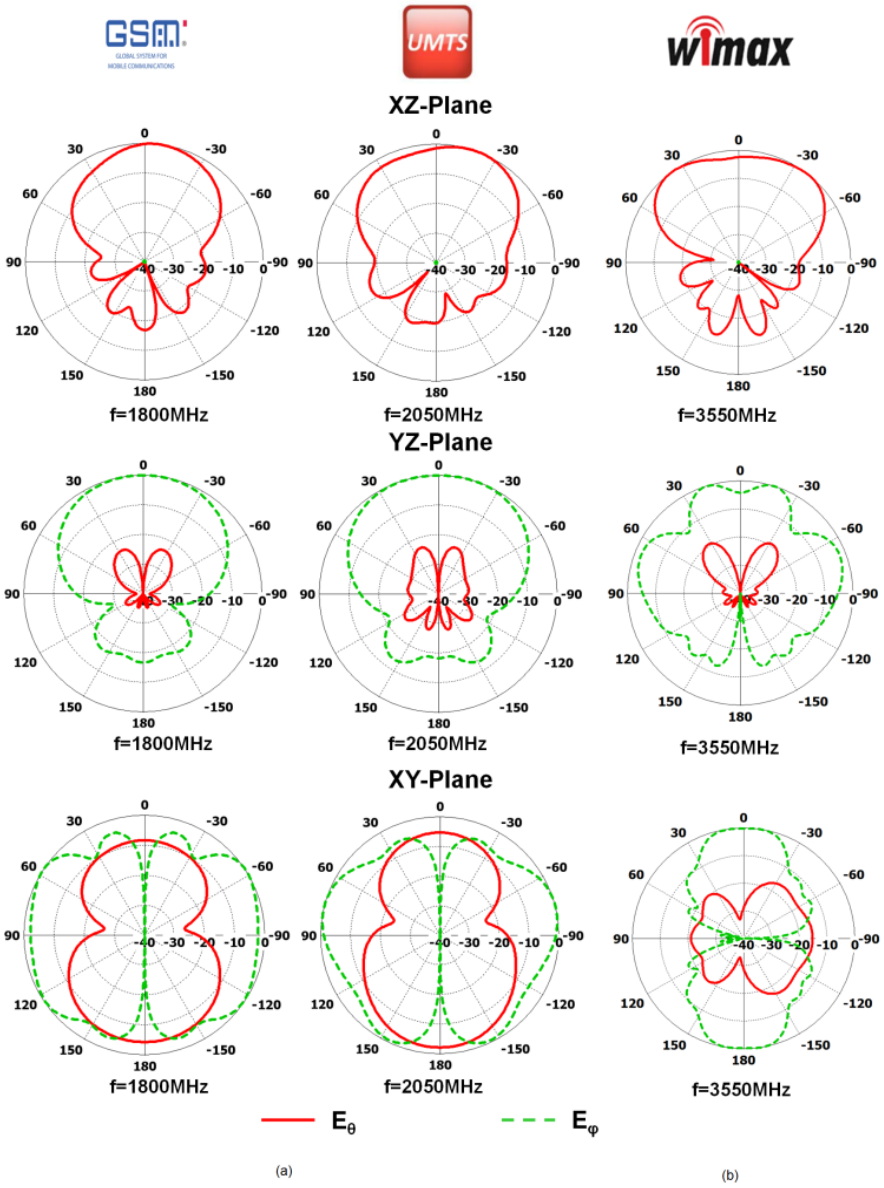

Figure 4.12 - Normalized radiation patterns in the principal planes at GSM and UMTS centre frequencies for the *TSSA,* and at WIMAX centre frequency for the *SSA*. A metallic reflector is placed at a distance *R* from the FR4 bottom: *R*=30mm for the TSSA, and *R*=20mm for the SSA.

4.3 Experimental Results

Figure 4.13 shows the *TSSA* and *SSA* prototypes. Two different commercial PV panels, corresponding to the cell arrangements in Figure 4.2, have been used to estimate antenna performance when it is attached on a real PV panel.

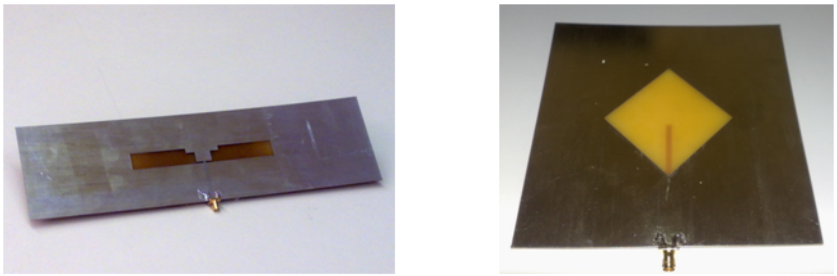

Figure 4.13 - TSSA (a) and SSA (b) prototypes realized on a 1.6mm-thick FR4 substrate.

4.3.1 Measurements results for the TSSA prototype

A 140-W-BRP6336064-140 PV panel [101] was employed to check the TSSA input impedance for different locations of the antenna with respect to the panel surface. The panel (Figure 4.14) consists of 36 high-quality polycrystalline silicon square solar cells (156×156 mm^2); the aluminium panel frame is 1655x991mm^2 and its thickness is 40mm. The total thickness of the top and bottom cover glass layers is 8mm, that guarantees a good light permeability and protects solar cells from atmospheric agents. In the standard BRP6336064-140 panel the distance *D* between the PV cells is set to 25mm. A panel with four columns at different distances (*D*=20, 30 and 50mm) was specifically manufactured, to measure the effect of the cell proximity on the antenna reflection coefficient. The distance between cells along the vertical direction is set to 25mm.

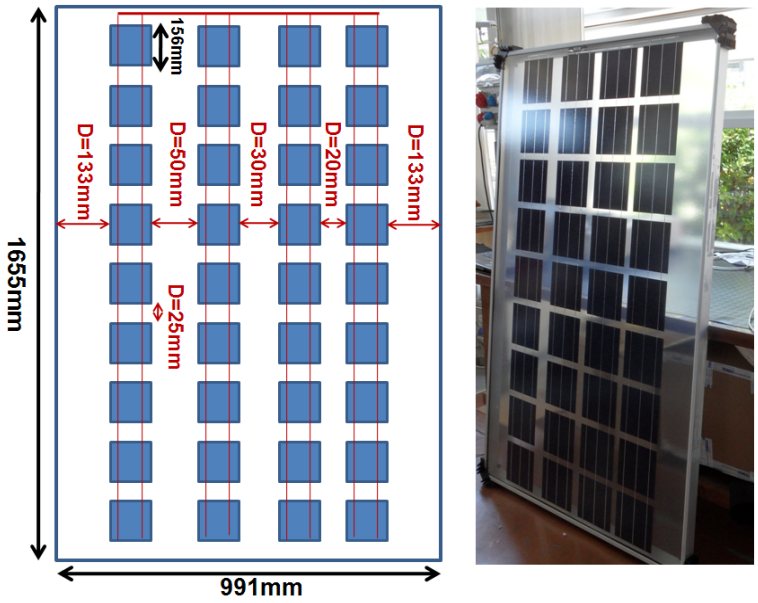

Figure 4.14 - The BRP6336064-140 PV panel used for testing the TSSA. The panel is made of four columns at different distance: *D*=20, 30 and 50mm. The distance between cells along the vertical direction is set to 25mm.

Measured values of *TSSA* reflection coefficient are plotted in Figure 4.15, for the isolated antenna (without the glass layer) and when the antenna is attached on the back of the PV panel, at the 133mm-wide space at the border of the panel (Figure 4.14), in order to maximize the distance from the cells and so minimize their effect. The miniaturization effect of the 8mm-thick glass layer is evident, while the variations introduced by a reflector at a distance *R*=30mm are much smaller. The cover glass layer determines a frequency shift of about 350MHz. Subsequent to the above preliminary measurements, a fine tuning of some geometrical parameters was used to get a return loss greater than 10dB in the whole band of interest, in presence of a reflector at a distance *R*=30mm form the panel bottom.

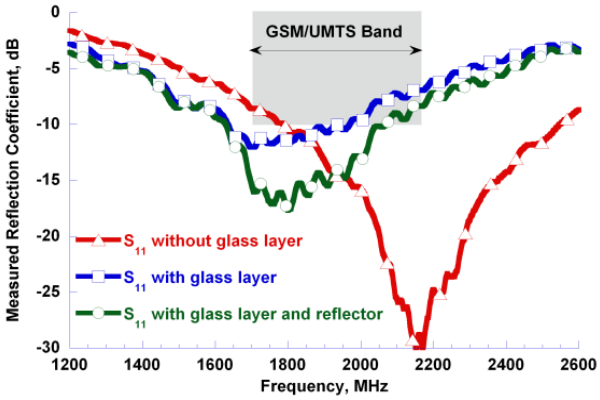

Figure 4.15 - Measured reflection coefficients of the proposed *TSSA,* with and without the cover glass, and in presence of a reflector at a distance of *R*=30mm.

Final geometrical values are shown in Table II.

TABLE II
PV panel integrated prototypes

TSSA DIMENSIONS (MM)			
N	200	A	42.5
M	70	B	49
L	105	C	54.3
W	14.5	R	30

Reflection coefficient measurements are shown in Figure 4.16, when the slot is attached on the back side of the PV panel, in presence of the metallic reflector at a distance of *R*=30mm, and at different distances from the nearby PV cells; indeed, the slot antenna has been measured when positioned at the centre of the room available between the four columns that are separated by a distance *D*=20cm, *D*=30mm and *D*=50mm.

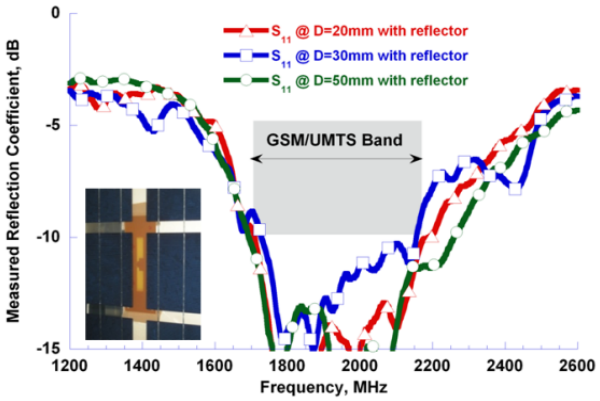

Figure 4.16 - Measured reflection coefficient of the *TSSA* by varying the distance between the slot and the nearby PV cells (the slot is positioned at the center of the room available between adjacent columns of PV cells, Figure 4.14). The metallic reflector is placed at a distance of *R*=30mm from the panel bottom.

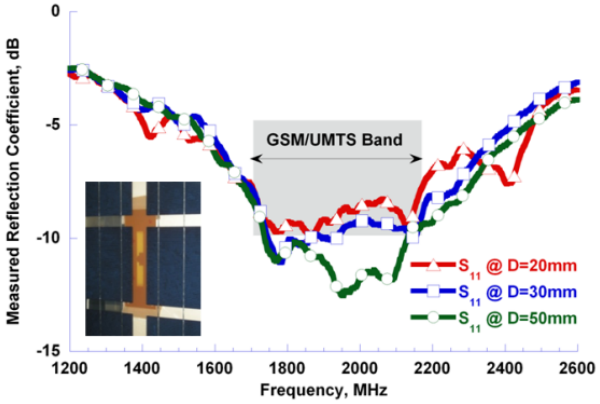

Figure 4.17 - Measured reflection coefficient of the *TSSA* by varying the distance between the slot and the nearby PV cells (the slot is positioned at the center of the room available between adjacent columns of PV cells, Figure 4.14). The metallic reflector has been removed.

If the specific application requires a bidirectional radiation pattern (as that about solar fields and mentioned in the Introduction) the reflector can be removed. The absence of the metallic reflector results in a slight impedance mismatching (Figure

4.17), which can be recovered by varying some of the antenna geometrical parameters, as for example the length *C* (see Figure 4.4). A possible approach to improve impedance tuning without changing slot geometrical parameters consists in moving the slots with respect to the nearby cells, for example by shifting the slot along the direction of its longer axis (y-axis) In Figure 4.18, the reflection coefficient of the antenna placed in three different positions (*A*, *B*, and *C*) is shown, when the distance between two solar cells columns is *D*=20mm, which corresponds to the worst case in terms of impedance detuning (Figure 4.17). In *Position A*, the centres of the slot antenna and solar cells are aligned along the x-direction (Figure 4.18a). Instead, in *Position B* the slot centre point corresponds to the symmetric centre of a group of 4 cells (Figure 4.18b). The *Position C* is an intermediate position between *A* and *B*.

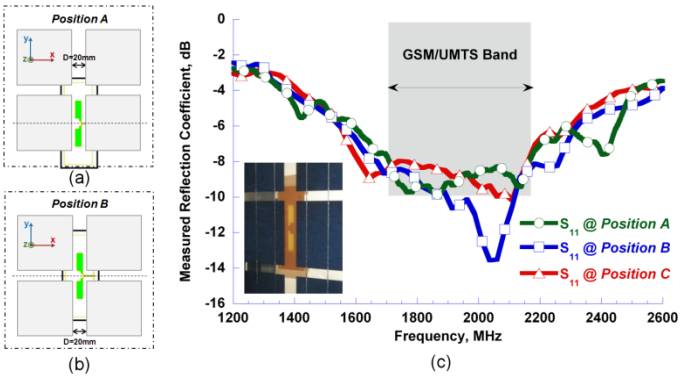

Figure 4.18 - Two Measured reflection coefficient of the *TSSA* by varying the relative position of the slot antenna with respect to the nearby solar cells, along the y-axis. Different positions were considered. The *Position C* is an intermediate position, between *Position A* and *B*.

Measured results in Figure 4.18 show that a small shift with respect to the y-axis represents an effective parameter to match the antenna without changing its geometry. Moreover, this effect must be considered when an arrangement of slots is used to implement a linear array along the y-axis, since the input impedance of each array element will be a function of its relative location with respect to nearby cells.

4.3.2 Measurements results for the SSA prototype

A 180-W-RSP180S-50M PV panel [101] was employed to check the SSA input impedance for different locations of the antenna with respect to the panel surface (Figure 4.19). The 1580x808 mm^2 panel consists of 72 monocrystalline silicon octagonal solar cells (125×125 mm^2); a 25mm-thick aluminium panel frame can be employed to fix the panel on a supporting structure. In the top and bottom side of the solar cell matrix, a 4mm-thick cover glass and a 1mm-thick Tedlar® film are present, respectively. The available space between each 4 octagonal solar cells group is a *J* =30mm-side square.

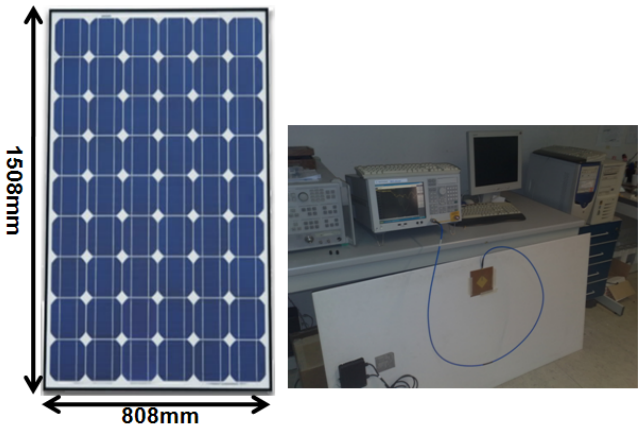

Figure 4.19 - The RSP180S-50M PV panel used for testing the SSA. The *J*-side square space (Figure 4.2b) between cells is 30x30mm^2.

Figure 4.20 shows the measured reflection coefficient of the SSA when it is attached on the PV panel backside, with and without a reflector. An aluminium reflector can be easily fixed to the metallic frame, at a distance of about 20mm from the FR4 bottom side. In the prototyping stage a decreasing of the stub length (*S*) was necessary, by setting this parameter equal to 12.3mm. The measured reflection coefficient (Figure

4.20) of the integrated antenna without the reflector was below -14dB in the band of interest. The presence of a reflector resulted in a slight mismatching and in a frequency shift. Anyway, the antenna reflection coefficient was still below -10dB in the whole WIMAX band.

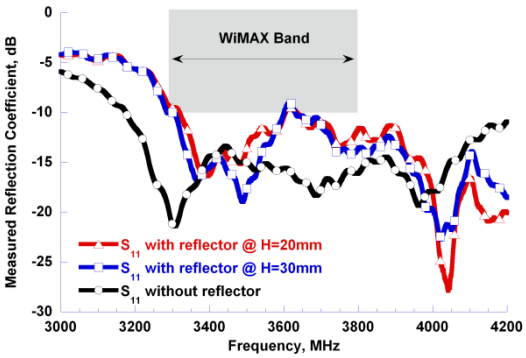

Figure 4.20 - Measured reflection coefficient of the proposed SSA attached to the back side of a PV panel, with and without the reflector (the reflector was at a distance *H*=20mm or *H*=30mm from the FR4 bottom).

4.4 Conclusions

Two slot antenna configurations have been optimized to fit the room between adjacent PV cells of a class of commercial PV panels. A linear slot (three-stepped slot antenna) with width of 13 mm and length of 94.2 mm can achieve a return loss greater than 10dB in a 24% percentage frequency bandwidth, like that required for GSM/UMTS applications. Moreover, a square slot with a side smaller than 20mm can be used to implement an antenna operating in the 3300–3800MHz WIMAX bands. The cover glass layer of the PV panel has been employed to achieve an effective and valuable antenna miniaturization. Experimental investigations on antenna prototypes attached to real PV panels have been used to evaluate the effect of cells nearby the slots. Moreover, the presence of a reflector has been considered to get an unidirectional

radiation pattern and increase antenna gain. The proposed slot antennas represent low-cost and compact solutions, which can be integrated into existing PV panels with a relatively easy mechanical process. Future work will be focused on the performance analysis of 2.4 GHz slot antennas integrated in the PV panels of a large solar PV field, mainly to show the effectiveness of the polarization and radiation patterns of the proposed slot antennas in such propagation scenarios.

5 Design and Performance of an Integrated Antenna for a 433MHz Car Park Monitoring System

5.1 Introduction

The demand for intelligent parking systems is expected to grow in the near future, to provide automatic management and monitoring, as well as convenience to the customers [103]-[104]. Such a system can be made of an RF reader, and a set of wireless sensors (or autonomous transmitters) each one placed on the ground of a parking space, as shown in Figure 5.1a. The 433MHz ISM band is preferred to the 2.4GHz one as lower frequency is more robust to car shadowing and interference level is lower too. In [103], an experimental validation of path loss models at 433MHz has been carried out.

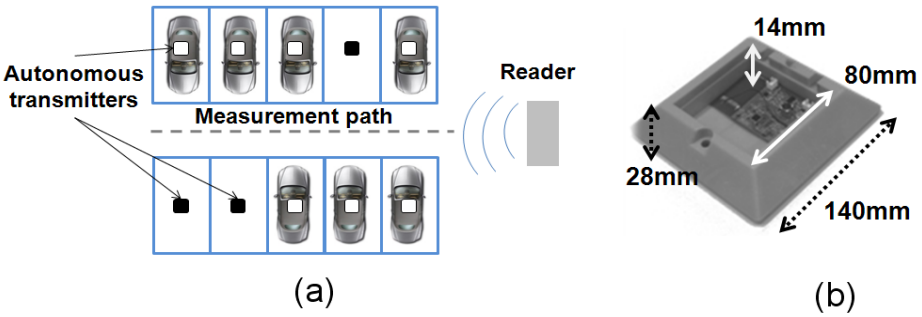

Figure 5.1 - Schematic operating principle of a car park monitoring system (a) and the wireless sensor (b)

The autonomous device developed at CUBIT (Consortium Ubiquitous Technologies), Pisa, Italy, is enclosed in a 140×140×28 mm3 polycarbonate box (Figure

5.1b), and a waterproof ultrasonic transducer is used to check the presence of a car parked above it. Thus, this information is transmitted to the reader through a 433MHz RF transmitter. The device is fed by two 66×50 mm2 photovoltaic (PV) cells and a battery, and covered by a 10-mm-thick acrylic sheet (Plexiglas^{TM}). All above components must fit in a small volume of 80×80×14 mm3. Since the available space is much smaller than the free-space wavelength ($\lambda \approx 700$mm), an electrically small antenna is required. By also considering the restricted available PV power and the complexity of the RF propagation scenario, it results that the efficiency, the polarization and the radiation patterns of the antenna all can represent valuable parameters to improve system performance. Moreover, input impedance matching must be achieved by considering most of the elements included in the sensor enclosure, and not just optimizing the antenna in free-space. Indeed, the presence of the PV cells and the Plexiglas^{TM} cover can introduce a significant antenna detuning. In this chapter the design and performance analysis of an integrated low-cost printed antenna are presented, when most of the above issues are accounted for. A comparison in terms of received power level between the proposed monopole antenna and a commercial 433MHz ceramic antenna is also considered.

5.2 Antenna design and performance

To optimize system performance, a vertically polarized integrated antenna with a null in the direction perpendicular to the ground is recommended. Moreover, a radiation pattern as much as possible uniform in the horizontal plane is required, although this pattern can be strongly distorted by the presence of the elements inside the sensor enclosure (PV cells, battery, ultrasonic transducer, etc.).

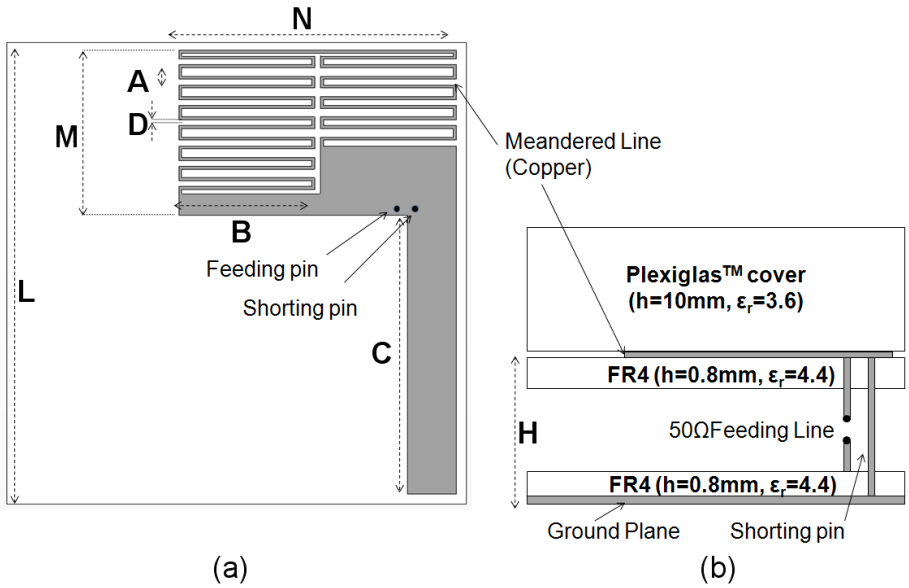

Figure 5.2 - Top view (a) and lateral view (b) of the proposed monopole antenna. Geometrical parameters of the final design: A=2.5mm, B=23mm, C=48mm, D=0.5mm, H=14mm, L=80mm, M=30mm, N=50mm.

To match above requirements, a folded monopole [105] top-loaded with a meandered microstrip line has been realized with a 0.8-mm-thick FR4 substrate, as shown in Figure 5.2. This low-cost structure was designed exploiting at the best the space available inside the sensor box. Numerical simulations were performed using the

commercial software CST MWS®. The resonant frequency was tuned by varying the number of meanders and their separation, as well as other geometrical parameters shown in Figure 5.2a. A number of prototypes have been realized and characterized. Figure 5.3 shows the measured reflection coefficient for one of the first prototypes, when some of the sensor components are separately added; it is clearly apparent the significant effect of the PV cells and the Plexiglas™ cover layer. The autonomous device components lead to an overall frequency shift of about 40MHz, with respect to the case in which only the polycarbonate box is present. As expected, the Plexiglas™ cover layer helps in the antenna miniaturization.

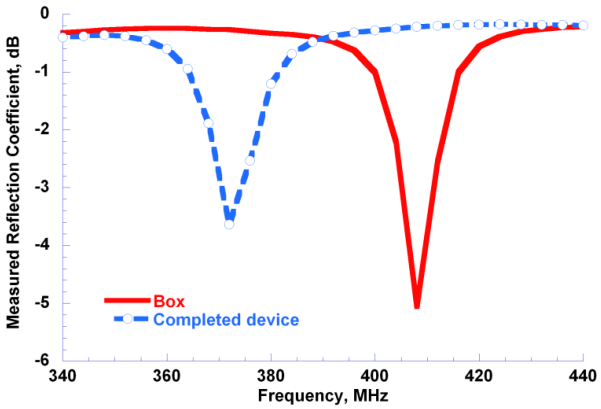

Figure 5.3 - Measured antenna reflection coefficient.

A careful optimization of the antenna parameters (when the monopole is inside the box together with all the nearby sensor components) and the introduction of a simple impedance matching network (composed by a single shunt-connected 6pF capacitor) resulted in a final design with very good performance in terms of input impedance tuning (Figure 5.4).

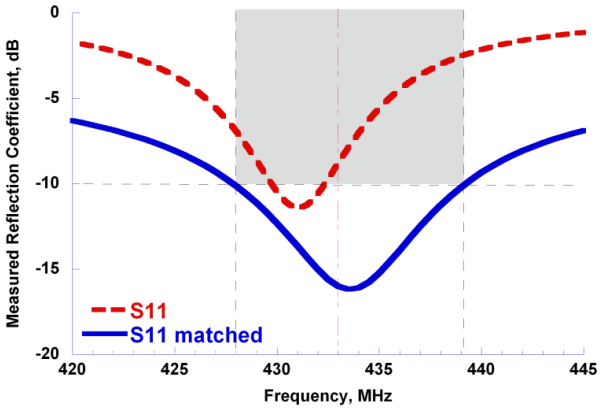

Figure 5.4 - Measured reflection coefficient for the final antenna design, with and without the impedance matching network.

The -10dB bandwidth of the proposed antenna is about 11MHz (about 2.5%), so covering the entire 433MHz ISM band. The final design is characterized by a maximum gain and a radiation efficiency of about -4.2dB and 18%, respectively. A comparison between the monopole antenna and a commercial ceramic antenna ($16\times3\times2$ mm^3) in terms of received power level at the reader was carried out (Figure 5.5). The wireless sensor was moved far from the reader along a linear path (see Figure 5.1a), in a full parking lot. Measurements were performed with a transmission power of 10dBm, using a GFSK modulation. The reader antenna was a $\lambda/4$ monopole characterized by a 2dBi maximum gain. An average increase of the received power level of around 2.2dB was noted when the ceramic antenna is changed with the low-cost printed monopole antenna.

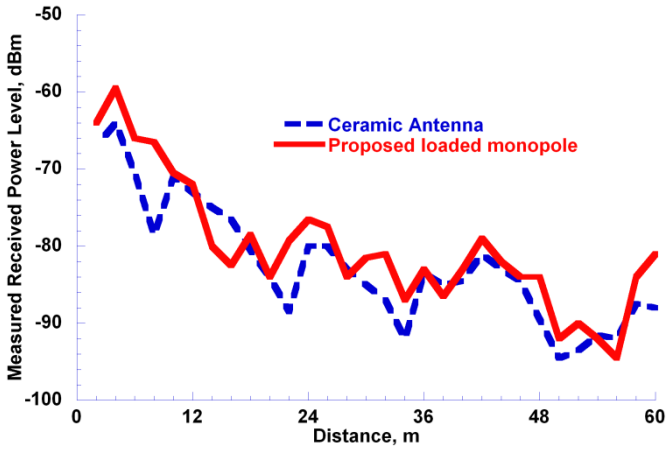

Figure 5.5 - Received power level at the reader when the wireless sensor is moved along the linear path shown in Figure 5.1a and uses either a commercial ceramic antenna or the proposed top-loaded monopole antenna.

5.3 Conclusions

A low-cost printed monopole antenna for the wireless sensors of a 433MHz car park monitoring system has been presented. The improvement of the received power level at the reader, with respect to a commercial ceramic antenna, is mainly due to a careful antenna tuning that accounted for the presence of all the elements nearby the antenna, as well as an effective utilization of the space available inside the sensor enclosure.

CONCLUSIONS

In Chapter I, a novel slot-coupling feeding technique for dual-polarized patch antennas has been presented. A square patch is fed through a square ring slot excited by two non-overlapping feed lines printed on the same side of a single-layer substrate. With respect to other slot-coupling feeding techniques for dual-polarized patch antennas, the configuration here proposed exhibits a simple structure and a valuable symmetry property with respect to the two feeding ports, while preserving a satisfactory isolation. To show the working principle and the radiation properties of the proposed slot-coupled patch, a sample antenna operating in the 3.3-3.8 GHz WIMAX™ frequency band has been designed, prototyped and characterized.

Then the novel slot-coupling feeding technique was used to realize a dual-polarized 2x1 microstrip stacked patch array for mobile wireless communication systems. The array is intended as a basic module for base station linear arrays, whose final size depending on beamwidth and gain requirements. Each array element is fed through two microstrip lines arranged on the basis of a sequential rotation technique. Each stacked square patch is excited through a square ring slot realized in the feeding network ground plane. Design procedure, simulation results and measurement data are presented for a 2x1 array working in the GSM 1800-1900 band (1710 – 1910 MHz), UMTS band (1920 - 2170 MHz), ISM band (2400 - 2484 MHz) and UMTS 3G expansion band (2500 - 2690 MHz) or, alternatively, WIMAX™ band (2300 – 2700 MHz), with a resulting 45% percentage bandwidth (reflection coefficient < -10dB). Due to both the symmetry properties of the novel slot-coupling feeding configuration and the implementation of a sequential rotation technique, good results have been obtained in terms of port isolation and cross-polar radiation patterns.

Finally, the novel slot-coupling feeding technique was used to realize a circularly polarized 2x2 microstrip array. Each array element is fed through two microstrip lines which are excited 90° out-of-phase (dual-feed technique) and coupled to a square patch by means of a square ring slot realized in the feeding network ground plane. Design

procedure, simulation results and measurement data are presented for a 2x2 array working in the WIMAX™ 3.3-3.8 GHz frequency band (14% percentage bandwidth). Due to both the symmetry properties of the novel slot-coupling feeding configuration and the implementation of a sequential rotation technique, excellent Axial Ratio (AR) performance is achieved in the WIMAX™ band (AR<1.35dB at broadside direction) and for any direction in the antenna main beam (AR<2.25dB at 3.55GHz). Actually, the 3dB AR bandwidth is larger than the WIMAX™ frequency band, as it goes up to about 30%.

In Chapter II, a compact dual-band Planar Inverted-F Antenna (PIFA) working in both the DVB-T (Digital Video Broadcasting-Terrestrial) and the WLAN (Wireless Local Area Network) IEEE 802.11b,g frequency bands has been presented. It is designed to be integrated in a monitor-equipped device, exhibiting reduced electrical size with respect to similar PIFA configurations. A reflection coefficient less than -6dB and -10dB was obtained in the 470-862 MHz (59% percentage bandwidth) DVB-T and the 2400–2484 MHz (2.7% percentage bandwidth) WLAN bands, respectively. An antenna gain of almost 3dBi and 4.5dBi, with more than 95% radiation efficiency, was obtained in the two frequency bands of interest. The PIFA fills an overall volume of 217 x 12 x 8 mm^3 and can be realized by properly cut and fold a single metal sheet. Measurements on prototypes have shown that the proposed layout is robust in terms of the impedance matching detuning that can be caused by the presence of metal parts nearby the antenna.

Finally, a dual-band L-shape Planar Inverted-F Antenna (PIFA) suitable to be integrated in a display-equipped device has been presented. The antenna can operate in both the DVB-T (Digital Video Broadcasting Terrestrial) and the WLAN (Wireless Local Area Network) IEEE 802.11b,g frequency bands. A reflection coefficient less than -6dB and -10dB, and an antenna gain of around 2dBi and 6.3dBi, have been obtained in the 470-862MHz DVB-T band (59% percentage bandwidth) and the 2400–2484MHz WLAN band (2.7% percentage bandwidth), respectively. The L- shape PIFA can be obtained by properly cutting and folding a single metal sheet, so resulting in a relatively low-cost and mechanically robust antenna configuration.

In Chapter III, a numerical analysis was performed for a wideband two-arm Archimedean spiral antenna whose arms are made of vertical metallic strips. As such, the proposed antenna structure permits much tighter turns. An advantage of this spiral is that the input impedance and polarization purity can be effectively controlled by varying the strip width and turn thickness. Also, when the antenna is embedded in a dielectric block, miniaturization is more effective than in conventional planar Archimedean spirals.

In Chapter IV, two configurations of slot antennas suitable for integration into a class of commercial large photovoltaic (PV) panels were presented. The basic idea is to exploit the room available between adjacent PV cells, also taking advantage of the presence of the cover glass layer that gives a valuable miniaturization effect. As test cases, two antenna designs are presented for stand-alone communication systems operating in the GSM/UMTS (1710-2170 MHz) and WIMAX (3300-3800 MHz) frequency bands. The numerical design has been performed by resorting to quite simple numerical models; after that, the effects on the antenna performance of the presence of nearby photovoltaic cells, DC bus wires and panel frame have been verified through a measurement campaign with slot antenna prototypes attached to real PV panels. Then, a straightforward fine tuning has been adopted to match the antennas when installed on the panel.

In Chapter V, a top-loaded vertical monopole antenna was designed to be integrated in a wireless sensor of a car park monitoring system operating at 433MHz. The final design came out from a careful analysis of the effects on the antenna input impedance of nearby elements (photovoltaic cells, battery, sensor cover, ultrasonic transducer). A performance comparison between the proposed vertically polarized antenna and a commercial ceramic antenna was presented, showing an average increase of the received power level at the reader of about 2.2dB, when measurements are performed on a distance range of 10-60m between the sensor and the reader antenna of the car park monitoring system.

REFERENCES

[1] R. Caso, A. Serra, A. Buffi, M. R. Pino, P. Nepa, and G. Manara, "A Dual-Polarized Slot-Coupled Patch Antenna Excited by a Square Ring Slot," *IET Microwaves, Antennas, Propag*., vol. 5, pp. 605-610, 2011.

[2] R. Caso, A.A. Serra, P. Nepa, G. Manara, and M.R. Pino, "A square ring slot feeding technique for dual-polarized patch antennas," *IEEE AP-S International Symposium*, Charleston, SC USA, 2009.

[3] A Buffi, R. Caso, G. Manara, P. Nepa, and A.A. Serra, "Ring-slot coupled microstrip patch antennas," *Atti della fondazione Giorgio Ronchi*, 2010.

[4] R. Caso, A. Buffi, and A.A. Serra, "*Ring slot coupled microstrip patch antennas*," *RiNEm Riunione Nazionale di Elettromagnetismo*, Benevento, Italy, 2010.

[5] A. Buffi, R. Caso, M.R. Pino, P. Nepa, and G. Manara, "Single-Feed Circularly Polarized Aperture-Coupled Square Ring Slot Microstrip Antenna," *IET Electronics Letters*, 46, (4), pp. 268-269, 2010.

[6] R. Caso, A. Buffi, M.R. Pino, P. Nepa, and G. Manara, "A novel dual-feed slot-coupling feeding technique for circularly polarized patch arrays," *IEEE Antennas and Wireless Propagation Letters*, 9, pp. 183-186, 2010

[7] A. Buffi, R. Caso, M.R. Pino, P. Nepa, and G. Manara, "A novel slot-coupling feeding technique for circularly polarized patch antennas," *IWAT International Workshop on Antenna Technology*, Lisbon, Portugal, p. 1-4, 2010

[8] R. Caso, A. Buffi, M.R. Pino, P. Nepa, G. Manara, "An annular-slot coupling feeding technique for dual-feed circularly polarized patch arrays," *IEEE AP-S International Symposium,* Toronto, Ontario, 2010.

[9] A. Buffi, R. Caso, M.R. Pino, P. Nepa, and G. Manara, "Circularly Polarized Square Ring Slot Patch Antennas," *IEEE AP-S International Symposium*, Toronto, Ontario, 2010.

[10] A. Buffi, R. Caso, M.R. Pino, P. Nepa, "AR Bandwidth Enhancement for Single-Feed Circularly Polarized Square Ring Slot Patch Antenna," *EMTS International Symposium on Electromagnetic Theory,* Berlin, Germany, 2010.

[11] R. Caso, A.A. Serra, M.R. Pino, P. Nepa, and G. Manara, "A Wideband Slot-Coupled Stacked-Patch Array for Wireless Communications," *IEEE Antenna and Wireless Propagation Letters*, vol.9, pp. 986-989, 2010.

[12] R. Caso, A.A. Serra, M.R. Pino, P. Nepa, and G. Manara, "A wideband linear array of slot coupled stacked-patches," *IEEE AP-S International Symposium*, Toronto, Ontario, 2010.

[13] A. Buffi, R. Caso, G. Manara, P. Nepa, and A.A. Serra, "Dual-polarization slot-coupled patch antennas: state-of-art and a novel configuration," *Giornata di studio sulla caratterizzazione di antenne*, Salerno, Italy, 2009.

[14] R. Caso, G. Manara, P. Nepa, and A.A. Serra, "Progettazione di antenne per apparati WIMAX," *RiNEm Riunione Nazionale di Elettromagnetismo*, Lecce, Italy, 2009.

[15] A.A. Serra, R. Caso, P. Nepa, and G. Manara, "A wideband dual-polarized stacked patch antenna array for base stations," *ISAP - International Symposium on Antennas and Propagation*, Taipei, Taiwan, 2008.

[16] R. Caso, G. Manara, P. Nepa, and A.A. Serra, "Antenne a microstriscia a larga banda e multi-banda per le stazioni radio base dei sistemi UMTS, WLAN e WIMAX," *Giornata di Studio: Coesistenza e compatibilità elettromagnetica delle tecnologie wireless emergenti*, L'Aquila, Italy, 2008.

[17] http://www.telsasrl.it/

[18] R. Caso, A. D'Alessandro, A.A. Serra, P. Nepa, and G. Manara, "An Integrated Dual-Band PIFA for DVB-T and WIMAX Applications," *IEEE Antenna and Wireless Propagation Letters*, pp. 1027-1030, 2011.

[19] R. Caso, A. D'Alessandro, A.A Serra, P. Nepa, and G. Manara, "Wideband integrated H-PIFA antenna for DVB-T and WIMAX applications," *IEEE AP-S International Symposium*, Spokane, Washington, USA, 2011.

[20] R. Caso, A. D'Alessandro, A.A. Serra, P. Nepa, and G. Manara, "A Compact Dual-Band PIFA for DVB-T and WLAN Applications," to appear on *IEEE Transaction on antennas and Propagation,* 2012.

[21] R. Caso, A. D'Alessandro, A.A. Serra, P. Nepa, and G. Manara, "Dual-band integrated G-PIFA antenna for DVB-T and WLAN applications," *IEEE AP-S International Symposium on Antennas and Propagation*, Spokane, Washington, USA, 2011.

[22] R. Caso, A. D'Alessandro, A.A. Serra, and P. Nepa, "Dual-Band L-Shape PIFA for Display-Equipped Devices," submitted to Electronic Letters, 2012.

[23] http://www.seco.com/

[24] A Guraliuc, R. Caso, P. Nepa, and J. L. Volakis, "Numerical Analysis of a Wideband Thick Archimedian Spiral Antenna," to appear on *IEEE Antennas and Wireless Propagation Letters*, 2012.

[25] A. Michel, R. Caso, P. Nepa, L. Tavanti, L. Gazzarrini, and R. Garroppo, "Design and Performance Analysis of a Slot Antenna Integrated in a Photovoltaic Panel," *IEEE AP-S International Symposium*, Chicago, Illinois, USA, 2012.

[26] R. Caso, A. D'Alessandro, A. Michel, P. Nepa, and G. Manara, "Integration of Slot Antennas in Commercial Photovoltaic Panels for Stand-Alone Communication Systems," submitted to *IEEE Transactions on Antennas and Propagation, 2012.*

[27] http://www.cubitlab.com/

[28] R. Caso, A. Michel, P. Nepa, G. Manara, and R. Massini, *"Design and Performance of an Integrated Antenna for a 433MHz Car Park Monitoring System*," *IEEE AP-S International Symposium*, Chicago, Illinois, USA, 2012.

[29] D.M Pozar, "Microstrip antenna aperture-coupled to a microstrip-line," *Electronics Letters*, 21, (4), pp. 49-50, 1985.

[30] A.A. Serra, P. Nepa, G. Manara, G. Tribellini, and S. Cioci, "Wideband dual-polarized stacked patch antenna array for base stations," *Microwave and Optical Technology Letters*, 52, (5), pp. 1048-1052, 2010.

[31] C.H Tsao, Y.M. Hwang, F. Kilburg, and F. Dietrich, "Aperture-coupled patch antennas with wide-bandwidth and dual-polarization capabilities," *Proc. IEEE Antennas and Propagation Symposium*, pp. 936-939, 1988.

[32] M. Barba, "A High-Isolation, Wideband and Dual-Linear Polarization Patch Antenna," *IEEE Trans. Antennas and Propagation*, 56, (5), pp. 1472-1476, 2008.

[33] A.A. Serra, P. Nepa, G. Manara, G. Tribellini, and S. Cioci, "A wideband dual-polarized stacked patch antenna," *IEEE Antenna and Wireless Propagation Letters*, 6, pp. 141-143, 2007.

[34] M. Yamazaki, E.T. Rehardjo, and M. Haneishi, "Construction of a slot-coupled planar antenna for dual-polarization," *Electronics Letters*, 30, (22), pp. 1814-1815, 1994.

[35] J.R. Sanford, and A. Tengs, "A two-substrate dual polarised aperture coupled patch," *Proc. IEEE Antennas and Propagation Symposium*, pp. 1544-1547, 1996.

[36] M. Edimo, A. Sharaiha, and C. Terret, "Optimised feeding of dual polarised broadband aperture-coupled printed antenna," *Electronics Letters*, 28, (19), pp. 1785-1787, 1992.

[37] B. Lindmark, "A novel dual polarized aperture coupled patch element with a single layer feed network and high isolation," *Proc. IEEE Antennas and Propagation Symposium*, pp. 2190-2193, 1997.

[38] V. Boyanov, "A novel dual polarized aperture coupled patch element with a single layer feed network and high isolation," *Proc. IEEE International Symposium on Phased Array Systems and Technology*, pp. 318-322, 2003.

[39] A. Adrian, and D.H. Schaubert, "Dual aperture-coupled microstrip antenna for dual or circular polarization," *Electronics Letters*, 23, (23), pp. 1226-1228, 1987.

[40] F. Rostan, and W. Wiesbeck, "Design considerations for dual polarized aperture-coupled microstrip patch antennas," *Proc. IEEE Antennas and Propagation Symposium*, pp. 2086-2089, 1995.

[41] K.L. Wong, H.C. Tung, and T.W. Chiou, "Broadband dual-polarized aperture-coupled patch antennas with modified H-shaped coupling slots," *IEEE Trans. Antennas and Propagation*, 50, (2), pp. 188-191, 2002.

[42] L.L. Shafai, W.A. Chamma, M. Barakat, P.C. Strickland, and G. Seguin, "Dual-band dual-polarized perforated microstrip antennas for SAR applications," *IEEE Trans. Antenna and Propagation*, 48, (1), pp. 58-66, 2000.

[43] B. Lee, S. Kwon, and J. Choi, "Polarisation diversity microstrip base station antenna at 2GHz using T-shaped aperture-coupled feeds," *IEE Proceedings on Microwaves, Antennas and Propagation*, 148, (5), pp. 334-338, 2001.

[44] S.C. Gao, L.W. Li, M.S. Leong, and T.S Ye, "Dual-polarized slot-coupled planar antenna with wide bandwidth," *IEEE Trans. Antenna and Propagation*, 51, (3), pp. 441-448, 2003.

[45] S.C Gao, L.W. Li, P. Gardner, and P.S. Hall, "Wideband dual-polarised microstrip patch antenna," *Electronics Letters*, 37, (20), pp. 1213-1214, 2001.

[46] P. Brachat, and J.M. Baracco, "Printed radiating element with two highly decoupled input ports," *Electronics Letters*, 31, (4), pp. 245-246, 1995.

[47] R.G. Vaughan, "Polarization diversity in mobile communications," *IEEE Trans. Veh. Tech.*, vol. 39, no. 3, pp. 177-86, 1990.

[48] M. Kar, and P. Wahid, "Two-branch space and polarization diversity schemes for dipoles," *Proc Int Symp IEEE Antennas Propag*., vol.3, pp. 364-367, 2001.

[49] P.S. Hall, J.S. Dahele, and J.R. James, "Design principles of sequentially fed, wide bandwidth, circularly polarised microstrip antennas," *IEE Proceedings part H, Microwaves, Antennas and Propagation*, vol. 136(5), pp. 381-389, 1989.

[50] F. Rostan, and W. Wiesbeck, "Design considerations for aperture-coupled microstrip patch phased arrays taking into account mutual coupling effects," *X International Conference on Antennas and Propagation*, vol. 1, pp. 237-240, 1997.

[51] F. Rostan, and W. Wiesbeck, "Aperture-coupled microstrip patch phased arrays in C- and X-band: a contribution to future multi-polarization multi-frequency SAR systems," *IEEE International Symposium on Phased Array Systems and technology*, pp. 141-146, 1996.

[52] P. Sharma, and K. Gupta, "Analysis and Optimized Design of Single Feed Circularly Polarized Microstrip Antennas," *IEEE Transactions on Antennas and Propagation*, vol. 31, pp. 949-955, 1983.

[53] S.D. Targonski, and D.M. Pozar, "Design of wideband circularly polarized aperture-coupled microstrip antennas," IEEE Transactions on Antennas and Propagation, vol. 41, n. 2, 1993.

[54] J. Huang, "A Technique for an Array to Generate Circular Polarization with Linearly Polarized Elements," *IEEE Transactions on Antennas and Propagation*, vol. 34, pp. 1113-1124, 1986.

[55] A.K. Singhal, R. Jyoti, and S.B. Sharma, "Sequentially rotated broadband circularly polarized patch array antenna," *International Conference on Recent Advances in Microwave Theory and Applications*, 2008.

[56] G. Leon, M.R. Pino, and F. Las Heras, "Improvement of a broadband circularly polarized planar array," *EUCAP 2007*, 2007.

[57] S. Hienonen, A. Lehto and A. V. Raisanen, "Simple broadband dual-polarized aperture-coupled microstrip antenna," *Proc. IEEE Antennas and Propagation Symposium*, pp. 1228-1230, 1999.

[58] DVB Project, [Online]. Available: http://www.dvb.org/

[59] K.L. Wong, C.I. Lin, T.Y. Wu, and J.W. Lai, "A planar DTV receiving antenna for laptop applications," *Microw. Opt. Technol. Lett.*, vol. 42, no. 6, pp. 483–486, 2004.

[60] C.M. Su, L.C. Chou, C.I. Lin, and K.L. Wong, "Internal DTV receiving antenna for laptop application," *Microw. Opt. Technol. Lett.*, vol. 44, no. 1, pp. 4–6, 2005.

[61] Y.W. Chi, K.L. Wong, "Wideband printed dipole antenna for DTV signal reception," in *Proc. TENCON IEEE Region 10 Conference* , pp.1-4, 2007.

[62] W.S. Chen, Y.T. Chen, H.T. Chen, and J.S. Kuo, "A Wideband Printed Monopole Antenna for Wireless Applications," in *Proc. IEEE AP-S Int. Symp., Charleston, SC, 2009.*

[63] C. Yang, J. Kim, H. Kim, J. Wee, B. Kim, and C. Jung, "Quad-Band Antenna With High Isolation MIMO and Broadband SCS for Broadcasting and Telecommunication Services," *IEEE Antennas Wireless Propag. Lett.* , vol. 9, pp. 584-587, 2010

[64] C. Y. Huang, B. M. Jeng, and J. S. Kuo, "Grating Monopole Antenna for DVB-T Applications," *IEEE Trans. Antennas Propag.*, vol. 56, no. 6, pp. 1775-1776, 2008.

[65] C. Y. Huang, B.M. Jeng, and C.F. Yang, "Wideband monopole antenna for DVB-T applications," *Electron. Lett.* , vol. 44, no. 25, pp. 1448-1450, 2008.

[66] C.H. See, R.A. Abd-Alhameed, D. Zhou, and P.S. Excell, "A Planar Inverted-F-L Antenna (PIFLA) With a Rectangular Feeding Plate for Lower-Band UWB Applications," *IEEE Antennas Wireless Propag. Lett.,* vol. 9, pp. 149-151, 2010.

[67] L. Low, J. Batchelor, R. Heaton, and N. Chen, "Dual patches microstrip fed antenna with wide bandwidth," in *Proc. LAPC Antennas and Propagation Conference*, pp.429-432, 2009.

[68] J.K. Wee, J.W. Park, I.S. Yeom, B.G. Kim, and C.W. Jung, "Compact DVB-H Antenna With Broad Dual-Band Operation for PMP Applications," *IEEE Antennas Wireless Propag. Lett.*, vol.9, pp.580-583, 2010.

[69] P. Nepa, G, Manara, A.A. Serra, and G. Nenna, "Multiband PIFA for WLAN mobile terminals,"*IEEE Antennas and Wireless Propagation Letters*, vol.4, pp. 349- 350, 2005.

[70] S. Filipović, and J.L. Volakis, "Broadband meanderline slot spiral antenna", *IEEE Proc. Microw. Antennas and Propag.*, vol. 149, no. 2, pp. 98-105, 2002.

[71] B.A. Kramer, C.C. Chen, and J.L. Volakis, "Size reduction of a low-profile spiral antenna using inductive and dielectric loadings," *IEEE Antennas and Wirel. Propag. Lett.*, vol. 7, pp. 22-25, 2008.

[72] H. Nakano, R. Satake, and J. Yamauchi, "Extremely low-profile, single-arm, wideband spiral antenna radiating a circularly polarized wave," *IEEE Trans. on Antennas and Propag,* 58(5), pp. 1511-1520, 2010.

[73] M.J. Radway, T.P. Cencich, and D.S. Filipović, "Pattern purity of coiled-arm spiral antennas", *IEEE Trans. on Antennas and Propag.*, vol. 59, no. 3, pp. 758-766, 2011.

[74] B.A. Kramer, C.C. Chen, and J.L. Volakis, "Fundamental limits and design guidelines for miniaturizing ultra-wideband antennas," *IEEE Antennas and Propag. Mag.*, vol. 51, no. 4, pp. 57-69, 2009.

[75] B.A. Kramer, M. Lee, C.C. Chen, and J.L. Volakis, "Design and performance of an ultrawide-band ceramic-loaded slot spiral," *IEEE Trans. on Antennas and Propag.*, (53), pp. 2193-2199, 2005.

[76] B.A. Kramer, S. Koulouridis, C.C. Chen, and J.L. Volakis, "A novel reflective surface for an UHF spiral antenna," *IEEE Antennas and Wireless Propag. Lett.*, vol. 5, pp. 32-34, 2006.

[77] J.L. Volakis, G. Mumcu, K. Sertel, C.C. Chen, M. Lee, B. A. Kramer, D. Psychoudakis, and G. Kiziltas, "Antenna miniaturization using magnetic-photonic and degenerate band-edge crystals," *IEEE Antennas and Propag. Mag.*, vol. 48, no. 5, pp. 12-28, 2006.

[78] H. Nakano, "A meander spiral antenna," *Proc. IEEE Antennas Propag. Soc. Int. Symp.*, vol. 3, pp. 2243-2246, 2004.

[79] M. Lee, B. A. Kramer, C.C. Chen, and J.L. Volakis, "Distributed lumped loads and lossy transmission line model for wideband spiral antenna miniaturization and characterization," *IEEE Trans. on Antennas and Propag.,* vol. 55, no. 10, pp. 2671-2678, 2007.

[80] B. Wang, and A. Chen, "Design of an Archimedean spiral antenna", *Int. Symp. Antennas Propag. and EM Theory (ISAPE)*, pp. 348-351, 2008.

[81] K.L. Kaiser, "Electromagnetic compatibility handbook", Chapter 27, pp. 188-190, *CRC Press*, 2005.

[82] S. Koulouridis, G. Kiziltas, Y. Zhou, D. Hansford, and J. L. Volakis, "Polymer–Ceramic Composites for Microwave Applications: Fabrication and Performance Assessment," *IEEE Trans. Microwave Theory and Techniques*, vol. 54, no.12, pp. 4202-4208, 2006.

[83] S.H. Lee, J. Lee, Y.J. Yoon, S. Park, C. Cheon, K. Kim and S. Nam, "A Wideband Spiral Antenna for Ingestible Capsule Endoscope Systems: Experimental Results in a Human Phantom and a Pig," *IEEE Trans. on Biomedical Engineering.,* vol. 58(6), pp. 1734-1741, 2011.

[84] M.J. Roo Ons, S.V. Shynu, M.J. Ammann, S.J. McCormack, and B. Norton, "Transparent patch antenna on a-Si thin-film glass solar module," *Electronics Letters* , vol.47, no.2, pp.85-86, 2011.

[85] T. Yasin, and R. Baktur, "Inkjet printed patch antennas on transparent substrates," *IEEE Antennas and Propagation Society International Symposium*, 2010.

[86] T.W. Turpin, and R. Baktur, "Meshed Patch Antennas Integrated on Solar Cells," *IEEE Antennas and Wireless Propagation Letters*, vol. 8, pp. 693-696, 2009.

[87] N. Henze, A. Giere, H. Friichting, and P. Hofmann, "GPS Patch Antenna with Photovoltaic Solar Cells for Vehicular Applications," *58th IEEE Vehicular Technology Conference Fall 2003*, Orlando, US, 2003.

[88] C. Bendel, J. Kirchhof, and N. Henze, "Application of photovoltaic solar cells in planar antenna structures," *Proceedings of 3rd World Conference on Photovoltaic Energy Conversion*, 2003, Volume 1, pp. 220 – 223, 2003.

[89] N. Henze, M. Weitz, P. Hofmann, C. Bendel, J. Kirchhof, and H. Fruchting, "Investigation of planar antennas with photovoltaic solar cells for mobile communications," *15th IEEE International Symposium on Personal, Indoor and Mobile Radio Communications*, *PIMRC*, Vol. 1, pp. 622 – 626, 2004.

[90] S. Vaccaro, P. Torres, J.R. Mosig, et al., "Integrated solar panel antennas," *Electronics Letters*, 36, (5), pp. 390–391, 2000.

[91] M.J. Roo Ons, S.-V. Shynu, M.J. Ammann, S. McCormack, and B. Norton, "Investigation on Proximity-Coupled Microstrip Integrated PV Antenna," *2nd European Conference on Antennas and Propagation*, EuCAP 2007, 2007.

[92] S.V. Shynu, M.J. Ammann, and B. Norton, "Quarter-wave metal plate solar antenna," *Electronics Letters*, vol. 44(9), pp. 570-571, 2008.

[93] S.-V. Shynu, M.J. Roo Ons, P. McEvoy, M.J. Ammann, S.J. McCormack, and B. Norton, "Integration of Microstrip Patch Antenna With Polycrystalline Silicon Solar Cell," *IEEE transactions on Antennas and Propagation*, vol. 57(12), pp. 3969-3972, 2009.

[94] N. Henze, C. Bendel, and J. Kirchhof, "Photovoltaic power supply and antennas in one device for wireless telecommunication equipment," INTELEC 2005, Berlin, Germany, 2005.

[95] M. Danesh, and J.R. Long, "Compact Solar cell Ultra-Wideband dipole antenna," *IEEE Antennas and Propagation Society International Symposium,* 2010.

[96] T. Wu, R.L. Li, and M.M. Tentzeris, "A mechanically stable, low profile, omni-directional solar cell integrated antenna for outdoor wireless sensor nodes," *IEEE Antennas and Propagation Society International Symposium*, 2009.

[97] S.V. Shynu, M.J. Roo Ons, M.J. Ammann, B. Norton, and S. McCormack, "Dual band a-Si:H solar-slot antenna for 2.4/5.2GHz WLAN applications," *3rd European Conference on Antennas and Propagation*, pp. 408-410, 2009.

[98] K.L Chung and A.S. Mohan, "Effect of superstrate thickness on the performance of broadband circularly polarised stacked patch antenna," *IEEE Antennas and Propagation Society International Symposium*, vol.1, pp. 687- 690, 2004.

[99] W. Kueathawikun, P. Thumwarin, N. Anantrasirichai, and T. Wakabayashi, "Wide-Band Slot Antenna for IEEE 802.11b/g," *SICE-ICASE International Joint Conference*, Bexco, Busan, Korea, 2006.

[100] J.Y. Jan, and J.W. Su, "Bandwidth enhancement of a printed wide-slot antenna with a rotated slot," *IEEE Transactions on Antennas and Propagation*, vol.53, no.6, pp. 2111- 2114, 2005.

[101] http://www.brandonisolare.com/

[102] http://www.risenenergy.com

[103] K. Phaebua, C. Phongcharoenpanich, D. Torrungrueng, and J. Chinrungrueng, "Short-distance and near-ground signal measurements in a car park of wireless sensor network system at 433MHz," *5th International Conference on ECTI-CON*, pp.241-244, 2008.

[104] V.W.S Tang, Y. Zheng, and J. Cao, "An Intelligent Car Park Management System based on Wireless Sensor Networks," *1st International Symposium on Pervasive Computing and Applications*, pp.65-70, 2006.

[105] H.K. Ryu, S. Lim, and J.M. Woo, "Design of electrically small, folded monopole antenna using C-shaped meander for active 433.92 MHz RFID tag in metallic container application," *Electronics Letters*, vol.44, no.25, pp.1445-1447, 2008.